Department of Precision and Microsystems Engineering

Correct examination of vibration energy harvester performance

Joeri Roos

Report no : 2020.056
Coach : T.W.A. Blad
Professor : J.W. Spronck
Specialisation : MSD
Type of report : M.Sc. Thesis
Date : 15 November 2020

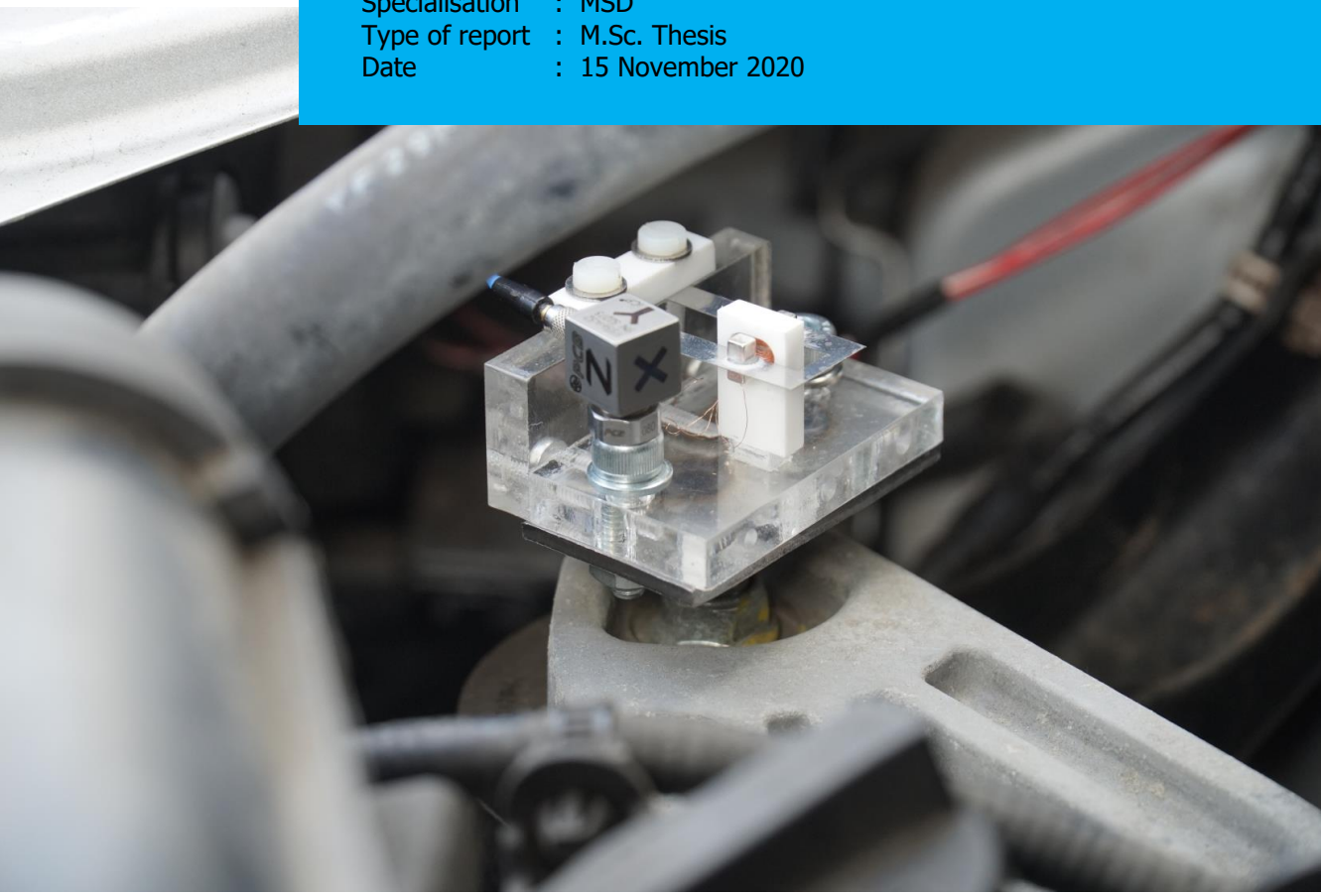

TU Delft Delft University of Technology

Challenge the future

CORRECT EXAMINATION OF VIBRATION ENERGY HARVESTER PERFORMANCE

vision, theory and experimental

M.Sc. Thesis

In partial fulfillment of the requirements for the degree of
Master of Science in Mechanical Engineering.
at the Department of Precision and Microsystems Engineering,
Delft University of Technology, Delft, The Netherlands
to be defended on Thursday, December 3rd, 2020 at 13:30.

by

Joeri Roos

born in Gouda, The Netherlands

Report no.	2020.056
Daily supervisor	Ir. T.W.A. Blad
Senior supervisor	Ir. J.W. Spronck
Specialization	Mechatronic System Design
Type of report	M.Sc. Thesis
Project duration	September 2, 2019 – December 3, 2020

This thesis was approved by the thesis committee:

Ir. J.W. Spronck	MSD, PME, 3ME, TU Delft
Ir. T.W.A. Blad	MSD, PME, 3ME, TU Delft
Dr. G.J. Verbiest	DMN, PME, 3ME, TU Delft

Keywords: Vibration energy harvesting, Real world vibrations, Electrodynamic shaker control, Vibration analysis

Printed by:

An electronic version of this thesis is available at `http://repository.tudelft.nl/`.

TU Delft Delft University of Technology

Preface

I've been building things almost all my life. My parents told me when I was little, some pieces of wood, a hammer and nails were the best toys for me. I also enjoyed playing with Lego technic a lot, always trying to build something else than the box was meant for or try to improve the design. Later on, the Lego was exchanged for all kind of mechanical constructions around the house or on the farm. I'm always fascinated about the different machines we use in our daily life and have a desire to know the mechanics behind all of them.

During the Bachelors final project, I came in touch with energy harvesting. The idea that everywhere around us, kinetic energy can be turned into electrical energy, was just fascinating. Knowing, that the source of energy already is there and just some technical innovations are required to make use of it. That was for me the drive to continue researching in the form of a master thesis.

I'm convinced that, one day, vibration energy harvesting will become a versatile and reliable source for low power electronics. Hopefully, this thesis will bring my vision one step closer to reality.

Please, enjoy reading my thesis!

Joeri Roos
Delft, December 2020

Summary

Vibration energy harvesting can become a durable source of energy for wireless sensors or other low power applications like pacemakers. Huge savings in ecological footprint, production and maintenance costs can be achieved by replacing batteries for vibration energy harvesters. Most of the time, newly developed energy harvesters are tested in a lab environment on an electrodynamic shaker. The problem is that the standard lab experiments in the form of a sinusoidal or Gaussian noise signal excitation are not representative for the real world applications. In a classification of ambient vibrations it was observed that most vibrations found in the real world consist of a series of dominant frequencies, shocks and noise. It was also seen that among real world vibrations, there is a lot of variation in the power distribution among the classes. In the aim to bring the vibration energy harvester performance tests closer to the real world applications, an experimental benchmarking of energy harvester performance has been conducted. An energy harvester is designed and applied in the real world on the engine of two different cars. Successively, three different lab experiments are performed on an electrodynamic shaker, each experiment with its own type of vibration control. It is found that only taking the FFT data of a real world vibration is not sufficient. Using a sinusoidal excitation matching a single amplitude and frequency, or even a noise excitation matching the entire power spectrum, results in an under or overestimation of 50% compared to the real world performance. Therefore, to accurately predict the performance of an energy harvester in the real world, simulation or experimental testing need to be performed on the actual or a replication of the intended real world vibration.

Contents

1 Vibration Energy Harvesting **1**
- 1.1 Introduction to energy harvesting . . . 2
- 1.2 How is vibration energy harvester performance tested? . . . 4
- 1.3 Problem statement . . . 4
- 1.4 Thesis outline . . . 5

2 On the classification of ambient vibrations for vibration energy harvesting **7**
- 2.1 Introduction . . . 8
- 2.2 Method . . . 9
- 2.3 Power distribution classification . . . 10
- 2.4 Results . . . 14
- 2.5 Discussion . . . 16
- 2.6 conclusion . . . 17

3 Benchmarking of energy harvesting performance on real world vibrations **19**
- 3.1 Introduction . . . 20
- 3.2 Method . . . 21
- 3.3 Results . . . 26
- 3.4 Discussion . . . 28
- 3.5 Conclusion . . . 30

4 Reflection, conclusions and recommendations **31**
- 4.1 Overview of research activities . . . 32
- 4.2 Successes . . . 33
- 4.3 Unsuccessful attempts . . . 34
- 4.4 Conclusions . . . 36
- 4.5 Recommendations . . . 36

A Vibration energy harvester test setup **41**
A.1 Components block scheme 42
A.2 Lab equipment 42

B Electrodynamic vibration shaker dynamics **47**
B.1 Schematic mass-spring-damper shaker model 48
B.2 Dynamical transfer function identification 53

C Electrodynamic shaker controller **61**
C.1 Frequency sweep controller; RMS based feedback 62
C.2 Power spectrum controller; FFT based feedback 72
C.3 Time Waveform Replication; Feedforward control 81

D Car vibration experiments **87**
D.1 Real world vibration measurement setup 88
D.2 Car engines as source of vibration 89
D.3 Measured acceleration data; raw 90
D.4 Measured acceleration data; analysis 92

E Harvester design **95**
E.1 Cantilever beam resonance harvester 96
E.2 Magnetic spring resonance harvester 104

1 Vibration Energy Harvesting

This chapter introduces the art of motion energy harvesting by explaining the basic principles and possible field applications. The main focus will lay on harvesting energy from vibrations. One of the problems which we need to overcome in order to make vibration energy harvesters commonly used in practice is given in the problem statement. This results in a research objective and research question. Finally, the thesis outline is given.

1.1 Introduction to energy harvesting

Energy harvesting is the process by which energy is derived from external sources (e.g., solar power, thermal energy, wind energy, salinity gradients, and kinetic energy, also known as ambient energy.)
Wikipedia

Turning ambient energy into electricity is a quite common feature in our society. Significant steps in the direction of renewable energy already have been taken in the form of solar, wind and hydro power. However, these solutions are predominately on the large scale and non-portable. Therefore, relies the majority of portable device upon batteries as a source of energy. However, batteries only contain a finite amount of energy, which brings up two major downsides up:

- **Ecological impact:** Batteries consist most out of chemical components. More than half of the used batteries is not recycled in the Netherlands [48]. They end up in the thrash or environment where they form a toxic pollution.
- **Economical impact:** Replacement of batteries in electronic devices is not always a simple swap-and-go procedure. For instance your own smartphone, a large number of smartphones need to be disassembled by removing the screen and other hardware in order to reach the battery. It can also be the case that the entire battery powered device is hard to reach; like the sensors on a vehicle or the pacemaker in your heart.

New solutions in the field of energy harvesting will have the opportunity to replace batteries, which will solve these problems. The ambient sources of energy are virtually unlimited.

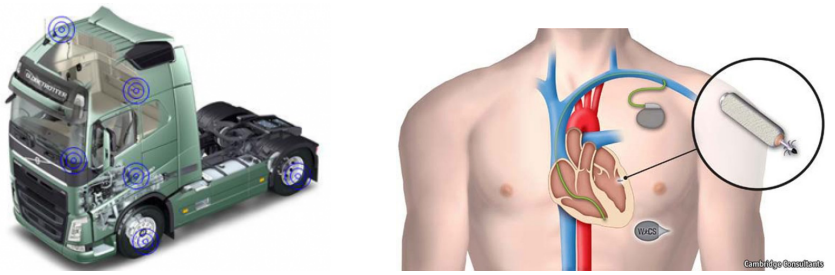

(A) (B)

FIGURE 1.1: **Examples of vibration sources and energy harvesting applications; A) Automotive sensors on a truck , B) human heart to power pacemakers [12, 40]**

1.1.1 Vibration energy harvesting

As the name says, vibration energy harvesting is the name for a process that extracts energy from an ambient vibration and converts it into electrical energy. Vibration energy can come from different origins, for example big applications like civil structures, trains, airplanes or even your own car, or from smaller applications such as your own heart or wrist.
In order to harvest electrical energy from vibrations, a vibration energy harvester (VEH) is needed. The VEH can in essence fulfill two functions simultaneously: it damps out the possible undesired vibrations and generates useful power. The conversion form kinetic to electrical energy is performed with a transducer mechanism. In the field of energy harvesting three different transducers are commonly used; Piezoelectric, Electromagnetic and Electrostatic.
Each transducer needs a mechanical mechanism to operate, which most of the times consists out of a proof mass that moves with respect to the harvester's housing figure 1.2. The mass m connected to the harvester's housing by a spring k. Due to external motion $y(t)$, moves the proofmass with respect to the harvesters housing $z(t)$. This movement dives the transducer where some of the kinetic energy is converted into electrical. The extraction of kinetic energy out of the system will damp out the motion of the proofmass, this is displayed as a damper c.

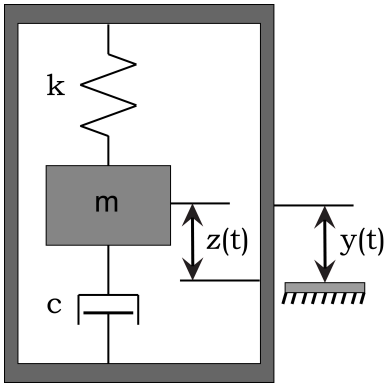

FIGURE 1.2: **Schematic model of a spring suspended vibration energy harvester. The mass *m* moves with respect to the harvester housing *z(t)* due to external vibrations *y(t)*. The transducer extracts kinetic energy from the system and damps out the motion as a damper *c*.**

Most ongoing research focuses on the design and improvement of the mechanical mechanism, transducer or signal conditioning. When a vibration energy harvester is designed, the performance is mostly tested in a lab environment with an electrodynamic shaker.

1.2 How is vibration energy harvester performance tested?

One of the most common tests for vibration energy harvester performance is the sinusoidal frequency sweep. In this test, the vibration energy harvester is placed on an electrodynamic shaker. This is a heavy and more robust kind of loudspeaker, where on top a test specimen, like the vibration energy harvester, can be mounted. The shaker performs a sinusoidal oscillation with an increasing or decreasing frequency. The frequency sweep is well suited for system identification, because all the instantaneous power is concentrated in one frequency. This way can the system response per frequency input easily be derived.
Commonly, the acceleration during the sweep is kept at a constant value, which is done by changing the amplitude of oscillation during the sweep with $\frac{1}{\omega^2}$. During the frequency sweep the output power of the harvester is monitored. This results in an overview of the power output per frequency for a specific acceleration.

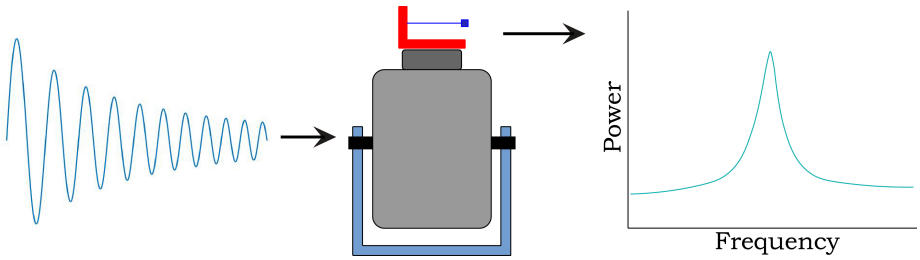

FIGURE 1.3: **Depiction of the standard procedure during a frequency sweep. A sweep signal is generated and fed to the shaker. The shaker, with the harvester attached on top, executes the vibration signal and the harvester power output is monitored. In the end, a graph showing the power generation per frequency is obtained.**

1.3 Problem statement

The applications for energy harvesters are already there, for instance your own car. Sensors are located all over the car. To power these sensors, wires have to be pulled through the chassis. Replacing the wired for wireless sensors could result in significant savings in production costs and weight. Also the quality and reliability of the sensors could increase by taking out the possible wire and connector errors [40]. To make energy harvesting devices feasible for the car application, the step from lab environment experiments to the real world needs to be taken. This can be approached from two sides; on one side more knowledge should be obtained about the vibration characteristics found in a car. While on the other side, the lab experiments should be able to represent the car vibrations in order to validate the harvester design. Therefore, the goal of this research is:

Indicate the correct experimental validation for vibration energy harvester performance in the real world.

To reach the goal, it is necessary to answer fist some sub-questions. These will be addressed according to the following structure:

- What are the characteristics found in real world vibrations?
- How is the performance of a vibration energy harvester tested nowadays?
- How can real world vibration characteristics be represented in a lab environment?

1.4 Thesis outline

This thesis focuses on bridging the gab between lab and real-world vibration energy harvester performance. Several topics are addressed: Vibration analysis, harvester dynamics and performing field and lab tests.

The second chapter contains the research paper on the classification of ambient vibrations for motion energy harvesting. In this chapter, dominant frequency, shock and noise content in various real world vibrations are analyzed. The amount of power in each class is separated in order to obtain an overview of the main source of energy in various real world vibrations. This demonstrated the differences among the real world vibrations, increasing the need for different harvester designs. Further details like, frequency range, amplitude of acceleration and shock -rate and -time, have been denoted to indicate different real world vibration characteristics in order to improve harvester design.

In the third chapter an experimental research paper is presented. The paper focuses on the comparison between real world and shaker excited energy harvester performance. Three different experiments have been designed to examine the energy harvester's output; a constant acceleration frequency sweep, a power spectrum matching random signal and a time waveform replication controller. A cantilever beam electromagnetic energy harvester design is used for the experiments. The energy harvester performance measured in a real world experiment on a car engine is compared with the various lab experiments. This demonstrated the essence of performing the correct experiment to make an accurate prediction on the real world performance.

The fourth chapter contains an overview of the research activities during the graduation project. Also, a critical reflection of the author about the successes and unsuccessful attempts is made. Followed by the conclusions drawn over the entire project and some recommendations for future research.

To preserve the thesis' main line on the research, but still keep a good track on the steps made during the project, the following appendices were added. Appendix A gives an overview of the test setup and equipment used to perform the lab experiments. In Appendix B the dynamics of an electrodynamic shaker have been derived based on a double mass- spring- damper model and an experimental transfer function identification. To control the shaker's output, three different controllers were designed and implemented on the cRIO. Each controller has it's own specific purpose, which is elaborated in appendix C. Appendix D presents more details on the real world vibrations measured on a car engine. An overview of the raw acceleration data followed by the analyzed data is set out. During the process, two different harvester prototypes were build. The design procedures of both prototypes can be found in appendix E.

2

On the classification of ambient vibrations for vibration energy harvesting

In this chapter, the research paper as part of the literature review is presented. Dominant frequency, shock and noise content is analyzed in various real world vibrations. Based on the amount of content in each class a power distribution has been made, these results have been presented in a triangular plot distribution. Details coming from the vibration analysis can be used to improve harvester design for real-world applications.

2

On the classification of ambient vibrations for Vibration energy harvesting

J.Roos, T.W.A.Blad and J.W. Spronck

Abstract— **This research presents an analysis to characterize real world vibrations based on their power distribution. High energy regions in time and frequency are identified with the use of a spectrogram. This enables a classification based on shock, dominant frequency and noise power in the vibration source. From the analyzed signals can be seen that there is a lot of variation in the power distribution among real world vibrations. Using the results, applications to motion energy harvesters and further important details found in environmental vibrations characterization are discussed.**

Keywords— **Ambient Vibrations, Vibration Analysis, Power Classification, Vibration Energy Harvesting**

2.1 Introduction

Energy is everywhere around us in various forms. These environmental sources of energy gain more and more interest, because of their potentials, with vibrational energy in particular [7]. In order to harvest the kinetic energy effectively, harvester mechanics have to match the environmental vibration characteristics [22]. Frequency matching is one of the most common, where the eigenfrequency of the mechanism matches the frequency of excitation. A mismatch can result in a significant output power decrease for resonating systems [17].
Previous works have already studied energy harvesting from non-harmonic inputs. Various harvesters have been tested on the human gait [11, 18, 41, 50]. Lan and Quin [29] have performed a study using Gaussian White noise with different intensities, where Cottone et al. [13] used colored noise in order to match better with real-world vibrations [14]. Since the studied environmental vibrations are all different in appearance and characteristics, some vital information about the vibration source omits in these studies. Kok et al. [25] have analyzed vibration sources on dominant frequencies and acceleration amplitude. In the study of Rantz and Roundy [37] a classification based on source and spectrogram appearance was made, where the number of dominant frequencies was counted and signals were labeled with an acceleration amplitude or noise tag. Beeby et al. [8] performed long time acceleration measurements on various vehicles, and looked into the peak frequency and amplitude range.

However, none of these studies have indicated how the signal power is distributed over the vibration. The goal of this study is to characterize real-world vibrations based on power distribution in both time and frequency domain. To this end, a method to analyze vibration signals and indicate high-power regions is introduced.

Section II gives the scope used for the literature search and important input characteristics for motion energy harvesters are stated. Section III gives the classification to distinguish vibration sources and describes the developed analysis. Section IV, Results, presents the power distribution and source characteristics found in real-world vibrations. Section V starts with an interpretation of the results, followed by energy harvesting applications and analysis limitations. Finally, in section VI the conclusions are stated.

2.2 Method

2.2.1 Search domain

In order to make a classification on real-world vibrations, information about the actuation of different energy harvesters is used. To this end, mainly books and review papers describing the different harvester types were used.

In order to perform the analysis, acceleration data of real world vibrations was searched for. The focus is on translational vibration data coming from all kinds of sources, for example, human motion, transportation, civil structures or industrial machines.

2.2.2 Harvester input characteristics

The most common way to model the mechanism of a motion energy harvester is a mass-spring-damper system [24], where relative displacement between the mass and generator housing drives a transducer to generate electrical energy. This system can be used as a *resonant device*, where the eigenfrequency is determined by the mass and stiffness. The other possibility is a *non-resonant device*, which has for example no restoring force for the mass [36].

In the case of a resonant device, the source of the vibration should be described on the basis of the most common or dominant frequency and its acceleration [36]. A non-resonant device has an eigenfrequency in a totally different frequency range as the excitation or does not contain an eigenfrequency; these systems can be designed to harvest impact or impulse forces. The source vibration should be described by the impulse, $\int F(t)dt$, and its rate of occurrence [36].

2.3 Power distribution classification

For real-world vibrations, the power distribution can vary in time and frequency domain. To make the potentials for energy harvesting come forward, a power based classification, which is able to allocate high power regimes, was made.

1. **Dominant Frequency**
   The dominant frequency class focuses on the power distribution in frequency domain, continuous over time. A frequency is classified as dominant when there is a significantly higher amplitude compared to the total frequency range. Only peaks larger than 50% of the largest peak are denoted as dominant frequency, see figure 2.1. For each dominant frequency, the mode (most common frequency), range and average acceleration are denoted, this was done for the more detailed analysis, which is needed for motion energy harvester design.

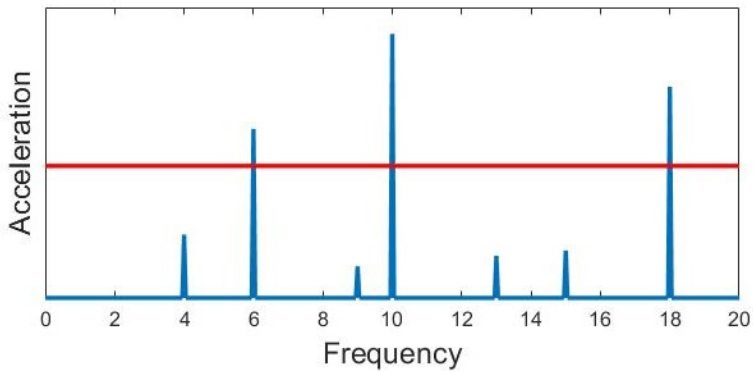

FIGURE 2.1: **FFT plot showing various dominant frequency peaks of an arbitrary signal. The $10\,Hz$ peak has the largest amplitude. Only peaks larger than half the largest peak amplitude, indicated by the red horizontal line, are denoted as dominant frequency.**

2. **Shock**
   The shock class quantifies the power variations in time. When the vibration power increases above twice the average, a shock is identified, see figure 2.2. To quantify a shock, the rate of occurrence over the whole time range and the average duration of a shock are denoted for the more detailed analysis.

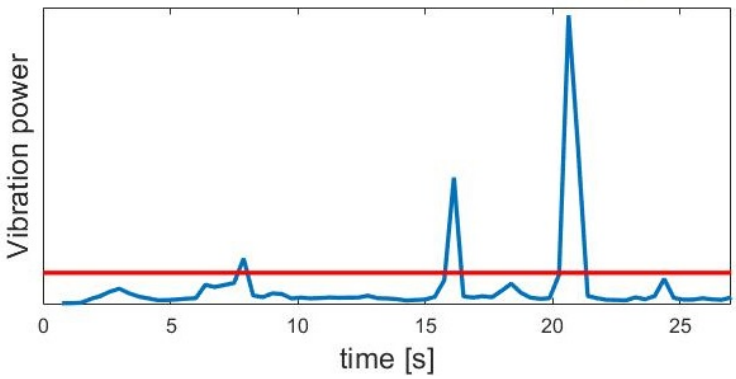

FIGURE 2.2: **When the vibration power increases above twice the average, indicated by the red horizontal line, a shock is identified.**

3. **Noise**
   Noise classifies the vibrations where no large variations are found in time or frequency. The signal power has an equal or random distribution in frequency and a constant power over average time.

2.3.1 Vibration analysis

For the analysis of environmental vibrations, the real vibration database [35] and the EH Network data Repository [34] are used to obtain raw acceleration data of real-world vibrations. The database files contain tri-axial acceleration data in time domain, where the acceleration data was represented in 'g' ($1\,g = 9.81\,m/s^2$). The text below describes the steps made to analyze the real-world vibrations, where the first step in the vibration analysis is source characterization. The origin of the measured signal can already tell a lot about the expected accelerations and behavior. Three real-world vibration signals, coming from the NiPS laboratory "Real Vibration" database [35], are used as visualization:

1. Top-loading washing machine, continuous centrifugation without clothes in the basket. Accelerometer located at the top of the loading door.

2. Adult human walking upstairs with the accelerometer attached to the left ankle.

3. Renault Clio 1.9 TD driving in urban conditions with the accelerometer placed at the wheel suspension.

In order to perform the analysis, the signal is divided into time blocks. On every time block a Fast Fourier Transform (FFT) is applied to obtain the acceleration amplitude per frequency in the given block. This FFT data is plotted for all the time blocks to obtain a spectrogram in which the acceleration per frequency and time block can be seen during the whole signal measurement, figures 2.3, 2.4 & 2.5. In order to obtain a clear spectrogram, the edge response has to be narrow [44], trade-offs between time and frequency resolution have to be made [45]. A Hanning-window with 2/3 or 3/4 block overlap works best to avoid discontinuities at the beginning and end of a block [26]. Overlapping the time blocks also compensates for data loss at the beginning and end of the block due to windowing.

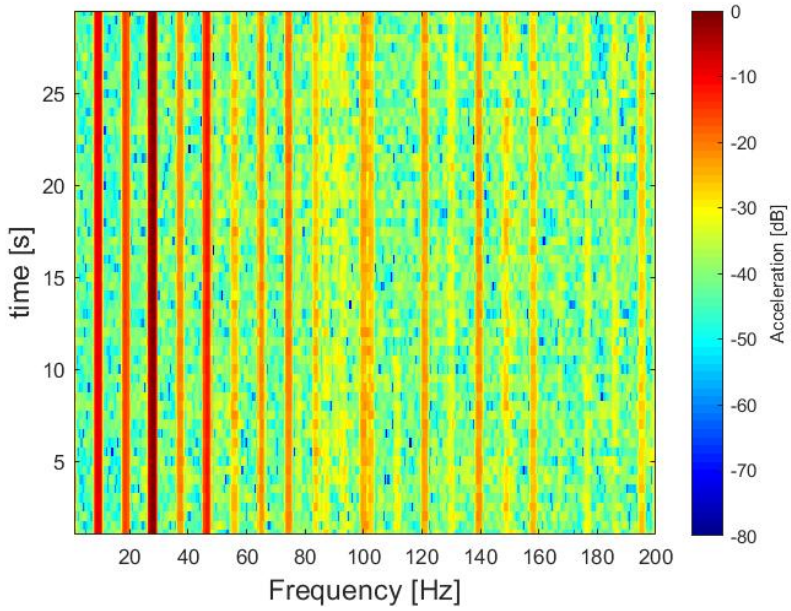

FIGURE 2.3: **Spectrogram made of the top-loading washing machine vibration signal. The vertical lines indicate frequency appearance constant over time, where only the line around $28\,Hz$ is indicated as dominant, because the other vertical lines had an average amplitude smaller than half the largest amplitude**

The amplitude of acceleration is shown by color indication in the spectrogram. To find dominant frequencies, a search on every FFT time block is performed to find the frequency with largest acceleration over a certain range. This gives an overview how the dominant frequencies vary over time. In order to identify how much the dominant frequencies vary over time the 90-Percentile frequency interval is taken to quantify a dominant frequency bandwidth for the real-world vibrations.

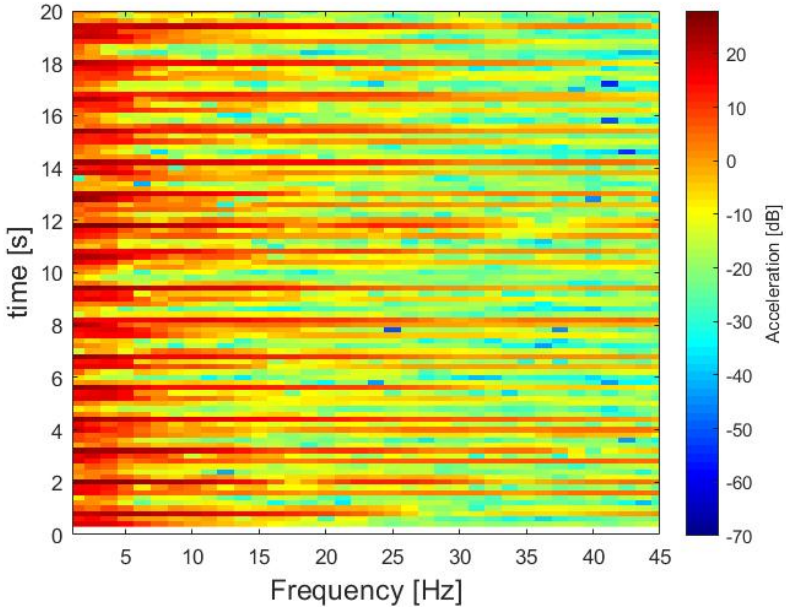

FIGURE 2.4: **Spectrogram made of the human walking upstairs, showing mainly horizontal lines which can be caused by foot-step strike. The horizontal red lines are an indication of shocks in the vibration.**

Shocks are found by taking the squared sum of all frequency content from a single FFT block. The squared sum indicates the power of each FFT block [27] and gives a time-power relation. When the power is larger than twice the average, it is denoted as a shock. For every signal, the shock rate and average duration of a shock are recorded.

Now the dominant frequency and shock areas in the spectrogram are known, the power of each can be determined. The signal power in a specified time and frequency window can be calculated using equation (2.1), [28], with P_m is the mean power, T the time interval, $H(f)$ the applied window to indicate the bandwidth and $L_T(f)$ the Fourier transform of the time signal.

$$P_m = \lim_{T\to\infty} \frac{2}{T} \int_0^\infty |H(f)|^2 |L_T(f)|^2 df \tag{2.1}$$

In the example, figure 2.5, the dominant frequency power can be found in the vertical black boxes and the shock power in the horizontal black boxes.

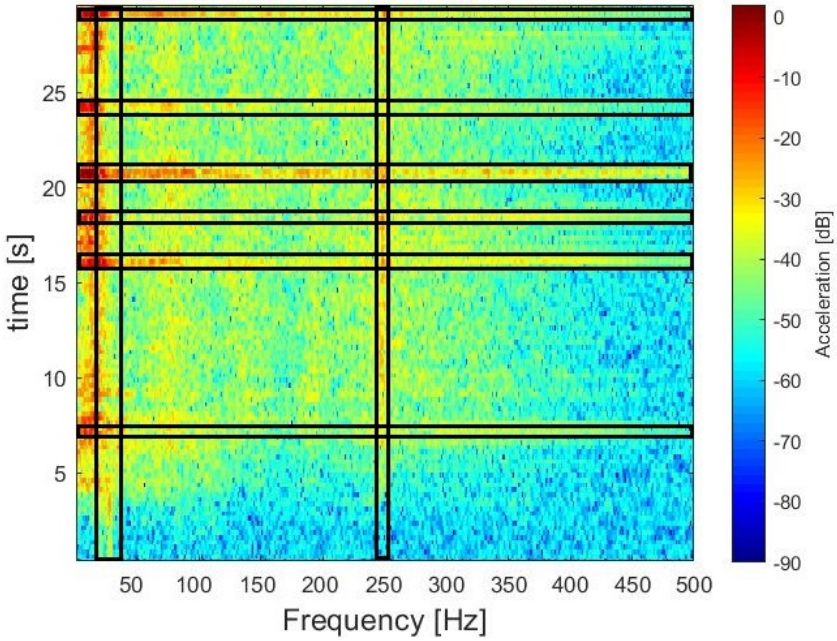

FIGURE 2.5: **Spectrogram made of the Renault Clio driving in urban conditions. Analysis gives dominant frequencies at** 35 **and** 246 Hz**, with a 90-percentile bandwidth of** $25-45\,Hz$ **and** $245-251\,Hz$ **respectively. The areas identified as dominant frequency or shock are marked with vertical and horizontal black boxes respectively.**

2.4 Results

The power distribution in the analysis was divided into three classes. It was desired to visualize this in a single two dimensional plot to obtain a clear overview. The horizontal position is determined by the mutual relation between shock and dominant frequency power. In order to determine the vertical position, the amount of energy located in the shocks and dominant frequencies is divided by the total vibrational energy.

In the top of the figure, where the noise power dominates the signal, the amount of power in shocks or dominant frequencies is negligible, which makes the small difference between them less significant. In order to visualize this, it was chosen to narrow the top of the figure down to a single point and this created a triangular figure with in each corner the ideal situation of a class. Signals located on the edge of the triangle contain all their power in the two classes connected by the edge and no power in the other class.

TABLE 2.1: **More detailed analysis of vibration sources, required for harvester design**

Vibration source	Car driving	Washing machine	Human walking
RMS acceleration [mg]	467	189	483
Dominant frequency [Hz]	35, 249	28	-
Range [Hz]	[25;45] [245;251]	[28;29]	-
Largest RMS acc. [mg]	36.6	101	-
Shock rate [n/s]	0.17	-	0.73
Shock time [s]	0.53 ± 0.19	-	0.32 ± 0.11

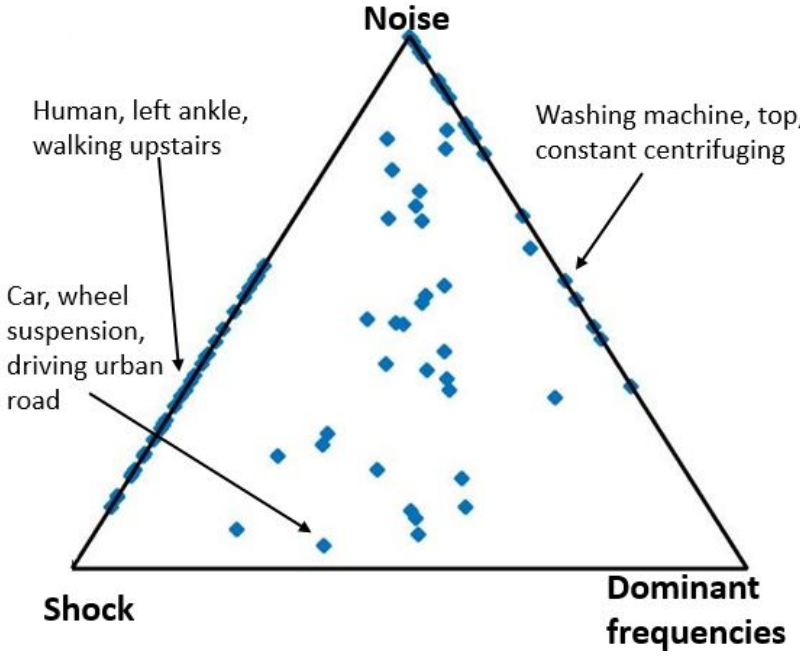

FIGURE 2.6: **Power distribution of various environmental vibrations.**

Figure 2.6 shows the power distribution of different environmental vibrations. After classifying the vibration source based on power, more details are needed for harvester design [36]. Table 2.1 shows a short preview of the more detailed results coming from the example vibrations shown in the spectrogram figures 2.3, 2.4 & 2.5. These vibration sources are also indicated in figure 2.6, to indicate their power distribution.

2.5 Discussion

The first notable characteristic in the power classification is the overall distribution: many of the environmental vibrations contain a significant amount of noise and only little dominant frequency power, which reached at most 74% of the total signal power. Vibrations with dominant frequencies often contain a lot of (smaller) higher order resonances, with still some of vibration power, for example in the case of a washing machine. Because these smaller resonances were not denoted as dominant frequencies, they have been allocated to noise.

Shock power was able to cover a larger part of the total signal power (max. 86%). This is because some signals had a very low overall RMS acceleration, with some moments of shock with significantly higher accelerations. The other possibility was that the shocks had a high rate of occurrence, which was in the case of a human walking.

Quite some signals are located on the line between shock and noise, meaning they do not contain any dominant frequency power. The studies performed by Kok et al. and Beeby et al. [8, 25] did not take such signals into account. Reilly et al. and Rantz et al. [38, 39] noted that some signals were characterized by shocks, but did not mention any further details. For signals with both shocks and dominant frequencies a choice has to be made, which can be aided by the more detailed analysis. For example, an effective resonator can be designed when the dominant frequency bandwidth is narrow [8].

2.5.1 Energy harvesting applications

Motion energy harvester performance is frequently validated by the use of a frequency sweep [51], which is a good strategy to find the peak performance. However, the signal power of a sinusoid would, in the power triangle, be placed in the dominant frequency corner, where none of the environmental vibrations are located. Studies of Fan et al. and Sallaudin et al. [17, 42] show almost four times lower output power for the intended application than found in the performed frequency sweep, which was done in order to find the maximum output power of the harvester. In order to come closer to a real-world performance estimation, the frequency sweep should be performed for the frequency range and accelerations found in the real world-vibration.

Figure 2.6 is able to show in one glance how the vibrational power is distributed in a source. With the power distribution known, a more detailed overview of the source characteristics has to be made for harvester design. When the source shows significant dominant frequency content, the dominant frequencies with their range and accelerations should be denoted. When the source shows large variations in acceleration, the rate of occurrence and shock-time should be denoted.

2.5.2 Analysis limitations

One disadvantage of the analysis is spectrogram tuning. There is no optimal setting which can visualize the key elements for every signal. So, still some human input is required. The FFT settings have effect on the frequency range for dominant frequencies and shock-time, which slightly affects the power distribution found.

For very low frequency signals, FFT settings can change the outcome completely. Take for example human foot accelerations while walking 2.4. When the windowsize is set to around one second, the spectrogram will mainly show shocks coming the foot-floor impact. When the windowsize is increased significantly, to the order of ten seconds, the spectrogram will show a dominant frequency around $1\,Hz$. In this study, it is chosen to classify signals like these as shock, because most reported resonating harvesters are based on cantilever designs [24], which become very long or thin to reach low stiffness for a low resonant frequency.

2.5.3 Future research

Successively on this vibration classification study, a practical validation of shock, dominant frequency and noise characteristics found in signals should be performed. The time response of a dominant frequency found in the signal can have a totally different shape than a standard sine wave. For the low frequencies ($< 5\,Hz$) the border between repetitive shocks and low frequency vibrations becomes less obvious.
This vibration analysis indicates sometimes real-world vibrations with multiple dominant frequencies, the phase relation between the frequency content is lost. Multiple frequencies can either amplify or attenuate each other. Therefore a more detailed analysis on real-world vibrations should be used and the effect of phase changes on resonating motion energy harvesters should be studied.

2.6 conclusion

A lot of studies into the design of motion energy harvesters are performed, only a few take the vibration source potentials into account. Therefore, this research has presented an analysis to characterize real-world vibrations based on their power distribution. High energy areas in time and frequency are identified with the use of a spectrogram. This has enabled a classification based on shock, dominant frequency and noise power in the vibration source. From the analyzed signals, it can be seen that there is a lot of variation in the power distribution among real-world vibrations; the signal power was never contained in purely dominant frequencies or shocks. The intended application should therefore be taken into account during the design and experimental validation of a motion energy harvester.

2

3

Benchmarking of energy harvesting performance on real world vibrations

This chapter presents an experimental research paper on energy harvester performance in various lab tests compared with the real world performance. The energy harvester performance measured on a running car engine, is compared with lab experiments using an electrodynamic shaker.

3

Benchmarking of energy harvester performance on real world vibrations

Theory and experimental validation

J. Roos, T.W.A. Blad and J.W. Spronck

Abstract— **This paper presents a comparison on resonance energy harvester power output in the real world versus three benchmark experiments. An one degree of freedom electromagnetic energy harvester is built and tested in various lab experiments using an electrodynamic shaker; sinusoidal frequency sweep, power spectrum matching noise and real world waveform replication. Comparing the vibration energy harvester power output, the frequency sweep showed a 50% underestimation, the power spectrum matching noise experiment made a 50% overestimation and the field wave replication remained within the 7% error. Results indicate the essence of vibration energy harvester performance testing on real world-like vibrations, to obtain an accurate performance indication.**

Keywords— **Vibration energy harvesting, real world, lab, electrodynamic shaker control, vehicle vibrations**

3.1 Introduction

Wireless system are becoming ubiquitous; for example, implementing wireless sensor systems in a vehicle could save on production costs and weight, and also increase the performance by taking out possible wire and connector errors [40]. Traditionally, wireless systems are mostly battery powered systems, which limits the intended lifetime due to recharging and aging of the battery. Therefore, replacing batteries with small and long lasting power sources, like energy harvesters, could bring a solution to increase the lifetime [16]. Vibrations coming from dynamical systems like industrial machines, portable devices or transportation vehicles, would form one of the most promising sources to harvest energy from [8].

In the past, large efforts have been made on designing new vibration energy harvesting (VEH) mechanisms. Beside studies focused on mechanism design, transducer materials or signal conditioning, the study of Beeby et al. [8] indicated the essence of simulation and experimental testing, in order to design and select the most suitable energy harvester for particular applications. Beeby's work indicated that for each application, the VEH parameters need to be optimized to maximize the harvested power. Although, these VEHs are designed for particular

real world applications, experimental validation is still mostly performed in lab environments.

VEH lab experiments are mostly performed on a vibration exciter in the form of an electrodynamic shaker. One of the most common experiments to test VEHs is the frequency sweep, where the shaker excites a sinusoidal wave at an in- or decreasing frequency [5, 18, 31, 42]. The research of Rantz and Roundy [38] indicated that real world vibrations consist of a series of stationary frequencies with some distortions. As a result, the frequency sweep often gives an under or overestimation of real world performance [37]. Therefore, VEHs have also been tested on white noise signals, to approach the multiple frequencies present in real world signals. [19, 31, 32].

However, some frequency content is more significant than the other in reald world vibrations. Colored noise experiments have aslo been conducted, as the frequency content in real world signals is non-uniform [13, 29]. Here, a part of the frequency band amplitude is amplified, in order to get closer to real world signals containing dominant frequency content. However, these experiments are still not representative for the real world performance.

Therefore, the goal of this research is, to benchmark the various lab experiments and indicate a better method for predicting energy harvester performances under real word conditions. To this end, the performance of linear resonant VEH in three lab environment tests is compared to a real world experiment on a running car's engine suspension.

Section II, presents the VEH design method, followed by the experimental setup and the three different controller typologies used to perform the lab experiments. Section III sets the experimental results out, which are further discussed in section IV. Finally, a summary of the main findings, togherther with the most important conclusions is provided in section V.

3.2 Method

3.2.1 Energy harvester design

Mechanical design

The VEH is designed as a one degree of freedom resonator. This can be modeled as the classical single mass-spring-damper system, as shown in Figure 3.1a. The equation of motion of such systems can be described with the following formula:

$$m\ddot{z} + c\dot{z} + kz = -m\ddot{y} \tag{3.1}$$

where, z is the excitation of the moving mass with respect to the base and y is the base excitation. The designed VEH has a moving mass of $m = 0.98g$, bending stiffness of $k = 61N/m$ and a mechanical damping coefficient of $c_{mech} = 0.0012N/ms^{-1}$. The mechanical damping has been determined with the logarithmic decrement method at open circuit conditions. When the harvester is connected to the load resistance the damping coefficient increased to $c = 0.0024N/ms^{-1}$ as a result of the damping due to the electromagnetic coupling. More details on the on the VEH parameters and system identification experiments can be found in Appendix E

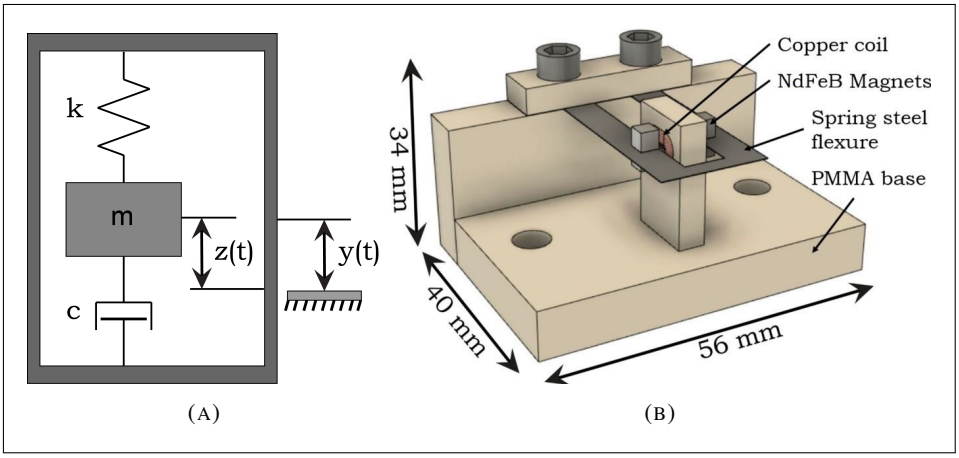

FIGURE 3.1: **Single mass-spring-damper system used to derive the VEH's equations of motion (A) and a 3D model of the linear resonance harvester (B), consisting of a base (Creme), spring steel flexure (dark gray), cubic magnets (light gray) and a copper coil (copper).**

The VEH consists of a static racetrack coil with on both sides permanent magnets attached on to a flexible beam. The magnetic flux lines go from one magnet, through the coil, to the other magnet, Figure 3.1b. This electromagnetic configuration is adopted from the works of Torah et al. [47] and Glynne-Jones et al. [21]. The electromagnetically generated voltage, V_{em}, can be calculated from the obtained velocity, $\dot{z}$, according to equation (3.2). The electromagnetic conversion constant, $\Phi = 0.09$, has been determined in the model verification experiment.

$$V = -\Phi\dot{z} \tag{3.2}$$

Fabrication

This one degree of freedom linear resonance harvester consists of a static coil with 460 turns of $71\mu m$ copper wire. This resulted in a 32Ω resistance and an inductance of $670\mu H$. The power output during the experiments was measured over a 30 Ω load resistance. The 0.10 mm thick spring steel flexure has two $5.5mm$ wide cantilever beams surrounding the coil and connected to each other on the tip. The four, $3mm$ cubic NdFeB magnets, with a magnetic flux density of $1.2T$, are glued on the cantilever beams at $20mm$ from the base. Each magnet weights $0.21gram$, together with the distributed beam mass can this be assumed as a discrete system with a $0.98gram$ mass located at $20mm$ from the base of the cantilever beam.

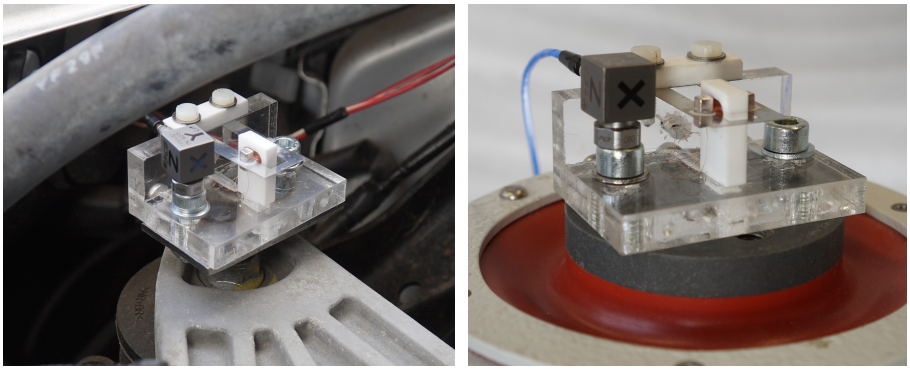

(A) (B)

FIGURE 3.2: **The harvester mounted at the engine side of the suspension with the accelerometer attached to it (A) and the energy harvester and accelerometer attached on the vibration shaker (B).**

3.2.2 Experimental setups

Real world experiments

The real world experiments have been carried out by mounting the VEH on the engine suspension of two cars, Figure 3.2a. The first real world experiment was on the engine of a Suzuki Swift with a 1.2L petrol engine. During the experiment, the engine ran constantly at 1320 RPM. Because of the property of a four cylinder engine of combusting twice per rotation, the dominant frequency could be found at 44Hz. An FFT is performed to identify this dominant frequency; a corresponding acceleration of 0.37g ($1g = 9.61m/s^2$) was found. The second real world experiment was performed on a Volvo V50 with a 2.0L diesel engine.

During the experiment the engine was kept at a constant level of 1140 RPM. This resulted in a 38 Hz dominant frequency with an acceleration amplitude of 0.54g found. The acceleration data on the VEH and the generated voltage over a 30 Ω resistance are measured simultaneously with a 5120Hz sample rate using the NI-cDAQ-9171 and NI-9234 module. A complete overview of the real world experiments data with the setup used for the field measurements, can be found in Appendix D

Lab experiments setup

A schematic presentation of the various components used in the lab setup is depicted in Figure 3.3. The lab experiments have been carried out on the TV51110 electrodynamic vibration exciter (shaker). The NI cRIO-9040 acts as a controller, actuator and data sampler. The actuation signal is sent by the NI-9260 C series voltage output module to the amplifier and successively to the shaker, where the electrical signal is transformed into motion. The VEH is fastened on top of the shaker as in figure 3.2b. Acceleration data is obtained/provided a PCB accelerometer mounted on the VEH frame. The acceleration data is sampled by the NI-9234 C series sound and vibration input module. Simultaneously, the generated voltage of the VEH, is sampled by the NI-9215 C series voltage input module.

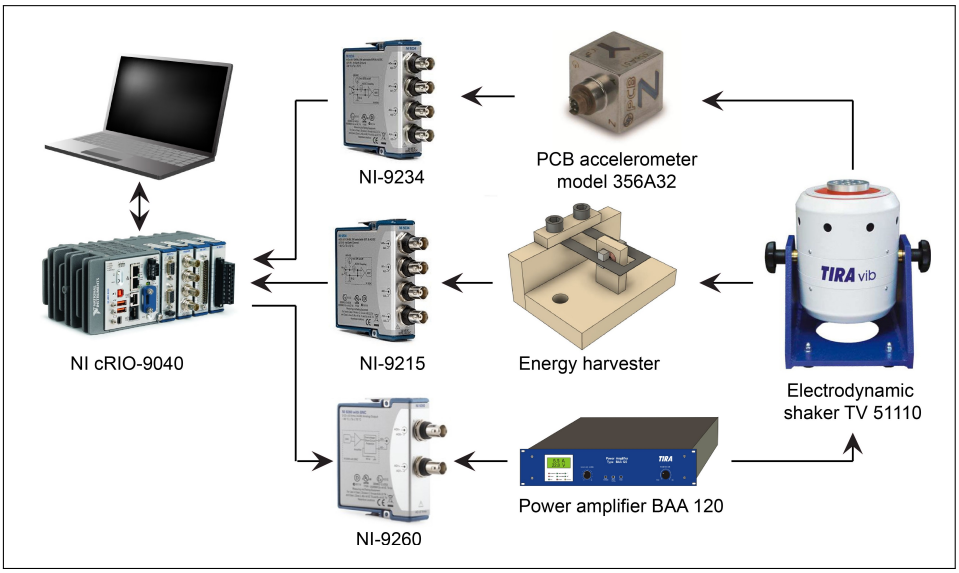

FIGURE 3.3: **Schematic depiction of the setup used during the lab experiments.**

Frequency sweep experiment

The frequency sweep controller produces a sinusoidal excitation signal. The frequency of the sinusoidal signal in or decreases over time at a predefined rate. A feedback control structure is designed in order to keep the acceleration amplitude constant. The acceleration profile is assumed to be a sinusoidal waveform. Therefore, the acceleration amplitude can be determined by taking the RMS acceleration and multiplying this by $\sqrt{2}$. Due to the presence of noise, this gives a more representative value for the acceleration amplitude than the maximum acceleration. The acceleration amplitude is compared to a reference value and successively, the actuation signal amplitude is adapted according to equation (3.3), where A_{i+1} is the new actuation signal amplitude, A_i is the previous actuation signal amplitude, r is the measured acceleration amplitude over the reference ($\frac{\text{acceleration amplitude}}{\text{reference acceleration}}$) and K is the compress factor, which sets the proportional gain of the controller.

$$A_{i+1} = \begin{cases} A_i \times \frac{K+1/r}{K+r} & \text{if } r \leq 1 \\ A_i \times \frac{K+1}{K+r} & \text{if } r > 1 \end{cases} \tag{3.3}$$

Power spectrum experiment

The power spectrum controller generates a Gaussian distributed noise signal, of which the power spectrum (R) is matched to that of the field measurement (R). A feedback control structure is designed, to generate a random signal with the same power spectrum as the represented real world signal. The FFT is constantly taken over a one second time interval, which results in a frequency spectrum with a one hertz resolution. The obtained power spectrum R of the acceleration profile is compared to the reference power spectrum R. Successively, the new actuation power spectrum D_{i+1} is generated from the old actuation power spectrum D_i according to equation (3.4). Here the discount factor k is used to alter the controller's gain. Eventually, by an inverse FFT, the actuation power spectrum is converted into a time signal to actuate the shaker.

$$D_{i+1} = D_i \left(\frac{A}{R}\right)^k \tag{3.4}$$

Wave replication experiment

The wave replication controller makes a replication of the acceleration data loaded into the controller. With the use of a feedforward control, the desired acceleration waveform is generated by the shaker. In order to design the feedforward controller, a system identification of the electrodynamic shaker was performed. A description of mechanical and electrical model of the electrodynamic shaker and a step by step derivation of the transfer function with the experimental identification, can be found in Appendix B. Successively, the feedforward controller was designed as described in the paper of Della Flora and Gründling [15]. Appendix C gives more details on the design, implementation and usage of the three different controllers.

3.3 Results

3.3.1 Model verification

In Figure 3.4 the simulated velocity response and experimental voltage output are shown. It can be observed that the velocity is related to the generated voltage by a constant factor of 0.09.

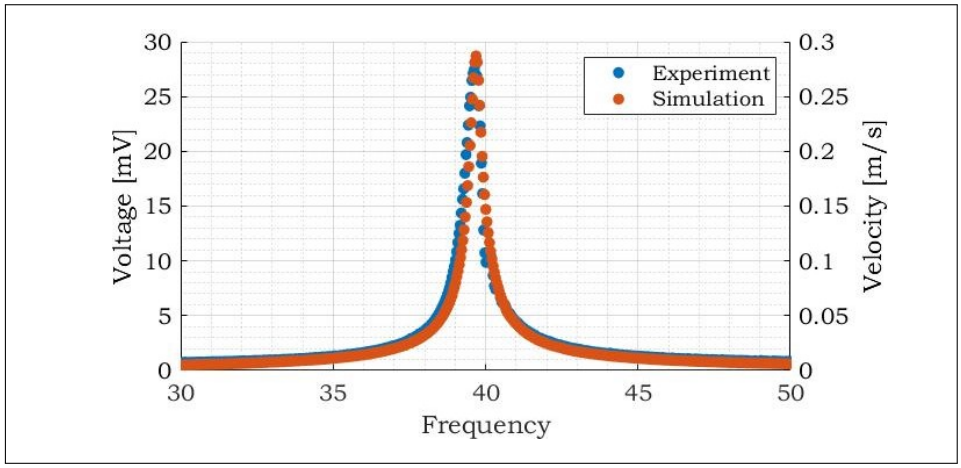

FIGURE 3.4: **Simulated proof mass velocity plotted together with the experimental voltage response on a 0.1g frequency sweep. Both values are the RMS of the oscillation. Analysis showed an electromagnetic constant of $\Phi = 0.09$ as a result of the voltage over the velocity.**

3.3.2 Experimental acceleration data

Figure 3.5 shows the acceleration data of the real world and lab experiments. It can be seen that the FFT analysis, Figure 3.5a, is the same response for all three experiments. The acceleration data from the power spectrum controller experiment, Figure 3.5b looks different than the acceleration data of the wave replication experiment, Figure 3.5c and the real world measurement performed on the engine suspension of the Suzuki Swift, Figure 3.5d

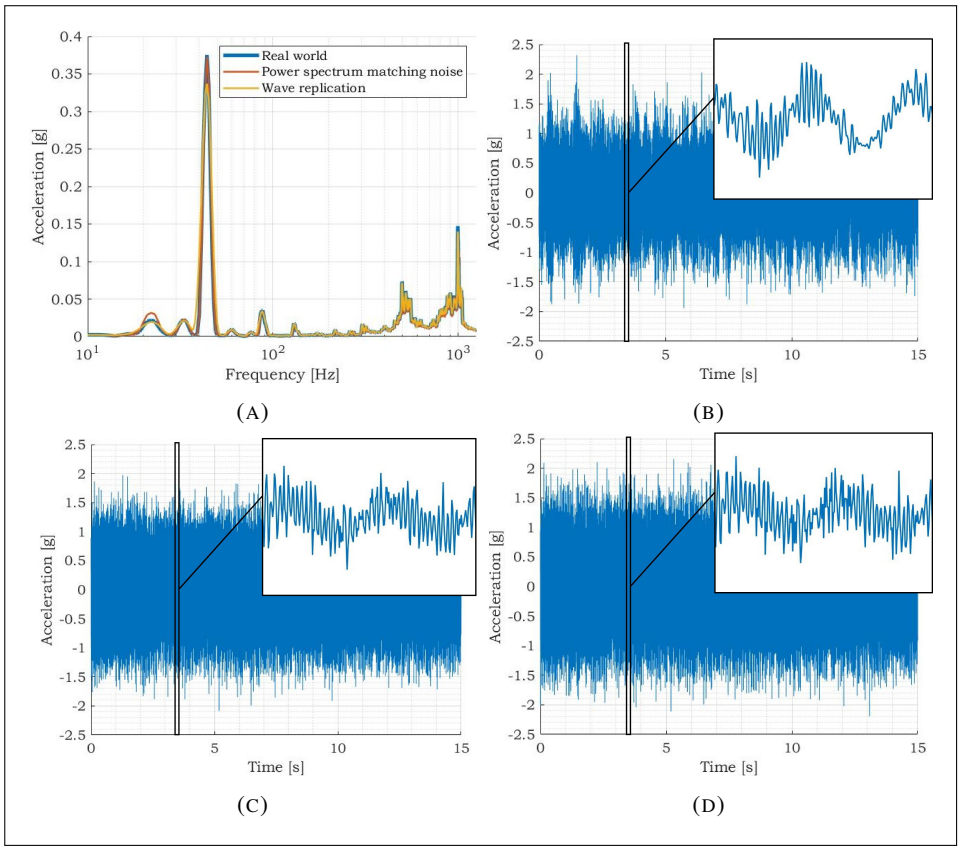

FIGURE 3.5: **FFT analysis belonging to the different experiments (A) and the acceleration data of the shaker power spectrum controlled (B), shaker wave replication (C) and the field experiment (D).**

3.3.3 VEH power output

Figure 3.6 shows the experimental and simulated RMS power output of the VEH. Note the difference between the experimental and simulated output values for the power spectrum matching method in both cases.

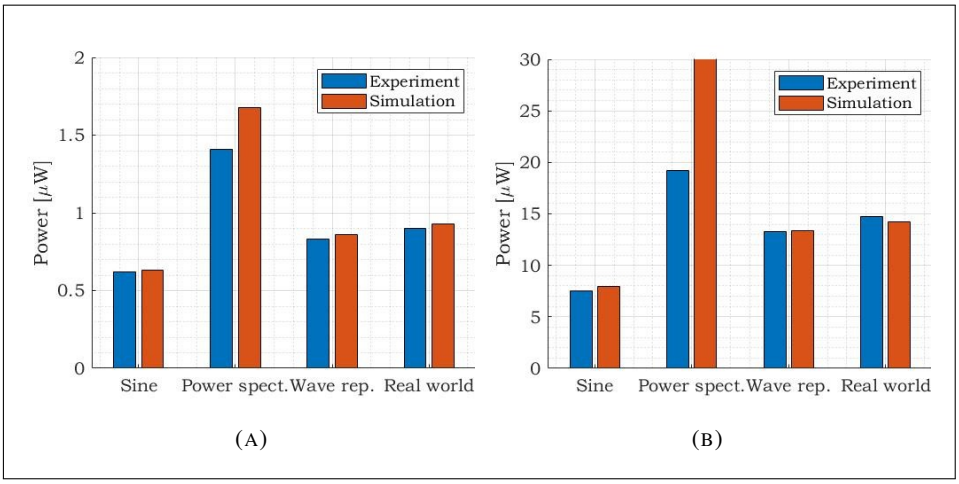

FIGURE 3.6: **Experimental and simulated results of the sine frequency sweep, power spectrum matching noise, wave replication and real world experiments based on the Suzuki Swift experiment (A) and the Volvo V50 experiment (B).**

3.4 Discussion

3.4.1 Frequency sweep experiment

Even though the field experiments were carried out at an arbitrary case where the engine RPM was kept at a constant level, so that one significant dominant frequency was present in the vibrations, Figure 3.5a, the sinusoidal vibration still showed roughly 50% error in the power output with respect to the real world measurement, Figure 3.6. In a frequency sweep, the instantaneous power is concentrated in one single frequency, while in the real world a broad range of frequency content is present. Hence, it is plausible that the presence of other, non-dominant, frequency content influences the performance of the harvester. It is assumable that the obtained performance will deviate more from the frequency sweep when the field experiments are not performed at an arbitrary case with a constant signal.

3.4.2 Power spectrum experiment

The amplification and attenuation characteristics can also clearly be seen in figure 3.5b. Here the power spectrum matching measurement has on average the same power per frequency as the field experiment, however there are much more amplitude fluctuations . This as a result of the FFT/IFFT simulation technique, where all the vibration characteristics other than the power spectral density function are lost. The fluctuations in amplitude can also clearly be seen in the VEH's voltage output. The generated voltage has significantly higher amplitude fluctuations, which results in an overestimation with respect to the field measurement. Due to the higher accelerations, the magnets move outside the coil area which results in nonlinear transducer behavior. This phenomenon is not take into account in the simulation, which explains the large difference between the simulation and experiment.

The power spectrum matching controller can be made more representative for the specific real world vibration by adding more information. Controlling the kurtosis, skewness and crest factor of the real world vibration will make the generated waveform more representative, but not a replica [46].

3.4.3 Wave replication experiment

The real world replication showed almost the same VEH performance as the field measurement. A small performance difference of 7%, between the field measurement and the lab environment replication can be dedicated to the error in the acceleration profiles, which was $0.14g$ and $0.77g$ RMS for the two car experiments. Also the location of the accelerometer was not exactly at the center of the VEH mount, which allowed for some small error due to rotational accelerations.

It should be kept in mind, that the results found for the harvester performance are not universally applicable. This due to selected conditions as engine RPM, location of the VEH and the type of VEH.

3.4.4 Recommendations

For further research, the frequency sweep or noise signal testing should still remain one of the basic experiments for VEH performance. The frequency sweep is well suited to gain insight in the order of magnitude of the power generated and compare this to other VEH designs. However, to take the next step towards VEH implementation, it will be necessary to test or simulate on the real world-like signals. The design of additional tests to predict the VEH performance in various real world applications would form an interesting field of research.

3.5 Conclusion

In this work we simulated a vibration energy harvester on real world vibrations and benchmarked the various test methods for vibration energy harvester performance. Therefore, a linear resonance harvester has been field tested on the engine of two running cars and three different lab experiments have been performed using an electrodynamic shaker; a sinusoidal frequency sweep, power spectrum matching noise and field measurement wave replication. Comparing the lab experiments to the real world, the frequency sweep showed an underestimation of roughly 50%, the power spectrum matching noise experiment made a 50% overestimation and the field wave replication remained within the 7% error. It can be concluded that, vibration energy harvester experiments based on sine or noise signals are useful to compare different systems on the same, commonly used, input signal. However, additional tests, like the field measurement wave replication or a real world signal simulation, should be performed to make claims on the real world performance.

4

Reflection, conclusions and recommendations

This chapter reflects on the approach, process and practical work during the graduation project. An overview of the research activities is presented and some of the successful and unsuccessful activities are discussed in further detail. Finally, the most important conclusions of the project are stated and recommendations for further research are proposed.

4.1 Overview of research activities

A schematic overview of the research activities is shown in figure 4.1. In total, the graduation project spanned a time-line of 15 months, from September 2019 till December 2020. During this time, the research resulted in three different shaker controllers implemented on a cRIO, two harvester prototypes and two papers. Also was contributed to a different project called "Project Mask", where various test equipment was designed and constructed to examine face masks for the Covid-19 pandemic. A collaboration paper on the project was published [10].

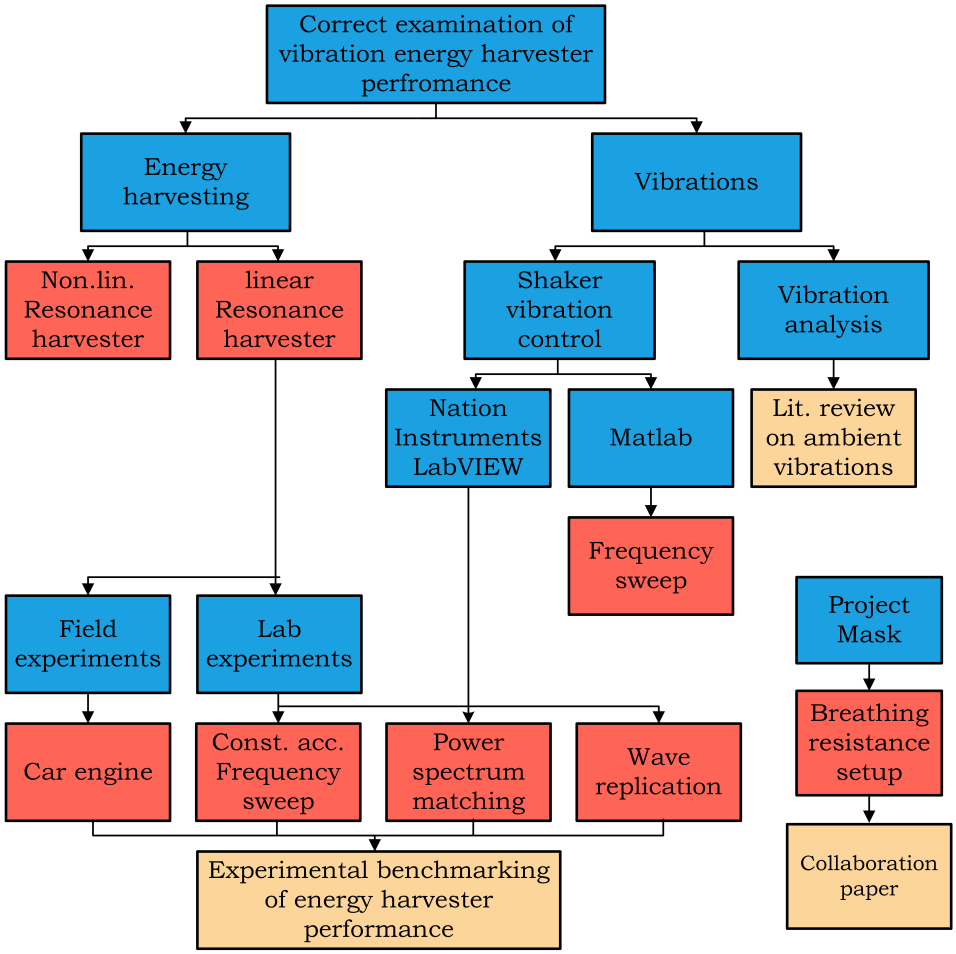

FIGURE 4.1: **Schematic overview of the research activities and achievements made during the graduation project. The general line of research is indicated in blue, red indicates experimental or practical work and in yellow the produced articles are indicated**

4.2 Successes

During the graduation project, many achievements have been made. Not every achievement contains scientific value. Generated resources and experimental setups can be of a great value for successive research. In the author's mind, the greatest successes of this project are the learning process and the practical implementation of shaker controllers. These topics will be discussed in further detail.

4.2.1 Learning process

In view of the author, running a project from *'A'* to *'Z'* was one of the greatest achievements made during the graduation project. In the literature phase, searching the enormous pool of information for the missing link you want to investigate. It took almost half an year to find out that the majority of vibration energy harvesters are solely tested in lab conditions, where the authors attempt to make their new energy harvester design perform better than other designs by tuning the input conditions. Therefore, during the literature phase was attempted to create a bridge between the lab and real world by creating an overview of the variety in real world vibrations. Successively, a follow-up research had to be formulated and carried out. Performing the experimental part of the project, was a learning process on it's own. Some minor things, which seem really straightforward can be very challenging and time consuming. Configuring and programming the setup from scratch resulted in a thorough understanding of the possibilities and limitations of the available lab equipment. Knowledge from various control system design courses needed to be expanded for a practical implementation.

Near the end of the project, when al the practical and experimental work was finished. The usefulness and results of the study need to be communicated to others. Just presenting the data on its own is not sufficient. You need to get and keep everyone's attention during the presentation of your work. It took multiple iterations to obtain a catchy and in the same time scientifically correct presentation of my graduation project.

Furthermore, other general skills were learned during the project. These skills include academic writing, programming in LabVIEW, sparring with peers on difficult questions, prototyping, presenting, dealing with setbacks, planning and management of your own research project.

4.2.2 Practical implementation

The first thing learned during the practical work, was the huge difference between simulation and actual experiments. The most difficult task was to design and implement controllers for the electrodynamic shaker. In the first eyesight seems a vibration shaker one of the most simple dynamical systems, a moving mass suspended by leaf springs with one actuator. The acceleration, which is directly coupled to the actuation force, should be easy to control. Which genuinely is the case, in theory. In practice, the system does not only exist of the shaker, but also the control hardware needs to be taken into account. The National Instruments modules are capable of sending and sampling data at very high rates, but there is a time delay of several milliseconds. It took over 4 months to conclude that the standard PID controller will not work using the available setup because of too large internal delays.

Besides the differences between simulation and the real world implementation, some challenges needed to be overcome on the hardware implementation itself. The National Instruments hardware has enormous capabilities in the field of sensing, control and actuation. However, due to the huge amount of opportunities with the hardware, programming and implementation on the hardware has become a study on it's own. (Some problems could even not be explained by the NI tech support) During the bachelor and master study, some basic courses in LabVIEW were offered, however this never got any further than some basic sensor data reading. The implementation of a controller, which includes FPGA programming, requires a much deeper understanding of the programming language and hardware. In the end, three working controllers have been designed for the electrodynamic shaker. These controllers are able to perform a constant acceleration frequency sweep, generate a noise signal with a predefined power spectrum and replicate a measured acceleration signal. Because of this, the value of the vibration shaker setup itself has increased significantly for research purposes.

4.3 Unsuccessful attempts

4.3.1 Magnetic spring resonance harvester

The focus of the graduation project was on the comparison of lab and real world energy harvester power output. In order to perform test on the various input vibrations, a vibration energy harvester was needed. In the first instance, was chosen for an electromagnetic spring harvester as presented in the study of Geisler et al. [20]. The design was proven to be reliable and being able to generate a sufficient amount of power to see clear distinctions between the various inputs. Also the author was

familiar with the design and production process from the bachelor end project. In two weeks, the modeling was finished, parts were ordered and the vibration energy harvester was constructed. The (range of) resonance of the nonlinear resonance harvester was around 20 to 30Hz, which would be ideal for energy harvesting on a stationary running car engine. However, in the same frequency band was the suspension mode resonance of Lab's vibration shaker, which made the control in that frequency band more difficult. Also, in a progress meeting with senior supervisor Jo Spronck, a linear resonance harvester was advised, to prevent difficult nonlinear effects during the experiments. Therefore, it was chosen to construct a cantilever beam resonance harvester, which is (for low accelerations) a linear system.

An earlier discussion and reflection on the design plans could have prevented the effort made for the nonlinear resonance harvester. A good lesson to always overthink and reflect on your progress during the project.

4.3.2 Feedback controller design

A tremendous amount of effort was put in the design and implementation of the controller for the electrodynamic shaker. In February, the discussion for the need of a shaker controller arose and it was assumed to be an easy job. So, the design of a feedback controller using the the "standard" rule of thumb PID settings was started with the help of Niranjan Saikumar, Hassan HosseinNia and Ali Ahmadi Dastjerdi. When the controller was designed, the shaker plus controller system was implemented in Simulink where it seemed to work. After a long procedure to implement the controller on the cRIO using LabVIEW, instability errors occurred. It was assumed to be a control issue, so many different controller transfer functions were designed using the loop shaping tool 'Shapeit' and successively implemented on the cRIO. After a long time, two major problems arose: First, the cRIO modules were not included in the system identification. The modules in the cRIO have an internal delay in the order of milliseconds, which makes the design of a feedback controller with a several hundred hertz bandwidth almost impossible because of phase issues. Second, the *"discrete transfer function"* block in LabVIEW does respond differently on various amplitude inputs, which complicated the implementation of a transfer function and made troubleshooting almost impossible. In the end was chosen for three different controller designs, as described in appendix C. Reflecting on the controller design procedure, lots of time could be saved when was started by looking in the literature for state of the art electrodynamic shaker controller designs and implementations.

4.4 Conclusions

Vibraton energy harvesting forms a promising source of energy, but some steps from design to actual implementation need to be taken. A classification method for real world signals has been presented, where a classification based on shock, dominant frequency and noise content in the various signals was made. It was found that the signal power, of real world vibrations, was never contained purely in dominant frequencies or shocks. Because the large variation among different real world vibrations, the intended application should always be taken into account during the design and experimental validation of a vibration energy harvester.

Two different experiments for motion energy harvester performance were found as standard in literature; the sinusoidal frequency sweep and Gaussian noise vibrations. These experiments are commonly performed with the use of an electrodynamic shaker. In order to perform the experiments properly, two different controllers have been designed and successively implemented on a cRIO. The first controller was designed to perform a frequency sweep at constant acceleration and the second controller was designed to match the power spectrum of the noise, to the power spectrum of the field measurement. A third controller was designed to reproduce the acceleration wave measured during the field measurement. Based on the comparison between lab and real world experiments can be concluded, that the standard lab tests give an over or underestimation of 40% to 100% compared to the field measurement. The wave replication experiment results in less than 7% error in generated power compared to the field measurement. Therefore, vibration energy harvester experiments based on sine or noise signals are useful as system identification on the same, commonly used signals, to compare different energy harvesters. However, additional tests, like wave replication, should be performed to make claims on the real world performance.

4.5 Recommendations

The performed research indicates that standard vibration energy harvester tests, like the frequency sweep and noise experiments, are unable to predict the real world performance accurately. The proposed solution, wave replication, is a way to test an energy harvester properly for a specific real world application. But, this will only result in the performance for a very particular case. It would be very interesting to design a series of tests which can link energy harvester performance to the characteristics found in all kinds of real world vibrations. So in the end, when energy harvesters become commonly used as a source of power, the best vibration energy harvester can be selected based on a list of characteristics.

Below, some general remarks are listed for future work.

- During the project formulation procedure, take all the steps needed towards the final result into account. Search on every step for some background information to obtain a deeper understanding and indicate the amount of work per step.
- When programming in LabVIEW or performing experiments in general, build the program or experiment step by step. Start with some very basic, straightforward or fundamental principles. When everything is correct, add one element and check the results again. When multiple variables are changed at a time, troubleshooting will become significantly more difficult.
- When you want to build, design or write something, first search in literature whether it already has been done. This could save lots of time in the design progress and problems could be prevented.
  Better well stolen (with correct references) than badly invented.
- Do not follow the advice of any supervisor or source blindly, always keep a good overview of the project. It is easy to lose track by adding too much detail.
- 3D printing is nice for prototyping, but the material characteristics are never the same. Some minor offset can have significant dynamical effects. Machined prototypes made of PMMA, Aluminum or steel are more reliable.

4

Acknowledgments

First of all, I am fortunate to have many friends supporting me. Not only my study and project related relatives have been supporting, but also my friends from home, water polo and work at Kwekerij Verboom helped me with the necessary distraction from the graduation project.

A few persons fulfilled a major role in the execution of this research. In specific, I would like to thank my supervisors Thijs Blad and Jo Spronck. Jo for his very precise questions and remarks on the course of the project, this really encouraged me to take a critical attitude towards my own project and let me think on how to present the results in an effective way. Thijs, for being supportive throughout the whole project. Always when a path seemed to reach a dead end, Thijs came with new suggestions. Not always the greatest, but eventually it helped me forward somehow.

Secondly, I would like to thank the "Stroomgraaiers" for the opportunity to discuss the problems and results encountered during the project. Especially, Stefan Molenaar, Armin Numić, Erik van de Wetering and Kylian van Puffelen for also providing an infinite amount of memes, caffeine and cake. Giving me some relaxation during the long days at the lab.

I would like to thank my family and particularly my parents, Piet and Sonja, for making it possible to complete my study. Although most of my study was a kind of magic for them, they were always interested in my day at TU Delft and the course of the project.

4

A

A

Vibration energy harvester test setup

To perform a proper measurement, you need to be familiar with your test equipment and know their weaknesses. This appendix states the test setup, constructed in order to conduct the experimental part. The first section gives a general overview of the components commonly used to test vibration energy harvester performance in a lab environment. Thereafter, the test equipment used during the experiments has been set out with the some of the specifications per component.

A.1 Components block scheme

The electrodynamic shaker can be seen as the heart of the vibration energy harvester test setup. To make the shaker vibrate, various components are needed. The setup can be made as extensive as desired, depending on the requirements. But in the basics, a signal needs to be generated and sent to the shaker. Most times, the generated signal is not strong enough to actuate the shaker. Therefore, a power amplifier is placed in between. The shaker vibrations need to be monitored with a sensor. Preferably the sensor data is processed somewhere in order to validate the motion. Together with the motion of the shaker, it is desired to monitor the performance of the vibration energy harvester under test. All these processes can be summarized in one single block diagram, figure A.1.

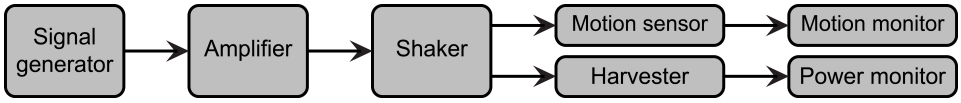

FIGURE A.1: **Bock diagram of the basic processes needed for a vibration energy harvester test setup.**

A.2 Lab equipment

In order to perform the experiments, it was desired to control the shaker's acceleration. Therefore, a controller is implemented on the NI cRIO-9040, which has a built-in FPGA module for fast and accurate signal processing. A signal is generated on the PC or on the real time or the FPGA module of the cRIO. A NI-9260 analog output module sends the generated signal, through the amplifier to the shaker. A PCB accelerometer is attached on top of the shaker table and measures the acceleration. The analog acceleration sensor is directly connected to the NI-9234 module, which is an IEPE analog input, filter and signal conditioner in one. The NI-9234 module placed in the cRIO which processes the acceleration data and communicates with the PC, where the data is stored for further analysis. An overview of the connections and modules is shown in figure A.2.

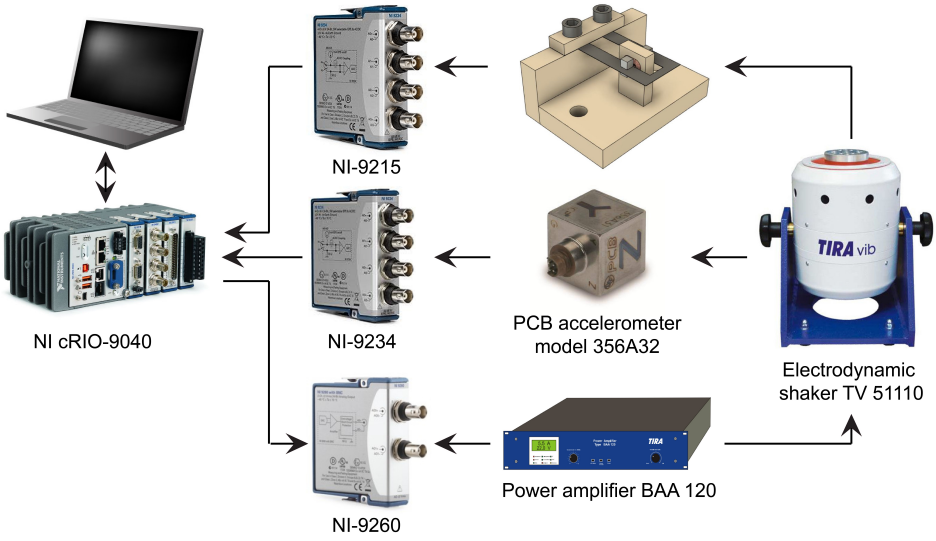

FIGURE A.2: **Schematic representation of the test setup, showing the different components used during the experimental part.**

A.2.1 Equipment specifications

NI cRIO-9040 [4]
The Compact Reconfigurable I/O, or better known as the cRIO is an embedded system that runs a real-time operating system and contains an user programmable FPGA (Field Programmable Gate Array). The real-time operating system is able to control the FPGA during operation for ultra high speed signal generation and data processing. The cRIO also contains four slots in which I/O modules can be placed. These modules can be used to control machines or interact with sensors. Depending on the application the desired module can be placed in the cRIO. Some of the cRIO-9040 features are displayed in table A.1.

TABLE A.1: **Short specification list of the NI cRIO-9040 used during the lab experiments.**

Processor	1.30 GHz Dual-Core
RAM memory	2 GB
Storage	4 GB
FPGA module	Kintex-7 70T
Number of I/O slots	4
Connectivity ports	Gigabit Ethernet, USB 3,1 USB 2.0, RS232 and RS485

NI-9260 [2]
The NI-9260 C Series Voltage Output module is an instrument-grade dynamic signal generator. The module has a build in signal conditioner for the digital to analog conversion. This means that the module increases the sample frequency, by interpolating the digital output and has an internal low pass filter which removes signal content above the sample frequency. Some important specifications are displayed in table A.2.

TABLE A.2: **Short specification list of the NI-9260 used to send the generated waveform to the amplifier.**

Digital resolution	24 Bit
Maximum voltage output	3 V rms
Number of AO ports	2
Max. sample rate	51.2 kHz
Output state Power-on impedance	10 kOhm
Signal conditioning	Digital frequency up-sampling + Analog lowpass filter
Output delay	$30.767/f_s + 3.2\mu s$

NI-9234 [1]
The NI-9234 C Series Sound and Vibration Input Module can measure analog signals from integrated electronic piezoelectric (IEPE) and non-IEPE sensors. The module has an internal AC/DC coupling and IEPE signal conditioner. The latter can be used to directly connect an accelerometer or force sensor to the module. Each channel also has built-in analog anti-aliasing filters that automatically adjust to the digital sample rate. Some important specifications of the NI-9234 are displayed in table A.3.

TABLE A.3: **Short specification list of the NI-9234 used to sample the PCB accelerometer data.**

Digital resolution	24 bit
Voltage range	-5 to +5 V
Maximum sample rate	51.2 kHz
Number of AI ports	4
Signal conditioning	Automatically adjustedAnti-Aliasing filter
Input delay	$(40 + \frac{5}{512})/f_s + 2.6\mu s$

NI-9215

The NI-9215 C series Voltage Input Module can be used to measure analog voltage signals. This can be used to connect other sensors, like a distance meter, or to measure the voltage output of the motion energy harvester over a resistance. Some important specifications of the NI-9215 are displayed in table A.4.

TABLE A.4: **Short specification list of the NI-9215, used to measure the generated vibration energy harvester power output.**

Digital resolution	16 bit
Voltage range	-10 to +10 V
Maximum sample rate	100 kHz
Number of AI ports	4
Input port resistance	200 kΩ
Conversion time	4.4μs to 10μs

Electrodynamic shaker TV 51110

The TV 51110 is a vibration test shaker built by TIRA Schwingtechnik. The shaker has a single degree of freedom table with a high cross-axial stiffness. Further specifications can be seen in figure A.3.

TECHNICAL PARAMETERS Vibration exciter S 51110

Rated peak force $Sine_{pk}$/$Random_{RMS}$	100/70 N
Frequency range	2-7000 Hz
Main resonance frequency	>6500 Hz
Max. displacement Peak-Peak	13 mm
Max. velocity Sine/Random	1.5/1.5 m/s
Max. acceleration Sine/Random	45/30 g
Suspension stiffness	8 N/mm
Effective moving mass	0.23 kg
Weight	12 kg
Armature diameter	60 mm

FIGURE A.3: **Technical specification of the TV 51110 vibration shaker**

A

Power amplifier BAA 120

The power amplifier BAA 120, also manufactured by TIRA Schingtechnik, is designed to power vibration test systems. The amplifier can be operated in voltage and current controlled modes. The output can be monitored using the voltage and current monitoring outputs. A current limiter protects the amplifier from instantaneous overloads and continuous power overloads. The specifications are shown in figure A.4.

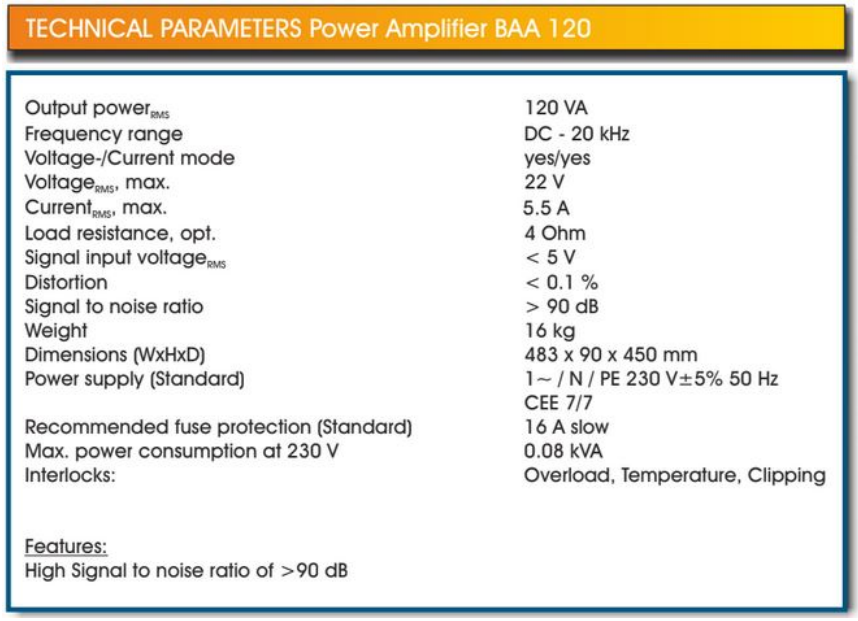

TECHNICAL PARAMETERS Power Amplifier BAA 120

Output power$_{RMS}$	120 VA
Frequency range	DC - 20 kHz
Voltage-/Current mode	yes/yes
Voltage$_{RMS}$, max.	22 V
Current$_{RMS}$, max.	5.5 A
Load resistance, opt.	4 Ohm
Signal input voltage$_{RMS}$	< 5 V
Distortion	< 0.1 %
Signal to noise ratio	> 90 dB
Weight	16 kg
Dimensions (WxHxD)	483 x 90 x 450 mm
Power supply (Standard)	1~ / N / PE 230 V±5% 50 Hz CEE 7/7
Recommended fuse protection (Standard)	16 A slow
Max. power consumption at 230 V	0.08 kVA
Interlocks:	Overload, Temperature, Clipping

Features:
High Signal to noise ratio of >90 dB

FIGURE A.4: **Technical specification of the BAA 120 power amplifier**

PCB accelerometer model 356A32

The PCB accelerometer is a triaxial IEPE accelerometer. An overview of the most important specifications for vibration testing is shown in table A.5.

TABLE A.5: **Short specification list of the PCB accelerometer 356A32, used to monitor the acceleration input of the vibration energy harvester.**

Sensitivity	10.2 mV/(m/s²)
Frequency range	0.7 to 5000 Hz
Resonant frequency	>25 kHz
Measurement range	491 m/s² peak
Overload limit	49.050 m/s² peak

B

Electrodynamic vibration shaker dynamics

Electrodynamic shakers are commonly used to test vibration energy harvester performance in a lab environment. The shaker is a mechanism which turns the electrical signal into an acceleration. Because of the transduction form electrical to mechanical and the internal dynamics of the shaker, will the acceleration signal deviate from the electrical. In order to obtain the same acceleration profile as the input signal, more knowledge on the shaker dynamics is required. This chapter starts with a description of the shaker model, where the internal shaker components are schematically depicted and the transfer function derivation is set out. Followed by the procedure to identify the shaker dynamics and a derivation of the transfer function parameters. Finally, an overview of the equations is given with the results and experimental validation performed for the TV51110 shaker.

"Maak even een controller voor de shaker, zo moeilijk kan dat toch niet zijn?"
Thijs Blad ∼ *januari 2020*

B.1 Schematic mass-spring-damper shaker model

The design of an electrodynamic shaker is very similar to that of a loudspeaker, it is only heavier and more robust. Figure B.1 shows the schematic representation of the shaker. The shaker consists of a body with permanent magnets. On top of the body is an armature suspended by leaf springs which hold the moving part aligned with respect to the body. On top of the armature is the shaker table, on which the specimen can be placed. On the lower side of the armature, the coil is connected with an adhesive bonding. When a current flows through the coil, a force between the coil and permanent magnets in the body is produced. This is called the Lorentz force F_l, eq.(B.1), commonly in the field of electrodynamics designated as the electromotive force F_{em}.

$$\boldsymbol{F_L} = \boldsymbol{I} \times \boldsymbol{B} l n = \Gamma I \tag{B.1}$$

where:

$\boldsymbol{F}_L$ = Lorentz force [N]
$\boldsymbol{I}$ = Electric current [A]
$\boldsymbol{B}$ = Magnetic field [T]
l = length of the coil in the magnetic field [m]
n = Number of windings [-]
Γ = shaker ratio of thrust to coil current $\Gamma = \mathbf{B} l n$ [N/A]

The dynamic capabilities of a shaker can be limited by various factors; for example: maximum stroke, stress-safety factor of the armature, thermal power generated in the coil (I^2/R), capacity of the power amplifier or the modes of vibration [30].

The modes of vibration are generated by the interaction between the various bodies inside the shaker. In order to obtain some more insight on the interaction of the various components, a mass-spring-damper model of the shaker was used. In figure B.2 can be seen that the shaker system consists of three masses, each suspended by a spring-damper, which is able to move in one direction. This gives the system a total of three Degree of Freedom (DoF), where every part has a characterizing eigenfrequency.

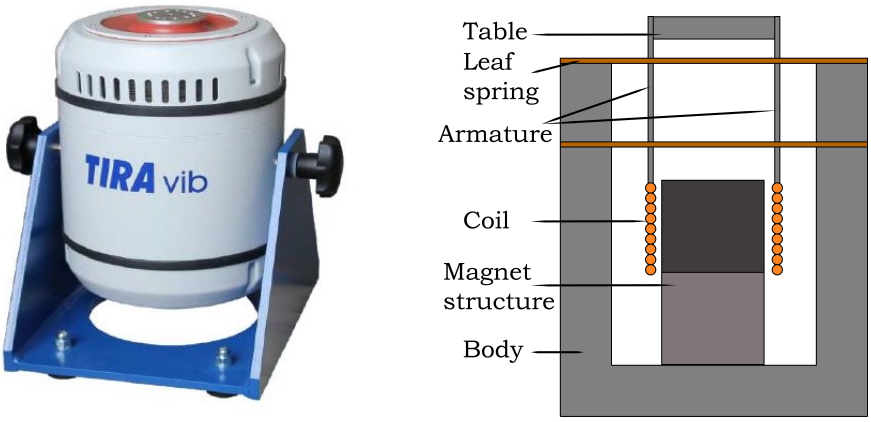

(A) **Vibration shaker** (B) **Shaker cross-section**

FIGURE B.1: **Shaker and schematic cross-section showing the components inside the shaker**

- **Shaker body:** The shaker body is the connection between the other parts and the environment. This body can move with respect to the environment and is characterized by a very low eigenfrequency. The shaker's body eigenmode is called the Isolation Mode.
- **Table:** The table, which is on top of the armature, is connected with the body and the coil. Most electrodynamic shakers have a table eigenfrequency in the range of 10 to 40 Hz and the movement is called the Suspension Mode.
- **Coil:** The coil, which is connected on the lower side of the armature with an adhesive bonding, is connected with the table. When a current passes through the coil, the Lorentz force acts between the coil and shaker body, which will move the two parts with respect to each other. The eigenfrequency of this system is near the upper frequency limit of the shaker, which is commonly in the order of 5 to 10 kHz. The coil starts to move out of phase with respect to the table, which is called the Coil Mode.

Besides the mechanical model, an electrical model of the shaker can be made, which takes the coil's resistance and inductance into account. The coupling between the electrical and mechanical domain is not only indicated by the Lorentz Force eq.(B.1), but also the other way around. When the coil moves with respect to the magnetic field a voltage is generated, called the "back EMF" (ElectroMotive Force) [15]. This back EMF can be seen in the electrical domain as an increase in coil impedance. When the Lorentz actuator is controlled by a voltage source, which ideally has zero source impedance, the back EMF will form a mechanical

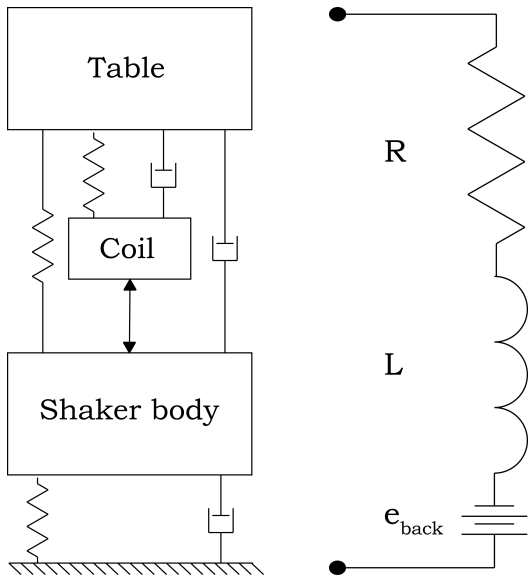

(A) **Mechanical model** (B) **Electrical model**

FIGURE B.2: **A) shaker constructed as mass-spring-damper system, B) electric model of the shaker, build up out of a coil with resistance and back emf**

damping in the system, which will result in non-linear behavior. When the Lorentz actuator is controlled by a current source, which has an infinite source impedance, the small increase in the coil's impedance will be negligible compared to the large source impedance. This will yield in a linear force actuator, the strong positive property of a Lorentz actuator [23].

B.1.1 Transfer function of the schematic model

In order to construct the shaker's transfer function some assumptions are considered for simplification. First, the shaker body is assumed to be rigidly connected to the environment. In reality, this is not the case, but the eigenfrequency of the connection between the shaker and the real world will be below the operative frequency range of the shaker, and therefore left out.
Second, an additional proof mass is assumed to be rigidly connected to the shaker table. Under these assumptions, a two degree of freedom mass-spring-damper system remains. Using the parameters as displayed in figure B.3, the equations of motion for the table and coil body are respectively eq.(B.2) and eq.(B.3).

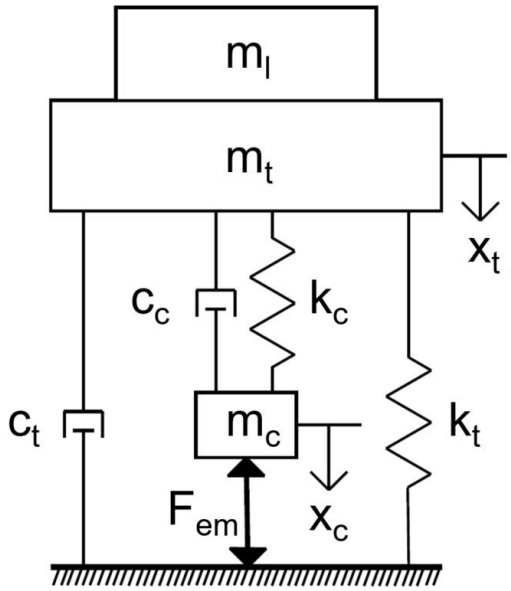

FIGURE B.3: **Shaker mass-spring-damper system simplified for transfer function.**

$$c_c\left(\frac{\mathrm{d}x_c(t)}{\mathrm{d}t}-\frac{\mathrm{d}x_t(t)}{\mathrm{d}t}\right)+k_c\left(x_c(t)-x_t(t)\right)=\left(m_l+m_t\right)\frac{\mathrm{d}^2x_t(t)}{\mathrm{d}t^2}+c_t\frac{\mathrm{d}x_t(t)}{\mathrm{d}t}+k_tx_t(t) \tag{B.2}$$

$$F_{em}=m_c\frac{\mathrm{d}^2x_c(t)}{\mathrm{d}t^2}+c_c\left(\frac{\mathrm{d}x_c(t)}{\mathrm{d}t}-\frac{\mathrm{d}x_t(t)}{\mathrm{d}t}\right)+k_c\left(x_c(t)-x_t(t)\right) \tag{B.3}$$

First, a switch from time to Laplace domain is made by using the Laplace transform. This makes the displacements $x_c(t)$ and $x_t(t)$ a function of s, which will no longer be written to improve readability. The equations of motion in Laplace domain can be written as:

$$c_c\left(x_c-x_t\right)s+k_c\left(x_c-x_t\right)=\left(m_l+m_t\right)x_ts^2+c_tx_ts+k_tx_t \tag{B.4}$$

$$F_{em}=m_cx_cs^2+c_c\left(x_c-x_t\right)s+k_c\left(x_c-x_t\right) \tag{B.5}$$

The current is used to generate the electromotive force F_{em}, eq.(B.1). Not all the parameters required to calculate the electromotive force are known. Therefore, this will be written as eq.(B.6), where Γ represents the thrust coefficient of the coil.

$$F_{em}=\Gamma i \tag{B.6}$$

The next step is to extract the coil displacement x_c out of the equations of motion by rewriting eq.(B.4):

$$0 = (m_l + m_t)\, x_t s^2 + c_t x_t s + k_t x_t - c_c\,(x_c - x_t)\, s - k_c\,(x_c - x_t)$$

$$0 = x_t\left[(m_l + m_t)s^2 + (c_t + c_c)s + k_t + kc\right] - x_c\left[c_c s + k_c\right]$$

B

$$x_c = x_t\left[\frac{(m_l + m_t)s^2 + (c_t + c_c)s + k_t + kc}{c_c s + k_c}\right] \tag{B.7}$$

Successively, eq.B.7 and B.6 are substituted into eq.(B.5):

$$\Gamma i = \left[\left(m_c s^2 + c_c s + k_c\right)\left(\frac{(m_l + m_t)s^2 + (c_t + c_c)s + k_t + k_c}{c_c s + k_c}\right) - \left(c_c s + k_c\right)\right] x_t$$

Expanding the brackets and making the denominator in each term equal, yields the following single fraction

$$\Gamma i = \left[\begin{array}{l} m_c(m_l + m_t)s^4 + m_c(c_t + c_c)s^3 + m_c(k_t + k_c)s^2 \\ \quad + c_c(m_l + m_t)s^3 + c_c(c_t + c + c)s^2 + c_c(k_t + k_c)s \\ \qquad + k_c(m_l + m_t)s^2 + k_c(c_t + c_c)s + k_c(k_t + k_c) \\ \hline \qquad\qquad\qquad\qquad c_c s + k_c \end{array} - \frac{c_c^2 s^2 + 2k_c c_c s + k_c^2}{c_c s + k_c}\right] x_t$$

The final step is to write the equations of motion as a transfer function. This is the relation of the table acceleration $\frac{\mathrm{d}^2 x_t(t)}{\mathrm{d}t^2}$ ($x_t s^2$ in Laplace transform) to the input current i:

$$H_{shaker}(s) = \frac{x_t s^2}{i} = \frac{\Gamma(c_c s + k_c)s^2}{\begin{array}{l} m_c(m_l + m_t)s^4 + (m_c c_c + M c_c)\, s^3 \\ \quad + (m_c k_t + c_c c_t + M k_c)\, s^2 + (c_c k_t + c_t k_c)s + k_c k_t \end{array}} \tag{B.8}$$

where:

$$M = m_c + m_l + m_t$$

B.2 Dynamical transfer function identification

B.2.1 Experimental identification

In the experimental identification, the shaker is fed with a constant amplitude sinusoidal sweep coming from the NI-9260 analog output module. During this sweep the generated signal, amplifier output current and the shaker table accelerations are monitored using the NI-9234 analog input module and stored on the PC via the cRIO-9040, see figure B.4. Successively, the transfer functions of the shaker and power amplifier can be identified according to eq.(B.9) and eq.(B.10) respectively.

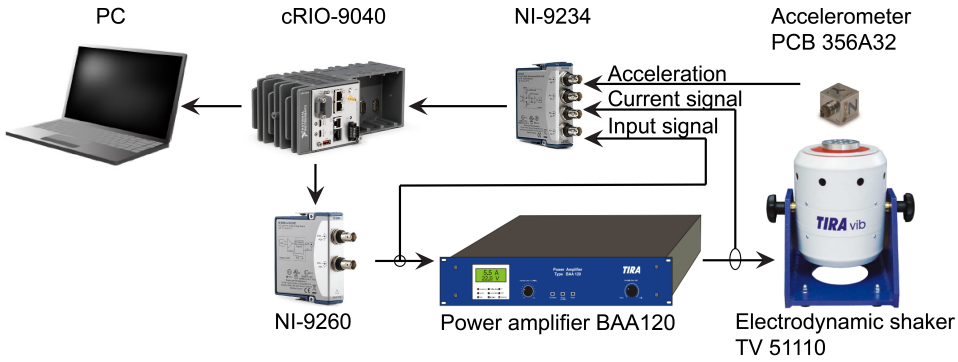

FIGURE B.4: **Schematic representation of the test setup used for shaker dynamics identification.**

$$H_{shaker}(s) = \frac{Acceleration(s)}{Current\ signal(s)} \tag{B.9}$$

$$H_{amplifier}(s) = \frac{Current\ signal(s)}{Input\ signal(s)} \tag{B.10}$$

It is known that the shaker has a suspension mode eigenfrequency between 10 and 40 Hz and an eigenfrequency near 5 to 10 kHz resulting from the coil mode. In order to capture these eigenfrequencies the sweep should start around 10 Hz and end at 10 kHz. This results in a huge frequency range in one sweep, where a trade-off has to be made between sweep time and frequency resolution. Using an exponential increasing frequency sweep improves the resolution at low frequencies, but this is at the expense of the resolution at high frequencies. Because the most interesting parts are at the lower and upper frequency range, it was chosen to cut the frequency sweep in three parts for a higher resolution at the interesting regions:

1. **5 - 50 Hz**, for a higher frequency resolution at the Suspension mode.
2. **10 - 5000 Hz**, less resolution is needed at the "flat region" where no resonances occur.
3. **4000 - 9000 Hz**, a relatively higher resolution at the Coil mode.

The three sweep parts have some overlap; this to reduce uncertainties at the beginning and end of each sweep in the transfer function estimation.

B.2.2 Transfer function variables derivation

The transfer function variables can be found by performing the experimental identification with and without a known mass attached to the table. The first resonance can be devoted to the suspension mode, where the coil-table connection is assumed to be rigid. Therefore, the shaker can be simplified to a single mass-spring-damper system with the following transfer function:

$$H_{suspension}(s) = \frac{\Gamma s^2}{(m_c + m_t + m_l)s^2 + c_s s + k_s} \tag{B.11}$$

The resonance frequency can be calculated using eq.(B.12) or eq.(B.13) depending on the load case.

$$f_{0s} = \frac{1}{2\pi}\sqrt{\frac{k_t}{m_t + m_c}} \tag{B.12}$$

$$f_{ls} = \frac{1}{2\pi}\sqrt{\frac{k_t}{m_t + m_c + m_l}} \tag{B.13}$$

where:

f_{0s} = Suspension mode resonance frequency with zero load [Hz]
f_{ls} = Suspension mode resonance frequency with known load [Hz]

These equations can be rewritten as:

$$m_t + m_c = \left(\frac{1}{2\pi}\right)^2 \frac{k_t}{f_{0s}^2} \tag{B.14}$$

$$k_t = (2\pi)^2 f_{ls}^2 (m_t + m_c + m_l) \tag{B.15}$$

Substituting eq.(B.15) into eq.(B.14) and rewriting, results in eq.(B.16) to calculate the shaker table plus coil mass m_a.

$$m_t + m_c = \left(\frac{1}{2\pi}\right)^2 \frac{(2\pi)^2 f_{ls}^2 (m_t + m_c + m_l)}{f_{0s}^2}$$

$$(m_t + m_c)\left(1 - \frac{f_{ls}^2}{f_{0s}^2}\right) = m_l \left(\frac{f_{ls}^2}{f_{0s}^2}\right)$$

$$m_t + m_c = m_l \left(\frac{\left(\frac{f_{ls}^2}{f_{0s}^2}\right)}{\left(1 - \frac{f_{ls}^2}{f_{0s}^2}\right)}\right)$$

$$m_a = m_t + m_c = \left(\frac{f_{ls}^2}{f_{0s}^2 - f_{ls}^2}\right) m_l \tag{B.16}$$

Equation(B.12) can be rewritten, to calculate the suspension stiffness k_t using the result coming from eq.(B.16):

$$k_t = (2\pi)^2 f_{0s}^2 m_a \tag{B.17}$$

In the second eigenfrequency, coming from the coil mode, the coil and table move out-of-phase. In this eigenmode the suspension stiffness k_t and damping c_t are negligible with respect to the coil bonding stiffness k_c and damping c_c, and will be set to zero [33]. So, the transfer function eq.(B.8) can be rewritten as eq.(B.18) for the coil mode resonance.

$$H_{coil}(s) = \frac{\Gamma k_c}{[m_c(m_l + m_t)]\, s^2 + [(m_a + m_l)c_c]\, s + [(m_a + m_l)k_c]} \tag{B.18}$$

In the transfer function the following equation of motion in Laplace domain can be recognized:

$$Ms^2 + Cs + K = [m_c(m_l + m_t)]\, s^2 + [(m_a + m_l)c_c]\, s + [(m_a + m_l)k_c]$$

Therefore, the coil mode resonance frequency can be calculated using eq.(B.19) or eq.(B.20), again depending on the load case.

$$f_{0c} = \frac{1}{2\pi}\sqrt{\frac{m_a k_c}{m_t m_c}} \tag{B.19}$$

$$f_{lc} = \frac{1}{2\pi}\sqrt{\frac{(m_a + m_l)k_c}{(m_t + m_l)m_c}} \tag{B.20}$$

where:

f_{0c} = Coil mode resonance frequency with zero load [Hz]
f_{lc} = Coil mode resonance frequency with known load [Hz]

These equations can be rewritten as:

$$k_c = m_c(2\pi)^2 f_{0c}^2 \frac{m_t}{m_a} \tag{B.21}$$

$$k_c = m_c(2\pi)^2 f_{lc}^2 \frac{m_l + m_t}{m_l + m_a} \tag{B.22}$$

Equate eq.(B.21) to eq.(B.22) and rewrite, results in eq.(B.23) to calculate the table mass m_t.

$$m_c(2\pi)^2 f_{0c}^2 \frac{m_t}{m_a} = m_c(2\pi)^2 f_{lc}^2 \frac{m_l + m_t}{m_l + m_a}$$

$$f_{0c}^2 \frac{m_t}{m_a} = \frac{m_l f_{lc}^2 + m_t f_{lc}^2}{m_l + m_a}$$

$$f_{0c}^2 m_t (m_l + m_a) = m_l m_a f_{lc}^2 + m_t m_a f_{lc}^2$$

$$m_t \left((m_l + m_a) f_{0c}^2 - m_a f_{lc}^2 \right) = m_l m_a f_{lc}^2$$

$$m_t = \frac{m_l m_a f_{lc}^2}{(m_l + m_a) f_{0c}^2 - m_a f_{lc}^2} \tag{B.23}$$

The table mass m_t and armature mass m_a are known. Only the coils mass m_c is needed to calculate the coil bonding stiffness, using eq.(B.21). The coil mass can be found by looking back at eq.(B.16):

$$m_c = m_a - m_t \tag{B.24}$$

The remaining parameters are the table and coil damping coefficients, c_t and c_c respectively, and the thrust coefficient Γ. These parameters can be evaluated by experimental observations as follows.
The shaker thrust coefficient can be evaluated by looking at the "flat region" shaker gain, which is between the suspension and coil mode resonance frequencies. Roughly ten times the suspension mode eigenfrequency is a good measure of the flat region gain. There is no resonance in the system at the "flat region", so the armature acceleration is purely generated by the electromotive force. Based on eq.(B.6), eq.(B.8) and Newton's second law; $\mathbf{F} = m\mathbf{a}$, the thrust coefficient can be calculated:

$$H_{shaker} = \frac{a}{i} = \frac{\frac{F_{em}}{m_a}}{\frac{F_{em}}{\Gamma}}$$

$$\Gamma = m_a |H_{shaker}(\geq 10 \cdot j2\pi f_{0s})|_{m_l=0} \tag{B.25}$$

The damping coefficients can be determined based on the magnitude of the resonance peaks. The table damping can be found by filling the s from eq.(B.11) in at the suspension resonance f_{0s} without load, $(m_l = 0)$.

$$s = j\omega_n = j2\pi f_{0s} = j\sqrt{\frac{k_t}{m_a}}$$

$$H_{suspension}(s) = \frac{\Gamma s^2}{(m_a + m_l)s^2 + c_t s + k_t} \tag{B.26}$$

$$c_t s = \frac{\Gamma s^2}{|H_{suspension}(s)|} - \left((m_a)s^2 + k_t\right)$$

$$c_t = \frac{\Gamma(2\pi f_{0s})}{|H_{suspension}(j2\pi f_{0s})|} - \left((m_a)(j\left(\sqrt{\frac{k_t}{m_a}}\right)^2 + k_t\right)$$

$$c_t = \frac{2\pi f_{0s}\Gamma}{|H_{suspension}(j2\pi f_{0s})|_{m_l=0}} \tag{B.27}$$

The coil damping can be found by filling the s from eq.(B.18) in at the coil resonance f_{0c} without load, $m_l = 0$.

$$s = j\omega_n = j2\pi f_{0c} = j\sqrt{\frac{m_a k_c}{m_t m_c}}$$

$$H_{coil}(s) = \frac{\Gamma k_c}{m_c m_t s^2 + m_a c_c s + m_a k_c}$$

$$m_a c_c s = \frac{\Gamma k_c}{|H_{coil}(s)|} - \left(m_c m_t s^2 + m_a k_c\right)$$

$$c_c = \frac{\Gamma k_c}{m_a(2\pi f_{0c})|H_{coil}(j2\pi f_{0c})|} - \left(m_c m_t \left(j\sqrt{\frac{m_a k_c}{m_t m_c}}\right)^2 + m_a k_c\right)$$

$$c_c = \frac{\Gamma k_c}{m_a(2\pi f_{0c})|H_{coil}(j2\pi f_{0c})|_{m_l=0}} \tag{B.28}$$

B.2.3 Transfer function parameters of the TV51110

The previous sections describe the dynamics and set out a derivation of the mechanical model of the electrodynamic shaker. This section shows the dynamic identification and the resulting mechanical model of the *TIRA TV51110 electrodynamic shaker*.
Table B.1 shows an overview of all the parameters used in the mechanical model and the equations used to derive them. These equations utilize data found in the dynamic identification. Figure B.5 shows the experimental transfer function of the TV51110 electrodynamic shaker with the magnitude and phase constants needed to fill in the model equations.

TABLE B.1: **model parameters and equations overview**

Symbol	Parameter	Equation	Value
H_{shaker}	Shaker transfer function	(B.8)	$[-]$
m_l	Load mass	[-]	0.357 $[kg]$
k_t	Table stiffness	(B.17)	9.31e3 $[N/m]$
k_c	Coil stiffness	(B.21)	4.38e7 $[N/m]$
m_t	Table mass	(B.23)	0.228 $[kg]$
m_c	Coil mass	(B.24)	0.022 $[kg]$
Γ	Thrust coefficient	(B.25)	16.64 $[N/A]$
c_t	Table suspension damping	(B.27)	2.76 $Ns/m]$
c_c	Coil damping	(B.28)	25.5 $[Ns/m]$

f

After filling in the identification constants found in fig.B.5 in the model equations; the shaker transfer function yields:

$$H_{shaker} = \frac{424.7s^3 + 7.29e8s^2}{0.004567s^4 + 5.888s^3 + 1e7s^2 + 1.212e8s + 4.076e11} \tag{B.29}$$

Finally, the resulting model can be compared with the experimental transfer function by comparing the frequency responses, fig. B.6. In conclusion, the two degree of freedom model assumption is a good approximation of the shaker's dynamic behavior. There is a lot of resemblance over the useful frequency range, but above the coil resonance accuracy is lost. Most likely, this is the result of dynamics due to a minor misalignment in the shaker assembly which is not included in the two DOF model. However, this will be to a lesser extend, because vibration experiments will mainly be performed below the coil mode resonance.

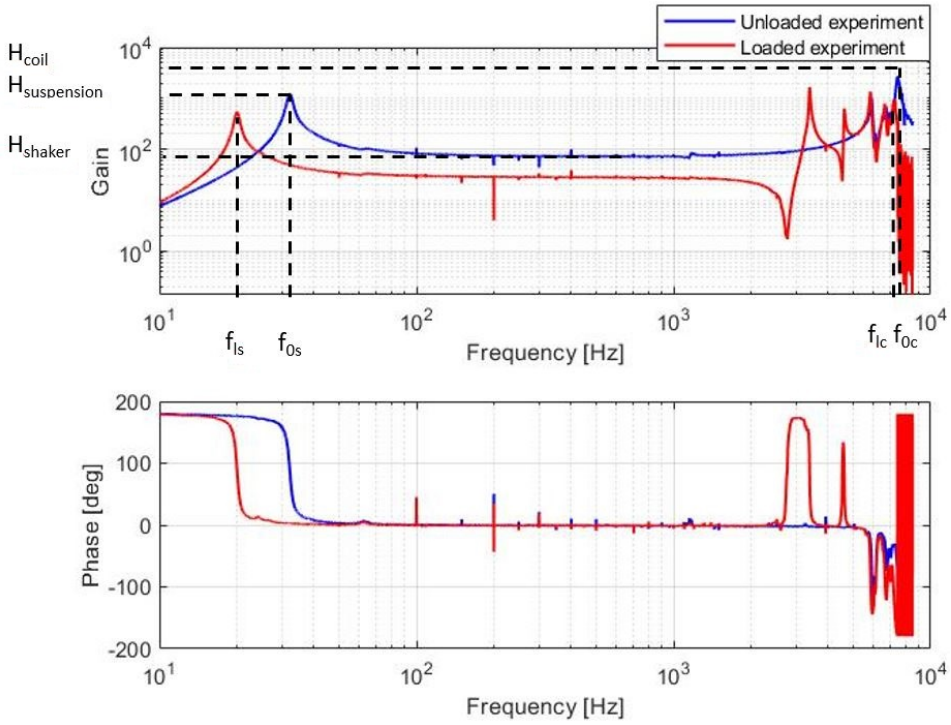

FIGURE B.5: **TV51110 vibration shaker transfer function found with the experimental identification. The Suspension mode, coil mode and flat region gain are identified in the unloaded experiment together with the resonance frequencies of the loaded and unloaded experiment. These variables can be used to fill in the model equations and derive the transfer function of the shaker.**

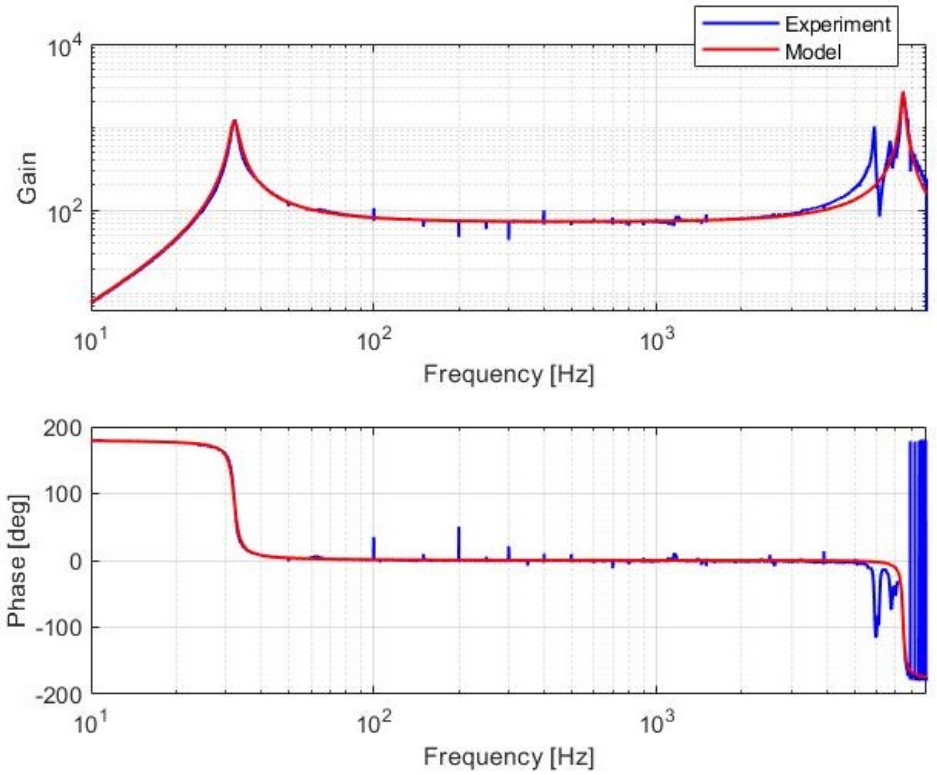

FIGURE B.6: **Experimental and simulated frequency response of the TV51110 electrodynamic shaker without load.**

C

Electrodynamic shaker controller

The controller design was implemented on the National instruments hardware using the corresponding programming software: LabVIEW. This should be an intuitive program to make programming on, for instance, an FPGA accessible. However, the design and implementation of the various controllers still required lots of iterations, according to PHD candidate Nima Karbasizadeh; "Mechatronic system design is a matter of persistence."

Eventually, three different controllers are designed and implemented. Each controller is designed for a specific type of signal generation and controls. Each section starts with the control structure, followed by the LabVIEW implementation and ends with the characteristics and performance of the generated acceleration.

The electrodynamic shaker can be used to replicate various vibration test conditions. Each vibration test has it's own set of boundary conditions and requirements. Ideally, one controller design would be able to perform all the test. However, because the perfect controller does not exist, it is very hard to satisfy all the requirements in one controller design. Therefore, multiple controllers are designed, which have their own specific purpose. [3].
In line with the state of the art shaker control software, three different controllers are designed. Each controller can be implemented on a National Instruments compact RIO chassis using the LabVIEW software package. The first controller, *Frequency sweep controller; RMS based*, is specifically designed to perform a sinusoidal excitation on the shaker. The second controller, *Random signal controller; FFT based* generates a random excitation on the shaker build of a predefined frequency spectrum profile. Lastly, the third controller, *Time Waveform Replication; FF*, is able to reproduce a measured acceleration signal using feed-forward control.

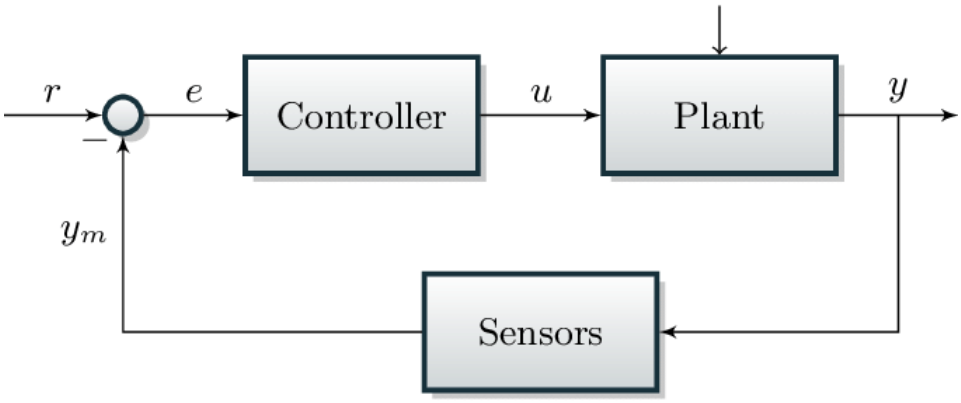

FIGURE C.1: **Basic closed loop control system principle**

C.1 Frequency sweep controller; RMS based feedback

The control loop of the RMS based controller is the same as the basic feedback control loop. The output signal of the plant, y, is compared to a reference, r. The controller responds on the resulting error, e, and generated an output signal, u, to drive the plant, Figure C.1.

In the case of the Frequency sweep controller is not the entire output of the plant's signal used as reference, but only the amplitude of oscillation is of interest, see Figure C.2. When the acceleration profile is assumed to be a sinusoidal wave, only the acceleration amplitude needs to be controlled. Because the acceleration

signal contains noise and small spikes, the maximum acceleration will give an incorrect representation of the total sinusoidal wave amplitude. The relation between the RMS of a sinusoidal wave and the amplitude, $Amplitude = \sqrt{2} \cdot RMS$, can be used to determine the acceleration level more precisely. Therefore, the feedback elements do not consist of all the acceleration data points, but of the RMS acceleration level for a given time interval. Successively, the RMS feedback elements are compared with the desired acceleration level, resulting in the error to fed the controller. At the controller's output is the actuation amplitude, which determines the amplitude of the sinusoidal actuation signal generated by the sine wave generator.

The controller consists solely of a proportional gain. Based on the factor between the reference and feedback amplitude is the error obtained. Based on the input error, a new actuation amplitude is determined by the controller based on equation (C.1).

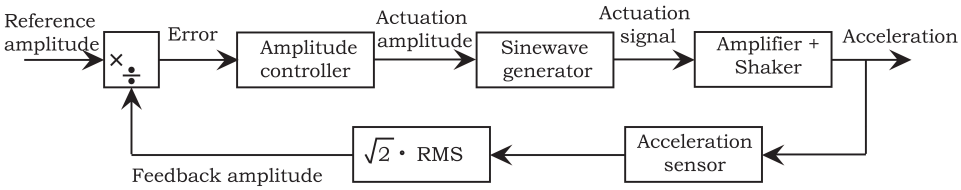

FIGURE C.2: **Frequency sweep controller block scheme**

$$A_{i+1} = \begin{cases} A_i \times \frac{K+1/r}{K+r} & \text{if } r \leq 1 \\ A_i \times \frac{K+1}{K+r} & \text{if } r > 1 \end{cases} \tag{C.1}$$

where:

A_{i+1} = New actuation signal amplitude
A_i = Current actuation signal amplitude
r = Error: acceleration over reference $r = \frac{RMS_{acc}}{RMS_{ref}}$
K = Compress factor

The response of the controller can be tuned using the compress factor K, which controls the proportional gain of the controller. A lower value of K results in a faster response to errors. But when the value of K is set too low, chances of overshoot and destabilization arise.

C.1.1 LabVIEW design

To implement the controller on the experimental setup as depicted in Figure A.2, the cRIO has to be programmed using LabVIEW. The LabVIEW project on the frequency sweep controller is build as a three level virtual interface structure, Figure C.3.

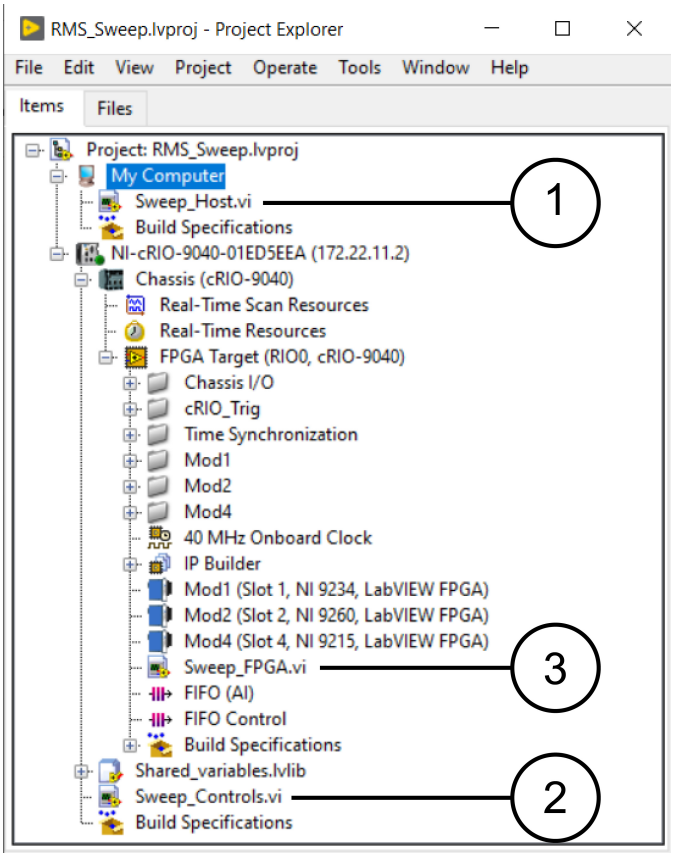

FIGURE C.3: **Frequency sweep controller; LabVIEW project explorer interface**

The first virtual interface, *Sweep_Host.vi*, runs on the hosting computer or laptop. This virtual interface is used to store the experimental data on the computer which can be used for further analysis.
The second virtual interface, *Sweep_Controls.vi*, runs on the real time module of the cRIO. This virtual interface is used to set the frequency sweep settings and monitor and control the acceleration level during the sweep. The settings can be entered on the front panel, Figure C.4. Table C.1, shows a brief description of the in- and output parameters of the *PSD_controls.vi*. The programming in labview

is performed in a block diagram as shown in Figure C.6. The *Sweep_Controls.vi* block diagram consist of a three stage sequence. In the first frame, the connection between the real time controller and the FPGA is made. Also the additional analog input ports and data rates can be selected. The second frame contains two while loops, one is a timed loop to update the frequency during the sweep. The second while loop contains the control part and runs as fast a possible. In this loop, the acceleration data is obtained and stored in a buffer. The RMS acceleration is taken from the data in the buffer and compared to the reference acceleration level. Successively, the obtained error value is fed to the controller which alters the actuation signal according to equation (C.1). During the sweep, the acceleration and RMS data ar plotted in two graphs to monitor the process. When the while loop is terminated, the FPGA is disconnected and the script is aborted.
The third virtual interface, *Sweep_FPGA.vi*, runs on the FPGA of the cRIO. This virtual interface forms the connection between the real world and the real time controller. The control commands come from the *Sweep_Controls.vi* and the sinusoidal wave is generated and sent by the analog output module. The real world data is read by the analog input modules and sent to the *Sweep_Controls.vi* and *Sweep_Host.vi*.

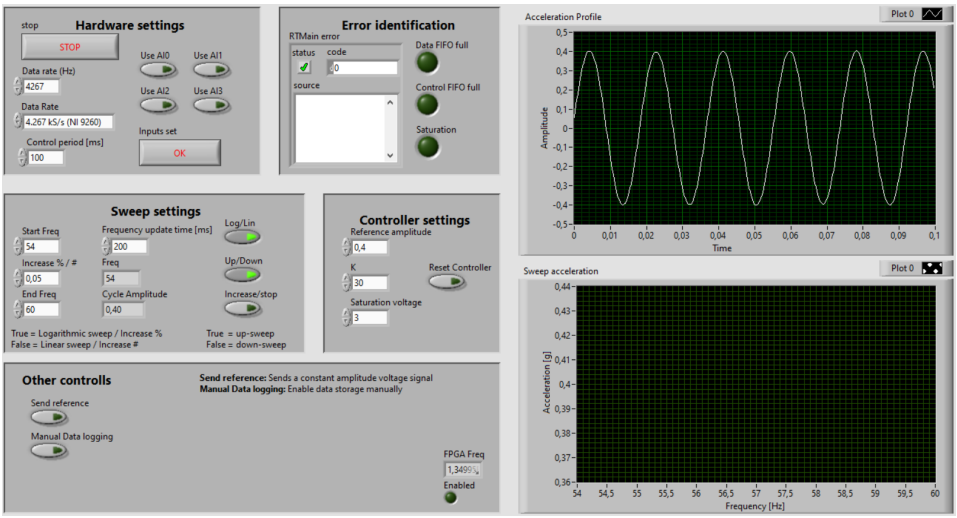

FIGURE C.4: **Frequency sweep controller; controller front panel**

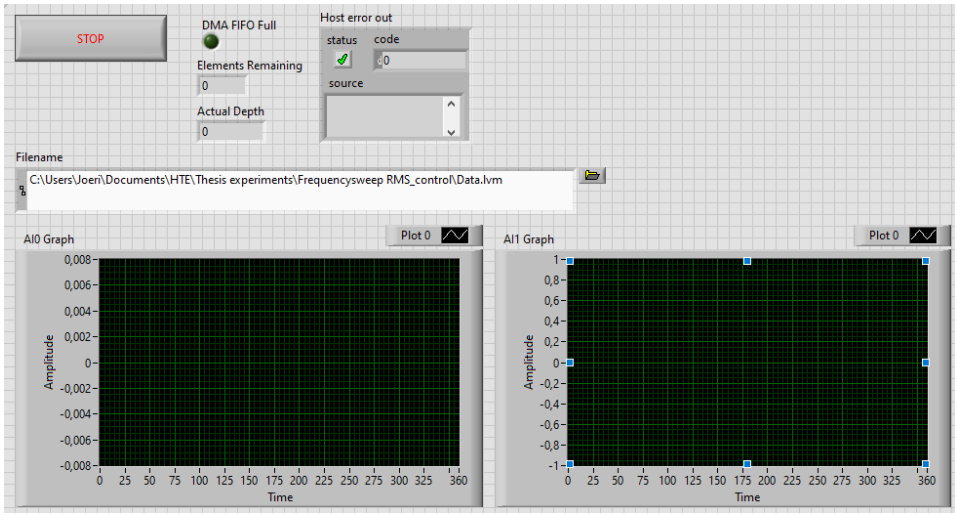

FIGURE C.5: **Frequency sweep controller; host front panel**

TABLE C.1: **Input and output description of the *Sweep_Controls.vi* front panel**

Input / Output	**Description**
Control period (ms)	Period to determine the sine wave RMS value
Data rate (Hz)	Same as "Data Rate", only numerical entered
Data Rate	Sample frequency of the analog in- and output modules
Use AI0	Enable Analog input 0 to measure more sensor data
Use AI1	Enable Analog input 1 to measure more sensor data
Use AI2	Enable Analog input 2 to measure more sensor data
Use AI3	Enable Analog input 3 to measure more sensor data
Stop	Exit controller script
Inputs set	All hardware settings are set; continue to sweep settings
RTMain error	Error output for the controller virtual interface
Data FIFO full	Indication of an error in the FPGA-Host data flow
Control FIFO full	Indication of an error in the FPGA-Controller data flow
Saturation	Indication of overflow in the output voltage
Start Freq	Lowest frequency of the sweep [Hz]
increase % / #	Frequency step size of the sweep in percents of absolute value
End Freq	Highest frequency of the sweep [Hz]
Freq	Indication of the current frequency during the sweep [Hz]
Cycle Amplitude	Indication of the current amplitude during the sweep [g]
Log/Lin	Switch button to select a linear of logarithmic sweep
Up/Down	Switch button to select an increasing or decreasing sweep
Increase/stop	Toggle button to start or exit the frequency sweep
Reference amplitude	Reference value for the desired acceleration amplitude [g]
K	Controller compress factor
Saturation voltage	Maximum output voltage to prevent overload
Reset controller	Toggle button to reset the controller when the output doesn't converge
Send reference	Switch button to send a constant amplitude voltage signal during the sweep
Manual data logging	Switch button to save the acceleration and AI data outside the sweep

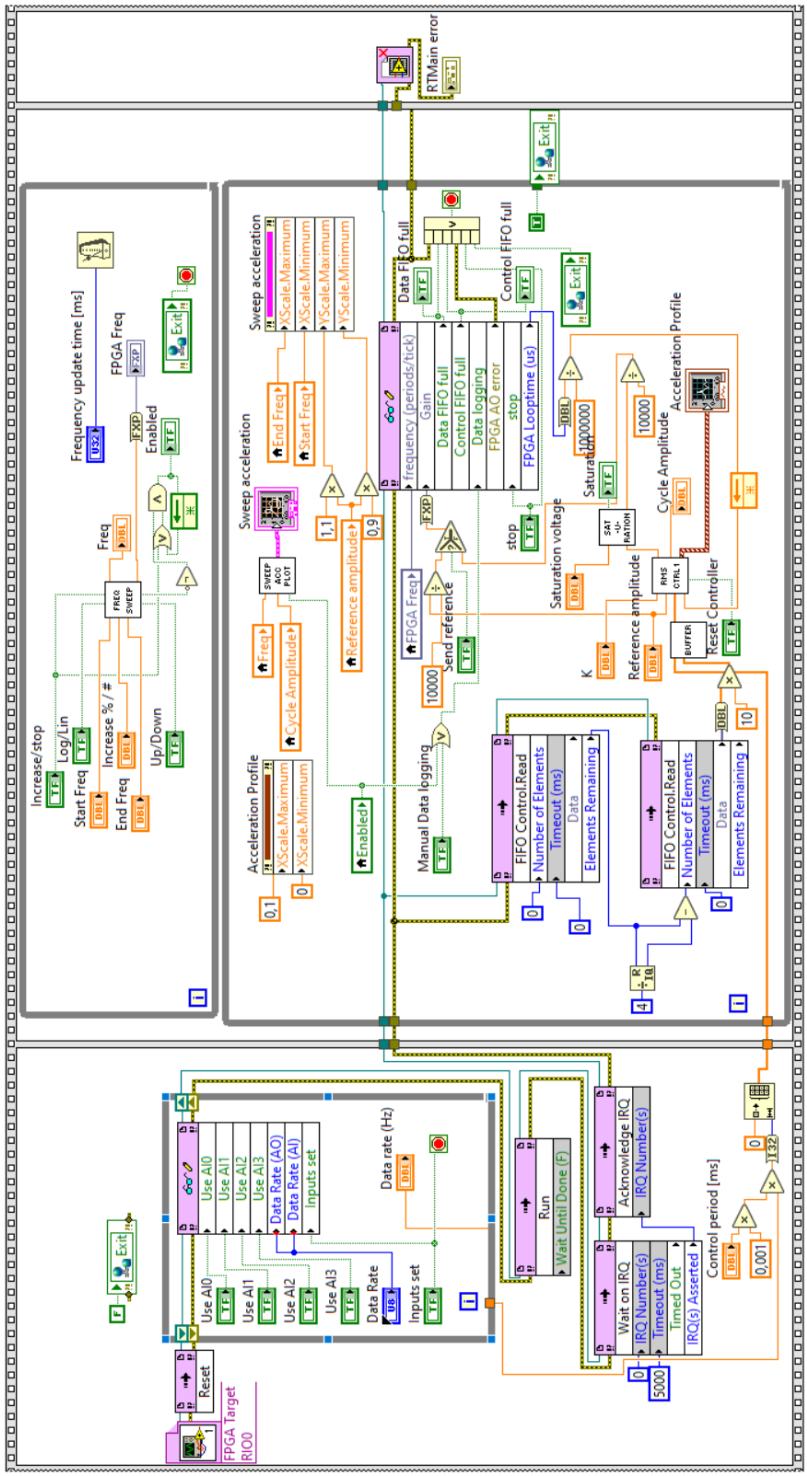

FIGURE C.6: **Frequency sweep controller; controller block diagram**

C.1.2 User guide

Below, a step by step instruction is described. This can be used as a guideline to operate the designed Frequency sweep controller.

1. Make sure that all the analogue input modules are connected into the right slot, the cRIO is connected to the (Lab)laptop by USB cable and the correct LabVIEW (NI LabVIEW 2019 sp1 (32-bit)) software is installed.

2. **Open: RMS_sweep.lvproj**
   The project explorer window should look like Figure C.3. In this project three virtual interfaces (VI) are included.

3. When you are not 100% sure whether this project was the last one deployed on the cRIO, the FPGA needs to be recompiled. **Right click Sweep_FPGA build specification and select Rebuild**.

   (a) *When the "bitfiles already match" popup window appears, select rebuild anyway. Use the local compile server to rebuid the FPGA bitfiles.*

   (b) *The compilation of the Sweep_FPGA.vi on the FPGA of the cRIO should take about 10 to 15 minutes. Time for some coffee with chewy cookies!*

4. **Open** using the project explorer window **Sweep_Controls.vi** and **Sweep_Host.vi**

5. **Fill in** the desired hardware settings on the **Sweep_Controls.vi** front panel and fill in the desired Filename on the **Sweep_Host.vi** front panel.

6. **Run Sweep_Controls.vi** by clicking the white arrow in the top left corner of the screen.

7. **Run Sweep_Host.vi** by clicking the white arrow in the top left corner of the screen.

8. Check your hardware settings in **Sweep_Controls.vi** again, if everything is correct, **press OK** in the hardware settings

9. Fill in the desired sweep and controller settings.

   (a) *'Freq' and 'Cycle amplitude' are indicators which indicate the frequency and cycle amplitude during the sweep*

   (b) *The upsweep goes from 'Start freq' to 'End freq' and the downsweep goes from 'End freq' to 'Start freq'.*

(c) *Log/Lin: True: perform a logarithmic sweep. False: perform a linear sweep*

(d) *Up/Down: True: perform an upsweep. False: perform a downsweep*

(e) *A lower value for the controller compress factor 'K' will make the response faster, but chances of overshoot arise. A value of 'K' in the range from 50 to 100 should in general be fine.*

10. **Click Increase/Stop** to start the frequency sweep

    (a) *Data will be stored automatically on the given filename, up until the sweep has ended.*

    (b) *The sweep automatically stops when the final frequency is reached*

    (c) *Clicking Increase/Stop again will abort the sweep and return to the initial frequency.*

11. **Click STOP** in the Hardware settings on Sweep_Controls.vi to abort both Sweep_Controls.vi and Sweep_Host.vi

C.1.3 Performance

The Frequency sweep controller performance has been measured using a logarithmic frequency sweep from 20 to 150 Hz on the shaker. The reference value was set at $0.5g$ acceleration using an increase percentage of 0.1% *per* $200ms$. Figure C.7 shows the acceleration profile, measured acceleration amplitude and the absolute error percentage over time.
In the acceleration amplitude, some oscillations in acceleration amplitude can be noticed. This can be the result of the increased absolute step size due the logarithmic sweep. Decreasing the stepsize could solve this. During the sweep the error with respect to the $0.5g$ acceleration reference did not exceed 2.55%.

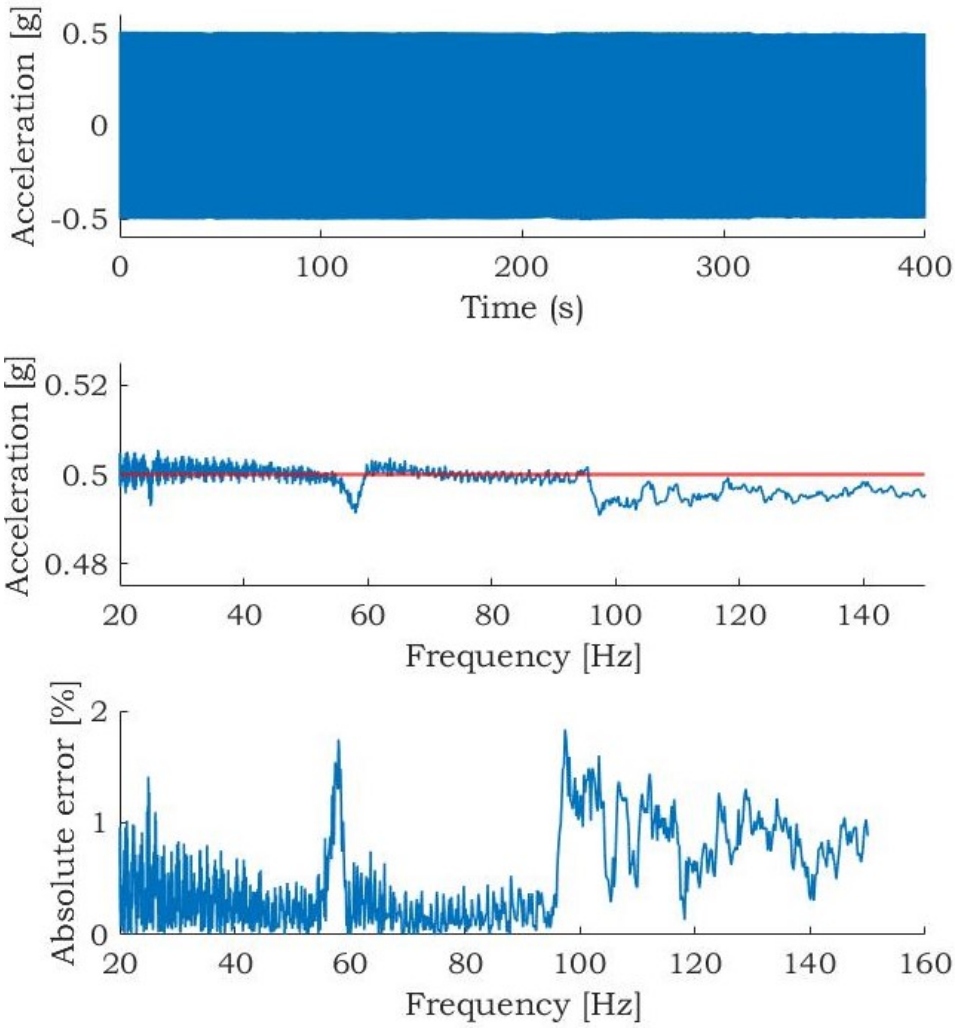

FIGURE C.7: **Frequency sweep controller; empty shaker performance experiment**

C.2 Power spectrum controller; FFT based feedback

The power spectrum controller generates a random signal with a predefined power spectrum. This could be, a white or colored noise signal for instance. In theory, white noise has an equal power distribution over the entire frequency range. On the contrary, colored noise has an unequal power distribution over frequency, which is also the case in real world vibrations, Appendix D. The user can load a power spectrum belonging to a real world vibration, successively the controller will generate a random acceleration signal with the same power spectrum on the shaker.

Using the fast Fourier transform (FFT), quick calculations of a signal's power spectrum can be made [9]. This enables to implement a control loop based on the spectral data of the acceleration. Similar to the frequency sweep controller, the power spectrum controller is based on a feedback control structure. The feedback signal contains the power spectrum data of the current acceleration signal. The error is obtained by taking the current power spectrum over the reference power spectrum. Successively, the error is fed to the controller which alters the new actuation power spectrum following equation (C.2).

$$D_{i+1} = D_i \left(\frac{A}{R}\right)^k \tag{C.2}$$

where:

D_{i+1} = New actuation power spectrum
D_i = Current actuation power spectrum
A = Current power spectrum
R = Reference power spectrum
K = Discount factor (Proportional gain)

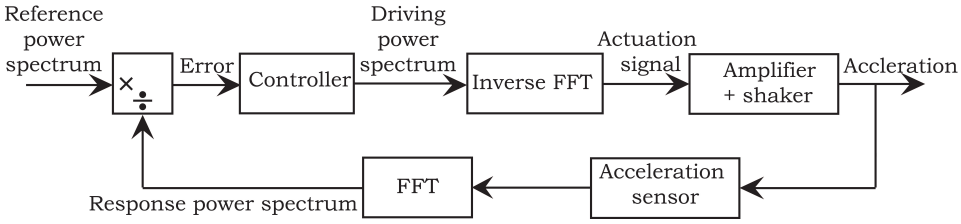

FIGURE C.8: **Random signal controller block scheme.**

The new actuation power spectrum D_{i+1} is back-converted into a time domain actuation signal by an inverse fast Fourier transform. This actuation signal is used to drive the shaker. New acceleration data is measured on top of the shaker using an accelerometer and fed back to the controller. Figure C.8 depicts the block scheme representing the random signal controller.

C.2.1 LabVIEW design

To implement the controller on the experimental setup, the cRIO is programmed using LabVIEW. The LabVIEW project on the random signal controller is build as a three level virtual interface structure, Figure C.9.

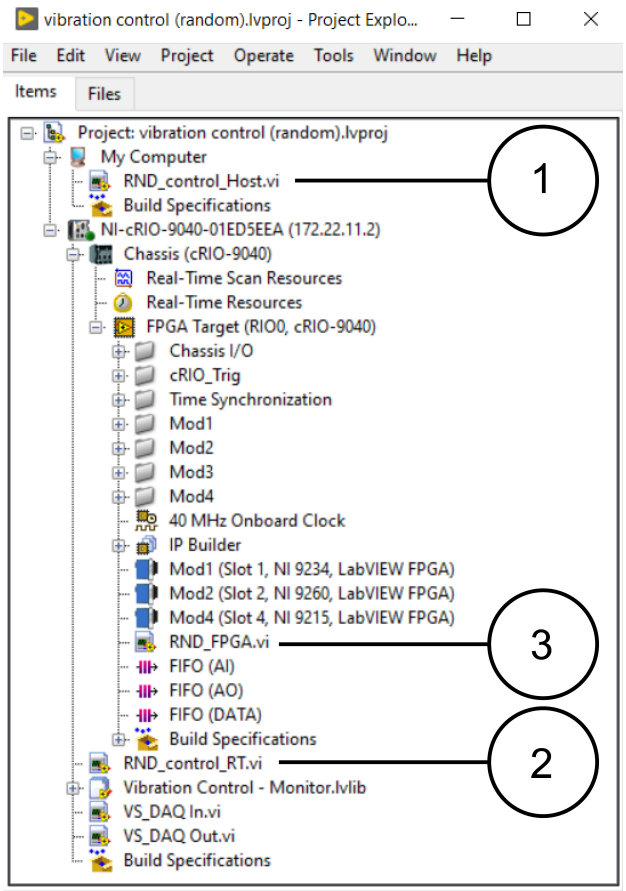

FIGURE C.9: **Random signal controller; Labview project explorer interface**

The first virtual interface, *RND_Control_Host.vi*, runs on the hosting computer or laptop. This virtual interface is used to load the reference spectrum from a data file, store measurement data and set all the controller settings on the front panel, Figure C.10. The front panel consists of two tabs. The first tab is used to load the reference spectrum and set the hardware settings. The second tab is used to alter the discount factor (K) and monitor the measured acceleration spectrum. Table C.2 shows a brief description of the in and output parameters of the *RND_Control_Host.vi*.

The second virtual interface, *RND_Control_RT.vi*, runs on the real time module of the cRIO. This virtual interface receives the controller settings from the *RND_Control_Host.vi* and runs the control part of the feedback loop, Figure C.12. The blockdiagram belonging to the *RND_Control_RT.vi*, consists of a five stage sequence. All the controller settings are reset in the first frame. The second frame establishes the data connection with the *RND_FPGA.vi* and loads the preset controller settings form the *RND_Control_Host.vi*. The third frame sends the reference actuation signal to the shaker in order to determine the initial power spectrum. The fourth frame executes the control loop and keeps running during the experiment. The controller receives acceleration data in the "*Reading DAQ block*" from the *RND_FPGA.vi*. Time domain acceleration data transforms from time to frequency domain in the "*PS block*". The "*EQU block*" generates a new actuation spectrum signal according to equation (C.2). This "*Driving PS*" is transferred to a second while loop, where the spectrum is converted into a time domain signal and send to the *RND_FPGA.vi*. When the user aborts the control loop, the blockdiagram moves to the fifth frame. Where, the data connection with *RND_FPGA.vi* is aborted.

The third virtual interface, *RND_FPGA.vi*, runs on the FPGA of the cRIO. This virtual interface forms the connection between the real world, the real time controller and the hosting PC. The actuation signal comes from *RND_control_RT.vi* and is send by the NI-9260 analog output module to the amplifier and shaker. The real world data is read by the NI-9234 analog input module and transferred to the *RND_control_RT.vi* for the control loop, and to *RND_control_Host.vi* for monitoring and data storage for further analysis.

Table C.2 gives a brief description of all the in- and output values of the Power spectrum controller. These in- and outputs can be entered or monitored in the *RND_Control_Host.vi* front panel, which is depicted in Figure C.10.

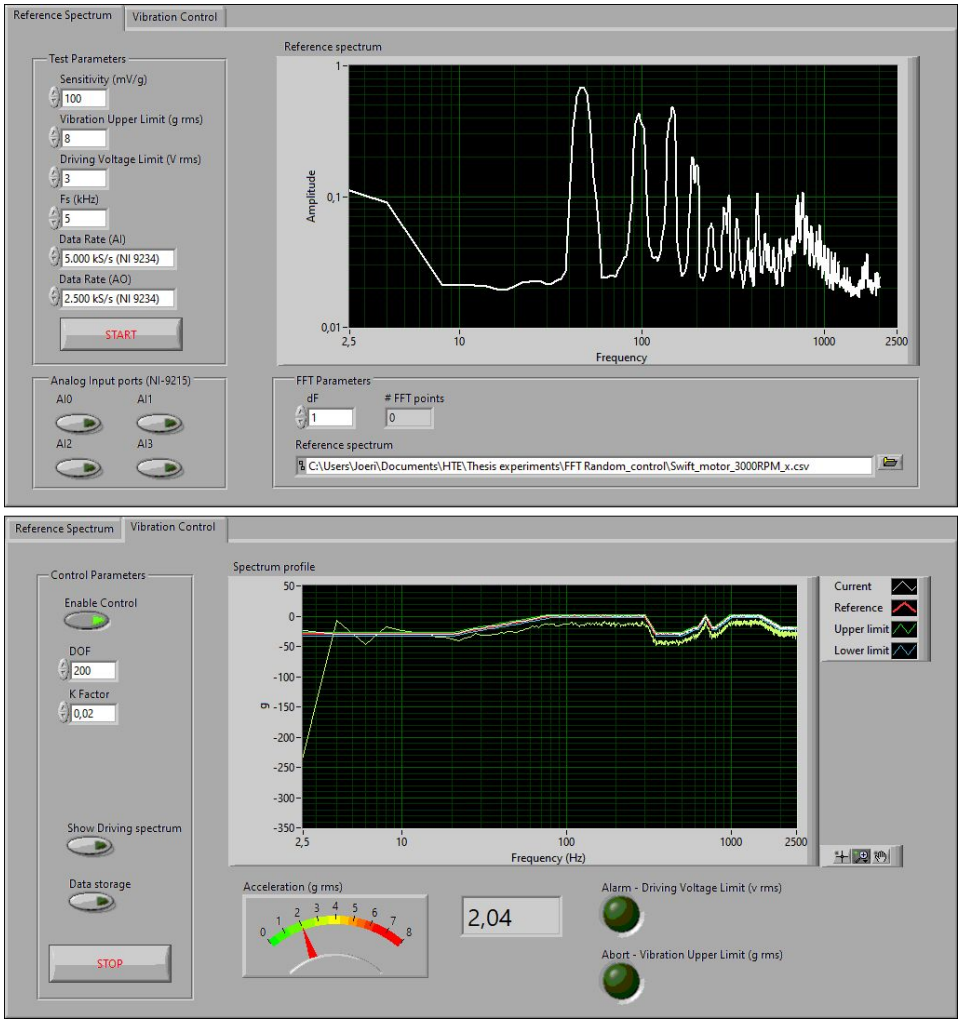

FIGURE C.10: **Random signal controller; *RND_Control_Host.vi* front panel tab 1 and 2. This interface is used to load the data into the controller, enter the control settings and monitor the performance during the experiment.**

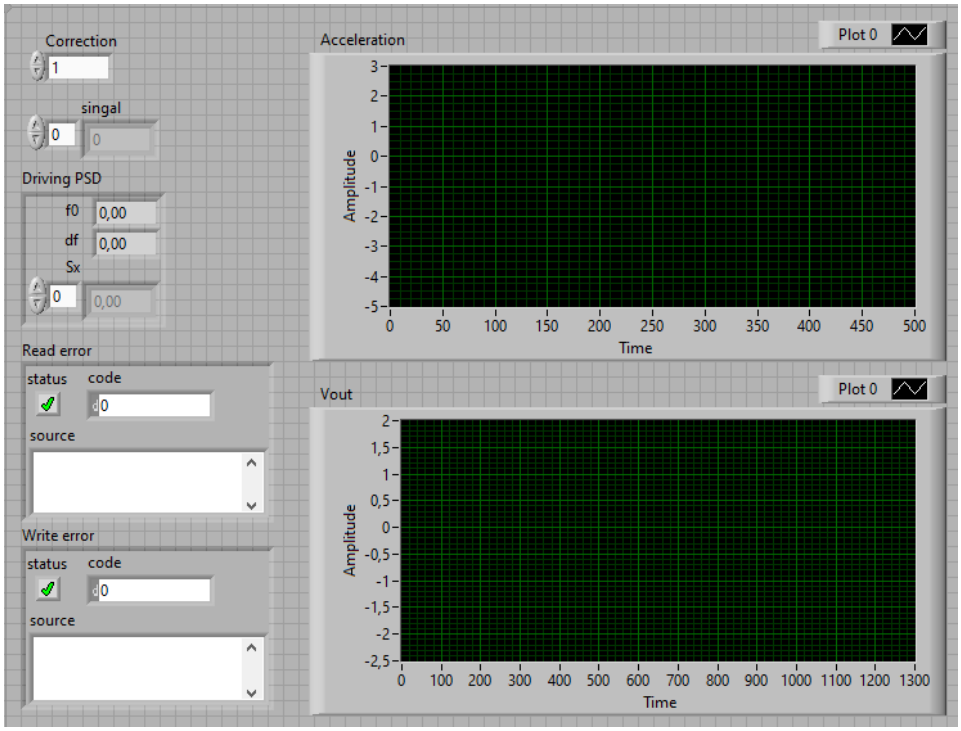

FIGURE C.11: **Random signal controller; Real time controller front panel**

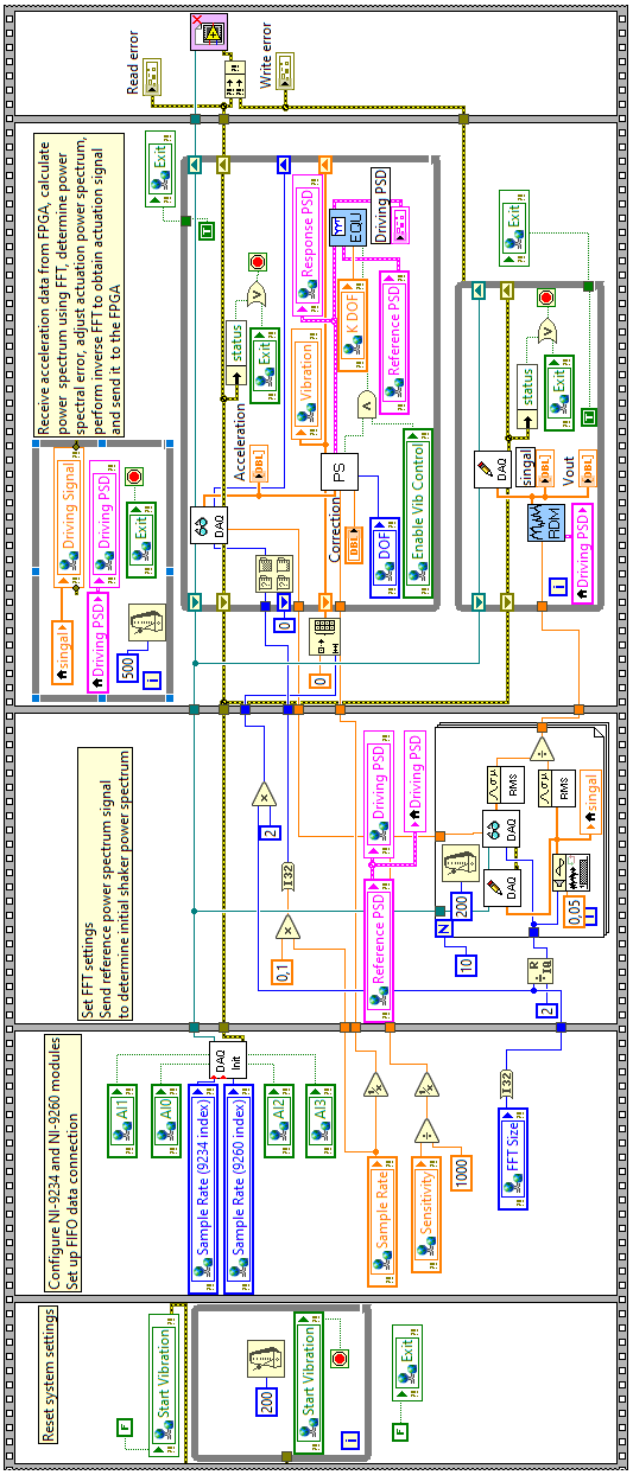

FIGURE C.12: **Random signal controller; block diagram. A five stage sequential frame is used to build all the functionalities in the controller.**

TABLE C.2: **Input and output description of the *RND_Control_Host.vi* front panel**

Input / Output	Description
Reference spectrum	
Sensitivity (mV/g)	Accelerometer sensitivity (mV/g)
Vibration Upper Limit (g rms)	Maximum RMS acceleration value produced by the shaker (gravity rms)
Driving Voltage Limit (V rms)	Maximum RMS output voltage send by the NI-9234 AO module
Fs (kHz)	Sample frequency of the analog input (to set FFT size)
Data Rate (AI)	Sample frequency of the analog input (to set module)
Data Rate (AO)	Sample frequency of the analog output (to set module) This should be 0.5*Data Rate (AI) for correct data flow
Start	Toggle button, all settings in the first tab are set, start vibration
AI0	Enable Analog input 0 to measure more sensor data
AI1	Enable Analog input 1 to measure more sensor data
AI2	Enable Analog input 2 to measure more sensor data
AI3	Enable Analog input 3 to measure more sensor data
dF	Frequency step size in the reference FFT [Hz]
Reference spectrum	File path to data file containing the reference spectrum
# FFT points	Indicator showing the number points in reference FFT This should be equal to the Data Rate (AO)
Reference spectrum	Plot showing the current loaded reference spectrum
Vibration Control	
Enable Control	Enable the controller to alter the driving spectrum
DOF	Number of spectrum profiles to determine the response spectrum
K Factor	Discount factor of the controller
Show driving spectrum	Show the driving spectrum in the spectrum profile plot
Data storage	Switch button to enable data storage in a file
Stop	Toggle button to abort the controller script and turn the controller off
Acceleration (g rms)	Indicator showing the system's rms acceleration
Spectrum profile	Plot showing the reference and response spectrum
Driving Voltage Limit	Indicator showing surpass of the AO rms voltage limit This is only an alarming indicator
Vibration Upper Limit	Indicator showing surpass of the rms acceleration limit Aborts the script and turns the controller output off

C.2.2 Performance

The random signal controller performance has been evaluated by reproducing a reference spectrum of a real world signal. The real world signal was measured, over a 15 seconds time interval, on top of a Suzuki swift engine running at 3000 RPM. Successively, the fast Fourier transform of the reference signal was made and loaded into the control script. The goal of the random signal controller is to generate a random signal with the same spectral profile as the real world signal. In Figure C.13 the time response of the real world vibration and the shaker vibration are plotted together with the spectral profiles of both vibrations.

Looking at Figure C.13, some clear difference between the real world and shaker accelerations can be noticed in the time domain. The real world signal seems to be more constant over time than the shaker acceleration signal. On the other hand, the spectral profiles seem to match quite well. Therefore could be said, that the average acceleration amplitude per frequency of both vibrations is similar over the total time interval.

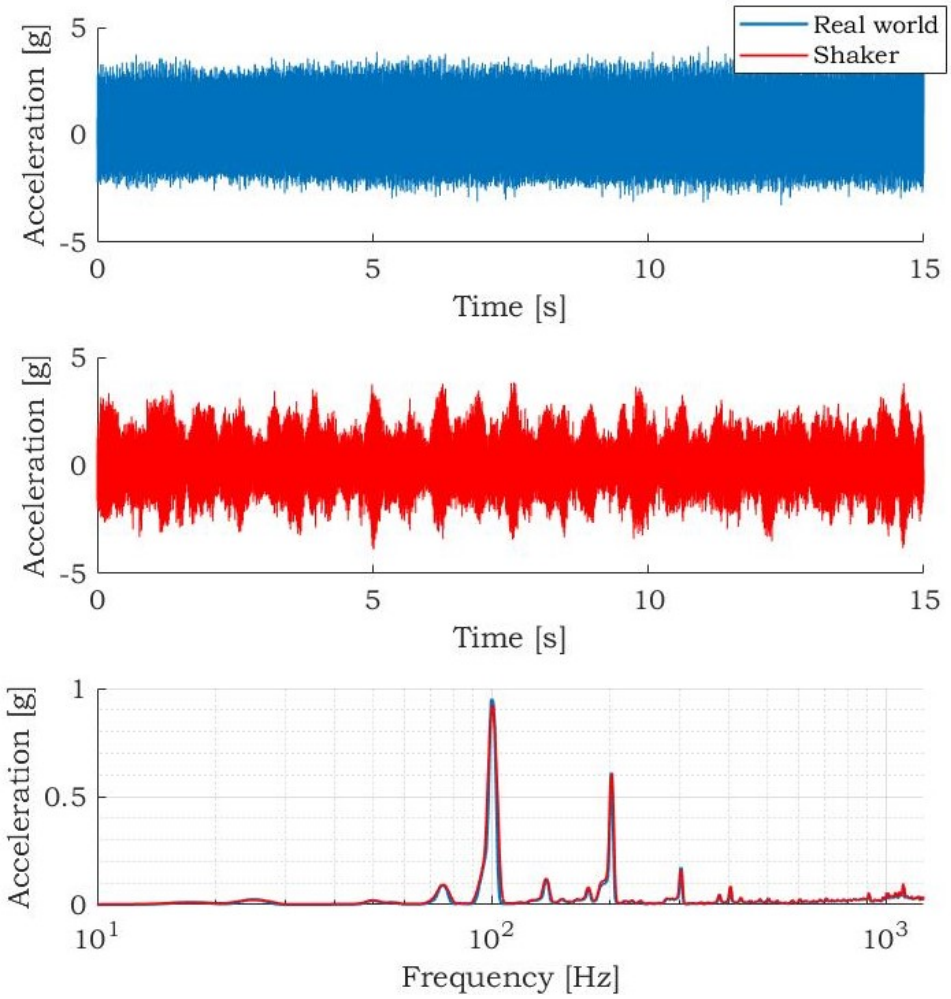

FIGURE C.13: **Random signal controller; empty shaker vibration compared with a real world vibration coming from a Suzuki Swift engine running at 3000 RPM**

C.3 Time Waveform Replication; Feedforward control

The Time Waveform replication controller is used, as the name says, to reproduce a measured acceleration signal. The acceleration data can be loaded onto the controller. successively, before the actuation signal is send to the shaker, the controller alters the waveform using feed forward to obtain the correct acceleration on the shaker.

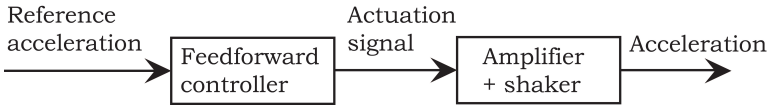

FIGURE C.14: **Time Waveform Replication controller block scheme**

In order to construct the feed forward controller, the dynamics of the electrodynamic vibration shaker need to be known. These can be obtained by performing a dynamic identification as described in Appendix B. Two resonant modes can be found in the shaker identification, namely the suspension mode and the coil mode. Because, the controller will predominately be used in a frequency range from ten to several hundred or one thousand hertz, it is only required to compensate for the suspension-mode. The use of a low-pass filter in the controller will reduce the higher frequency accelerations of the acceleration signal and attenuate the coil mode.

The feedforward control transfer function could be constructed by taking the inverse of the suspension mode transfer function, equation (B.26). However, the shaker presents no DC response, which means that the double integrator in the inverse transfer function will make the driving signal go to infinity when the frequency approaches zero hertz. The output voltage of the analog output module placed in the cRIO will saturate. By replacing the poles at $s = 0$ for $s = -1/\mu$, where μ is a positive design parameter, the large DC amplification can be prevented [15]. This results in the following transfer function to compensate for the suspension mode.

$$H_{FF}(s) = \frac{(m_a + m_l)s^2 + c_t s + k_t}{\Gamma(\mu s + 1)^2} \tag{C.3}$$

The controller is programmed on the cRIO, which is a digital system. Therefore, the transfer function needs to be converted from continuous to discrete time. The easiest way to do this, is by using the Matlab function "c2d". Here, the continuous transfer function, sample time and conversion method can be specified to convert to discrete time. Each time the system dynamics change; for instance by changing

the amplifier gain or mounting something different on the shaker, the system identification and controller design needs to be redone. When the acceleration signal is set at a different sample frequency, the discrete transfer function needs to be re-determined.

C.3.1 LabVIEW design

To implement the controller on the experimental setup, the cRIO has to be programmed using LabVIEW. The LabVIEW project on the *Time wave replication; feedforward controller* is build as a three level virtual interface structure. Figure C.15 shows the project window, containing the three virtual interfaces included in the project.

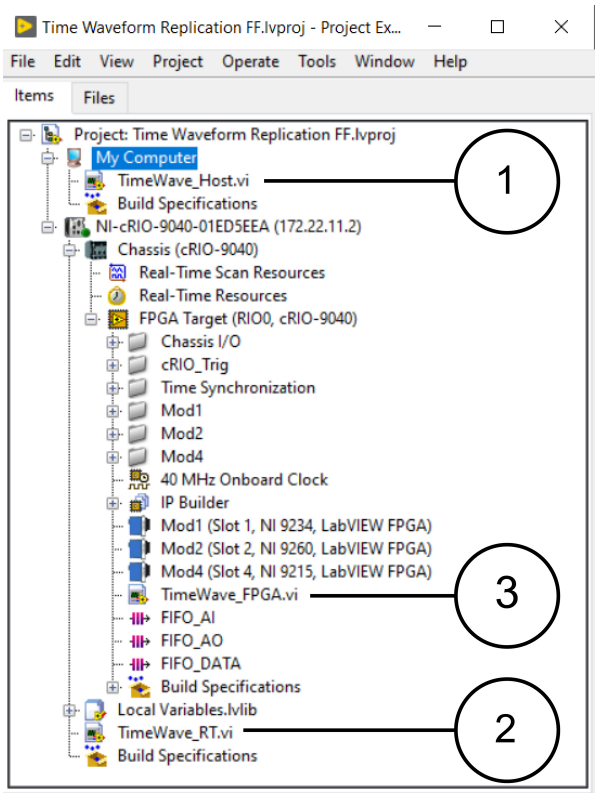

FIGURE C.15: **Time waveform replication; Labview project explorer interface with the three virtual interfaces used to run the controller highlighted.**

The first virtual interface *TimeWave_Host.vi* runs on the computer. This interface is used to load the reference acceleration signal and store the measurement data generated during the experiment. In the front panel the reference file path and

the analog input settings can be entered, Figure C.16.

The second virtual interface, *TimeWave_RT.vi*, runs on the real time module of the compactRIO. This interface is used to set the analog input rates of the modules, enable the feedforward control and enter the discrete transfer function, Figure C.17.

The third virtual interface, *TimeWave_FPGA.vi*, performs the feedforward control part using the discrete transfer function and forms the connection between the digital and real world. The reference acceleration signal comes from the *Timewave_RT.vi* and is send via the discrete transferfunction to the NI-9260 analog output module. Successively, the real world data is read by the NI-9234 analog input module and send to the *Timewave_Host.vi* for monitoring and data storage for further analysis.

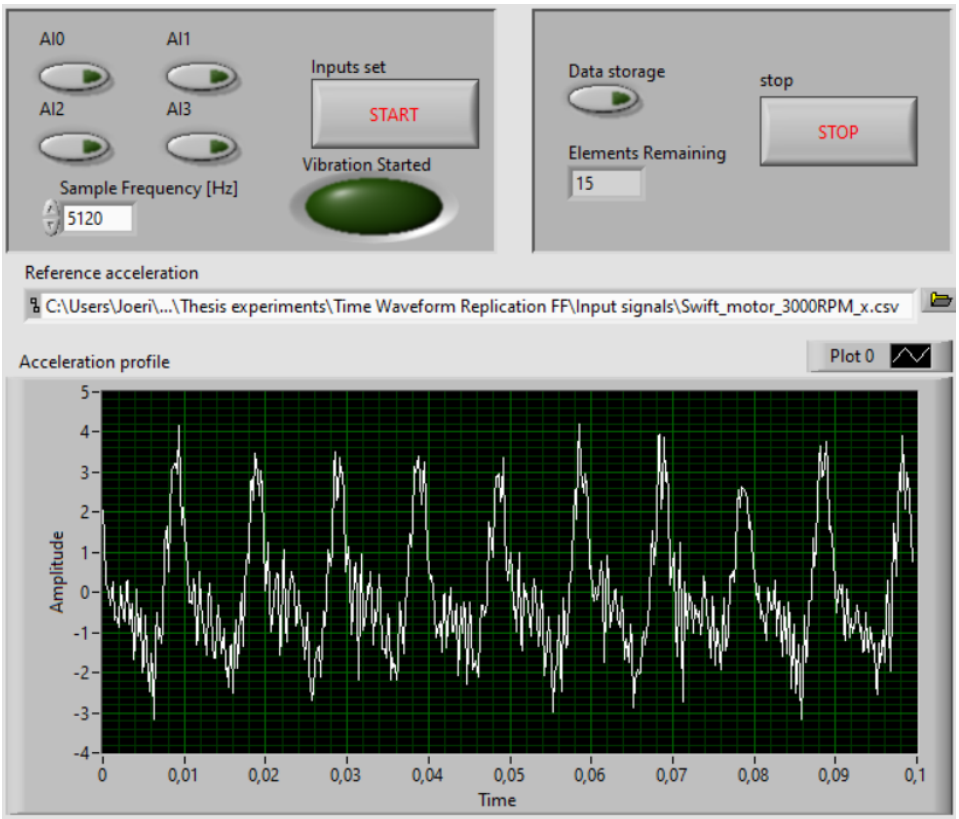

FIGURE C.16: **Time waveform replication; frontpanel *TimeWave_Host.vi***

A brief description of the in- and output parameters of the controls in the *TimeWave_Host.vi* and *TimeWave_RT.vi* virtual interface front panels, Figures C.16 and C.17 respectively, is found in table C.3.

TABLE C.3: **Input and output description of the *Timewave_Host.vi* and *Timewave_RT.vi* front panels**

Input/Output	Description
Timewave_Host.vi	
AI0	Enable Analog input 0 to measure sensor data
AI1	Enable Analog input 1 to measure sensor data
AI2	Enable Analog input 2 to measure sensor data
AI3	Enable Analog input 3 to measure sensor data
Sample Frequency [Hz]	Sample frequency of the analog in- and output modules
Inputs set	Toggle button; all settings are set and start the vibration
Vibration Started	Indicator; the timewave replication is running
Data storage	Enable data storage in measurement file
Stop	Stop the measurement
Elements Remaining	Indicator; amount of elements in the FIFO
Reference acceleration	File path to the reference timewave to replicate
Acceleration profile	Graph showing the current acceleration profile produced on the shaker
TimeWave_RT.vi	
Data Rate AO	Sample frequency of the analog output
Data Rate AI	Sample frequency of the analog input
Enable FF	Enable the feedforward transfer function
Reset FF	Reset the feedforward transfer function
FF FXP	Fixed point multiplication to increase or decrease amplitude for the transfer function
Correction Factor	Factor to correct feedforward amplitude offset
FXP Feedforward TF	Indicator showing the fixed point transferfucntion which can be entered in the math script module in the block diagram
Write Error	Indicator showing the real time module errors
Empty elements remaining	Indicator showing the empty elements remaining in the FIFO form the RT to the FPGA.
Reference acceleration profile	Graph showing the reference acceleration profile to be excited by the shaker

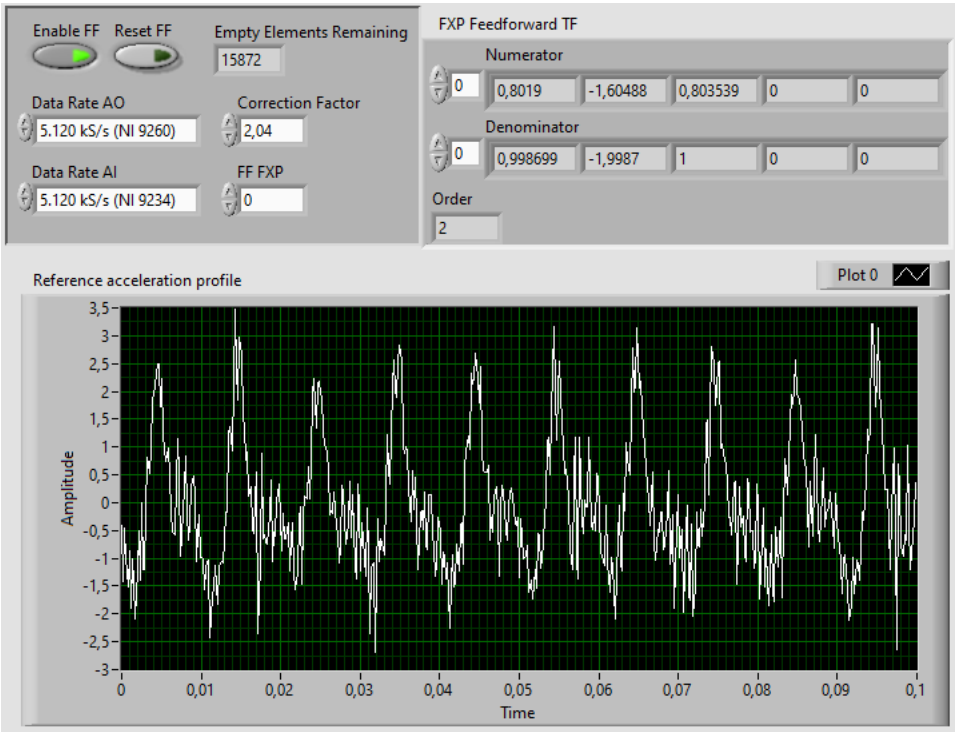

FIGURE C.17: **Time waveform replication; frontpanel *TimeWave_RT.vi***

C.3.2 Performance

The time waveform replication controller performance has been evaluated by reproducing the same acceleration signal as used for the random controller; a 15 seconds acceleration signal measured on top of a Suzuki swift engine running at 3000 RPM. One component of the three directional acceleration data was chosen to reproduce.
The goal of the time waveform replication controller is to reproduce the measured acceleration signal. Therefore, an evaluation will be made based on the shape of the time signal and the Fourier transform, Figure C.18.

Looking at the overall time signal, it can be seen that the response of the shaker looks very similar to the real world signal and the Fourier transform of both signals seems also be the same. When zoomed in on a very small time interval, of roughly 50 milliseconds, some minor differences in the response can be found. When the two acceleration signals are placed on top of each other, a RMS error of $0.14g$ was found. The total acceleration signal has a RMS of $1.12g$.

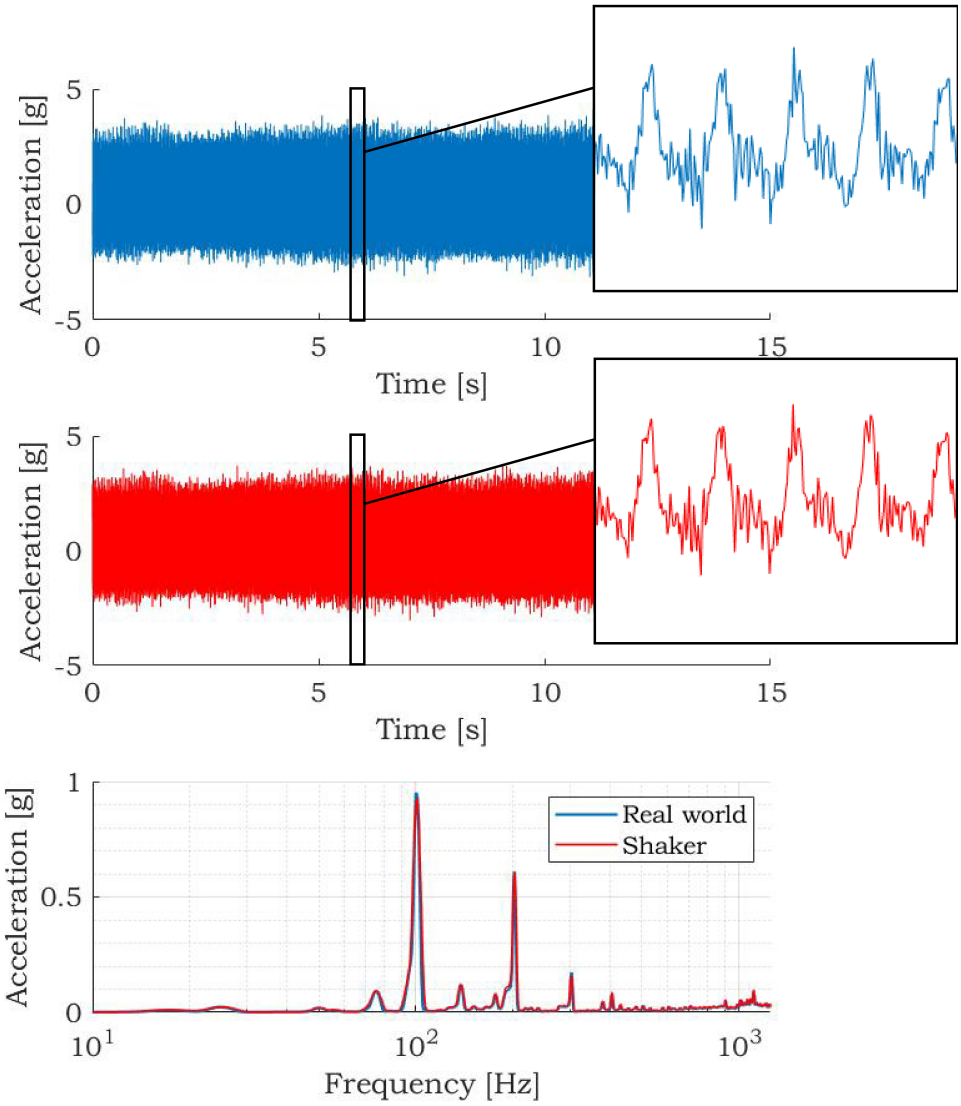

FIGURE C.18: **Time Waveform Replication controller; reference acceleration signal measured on a Suzuki Swift engine running at 3000 RPM. On top the reference signal together with a 50 milliseconds zoom on the right. In the middle, the replicated signal, measured on the shaker. And below the fast Fourier transform of both acceleration signals on top of each other.**

D

Car vibration experiments

During the graduation project lot of different vibrations have been measured and generated. Some characteristics, like amplitude and the presence of significant peaks, can be seen in the raw acceleration data. However, to obtain more information on the frequency content contained in the vibration, an analysis would be required. This appendix presents an overview of the real world vibration measurement setup and the analysis used for the acceleration data.

D.1 Real world vibration measurement setup

In order to perform real world vibration measurements, it is desired to have a portable measurement setup. This was obtained by using a laptop in combination with a NI-cDAQ 9171. The cDAQ is powered from the laptop by USB, which is also used for data transfer. The three directional PCB accelerometer was connected to the first three terminals of the NI-9234. The fourth terminal of the NI-9234 was used to measure the voltage generated by the vibration energy harvester simultaneously over a 30Ω resistance. Figure D.1. During the measurements, the acceleration and generated voltage are sampled with a 5120Hz sample frequency. This was in accordance with the sample frequencies used during the lab experiments and sufficiently high to sample most real world vibrations, which a typically below 100Hz [37].

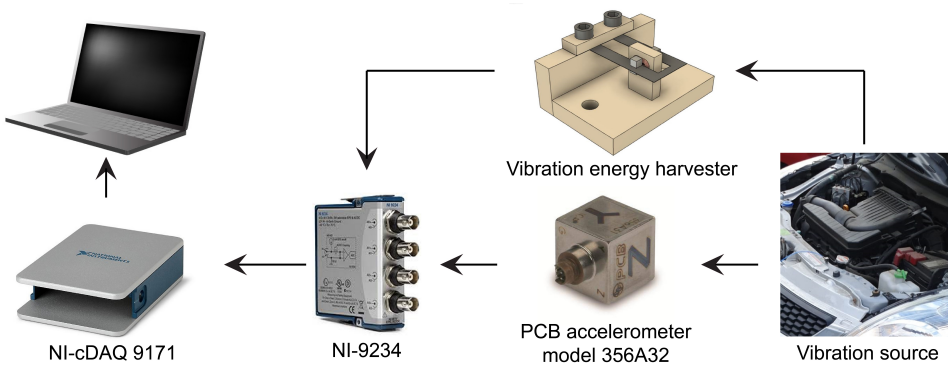

FIGURE D.1: **Schematic representation of the portable measurement system where the three directional acceleration and the vibration energy harvester generated voltage are measured simultaneously by the NI-9234 in a cDAQ chassis.**

D.2 Car engines as source of vibration

The real world experiments were performed on the engine suspensions of two cars, a 2011 Suzuki Swift and a 2010 Volvo V50. The fist car contained a 1.2L gasoline engine and the second had a 2.0L diesel engine. In both cases was the vibration energy harvester mounted to the engine side of the engine suspension. This location was chosen for the significant presence of vibrations from the engine and the possibility to connect the vibration energy harvester rigidly to a towering bolt of the suspension.

During the experiments was the engine RPM kept at a constant level. Due to this it was possible to approach the resonance frequency of the vibration energy harvester. This way was ensured, that sufficient power was generated to measure and compare with the three lab experiments. From the three directional acceleration data, only the Y direction was used for analysis, because this direction corresponds to the vibration energy harvester input direction.

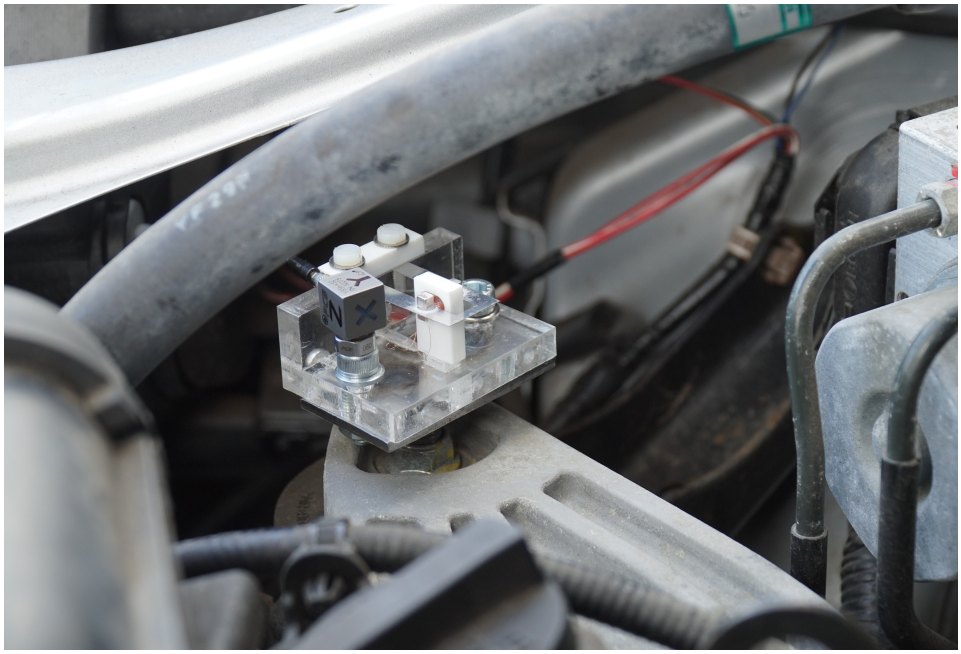

FIGURE D.2: **The constructed vibration energy harvester mounted on top of a towering bolt from the engine suspension of the Suzuki swift. On top of the vibration energy harvester is the PCB accelerometer mounted with the use of a magnet.**

D.3 Measured acceleration data; raw

Figure D.3 shows the raw Y direction acceleration data over a 15 seconds time interval with in the small frame a 50 milliseconds zoom of the vibration signals. The first notable difference is the peak-peak amplitude of the various signals. The Suzuki acceleration data is plotted on a 5g interval, figure D.3a, while the Volvo acceleration data, figure D.3b, has a 25g interval, where $(1g = 9.81m/s^2)$.

By looking at the 50 milliseconds zoomed interval, in both signals can a oscillating wave can be recognized with lots of higher frequency oscillations over it. The major difference is the behavior of the higher frequency oscillations, the Suzuki has more constant amplitude for the higher frequencies. The Volvo signal is characterized by some dominant repetitive peaks. The differences in high frequency behavior could be clarified by the two different engine types. The Volvo has a diesel engine, which relies on the spontaneous combustion principle. The air in the cylinder is compressed and some fuel is injected. The air has been heated a lot due to the compression, which makes the fuel ignite spontaneously. This give a much more intense reaction than the gasoline engine, where the fuel ignites with a spark plug.

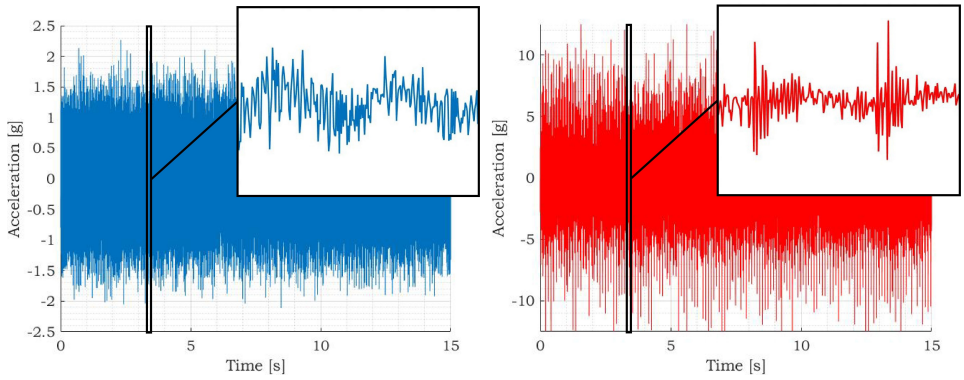

(A) (B)

FIGURE D.3: **Raw acceleration data of the Suzuki Swift running at 1320 RPM (A) and Volvo V50 running at 1140 RPM (B). Measured on the base of the vibration energy harvester, which was mounted on the engine suspension of the cars.**

Figure D.4 shows the one directional acceleration data of the Suzuki Swift running at various engine RPM. Analyzing the acceleration data, it can be seen that the low frequency oscillation increases in frequency and amplitude with an increasing RPM. Also the high frequency content seems to increase in amplitude, but it is hard to see whether the frequency also increases.

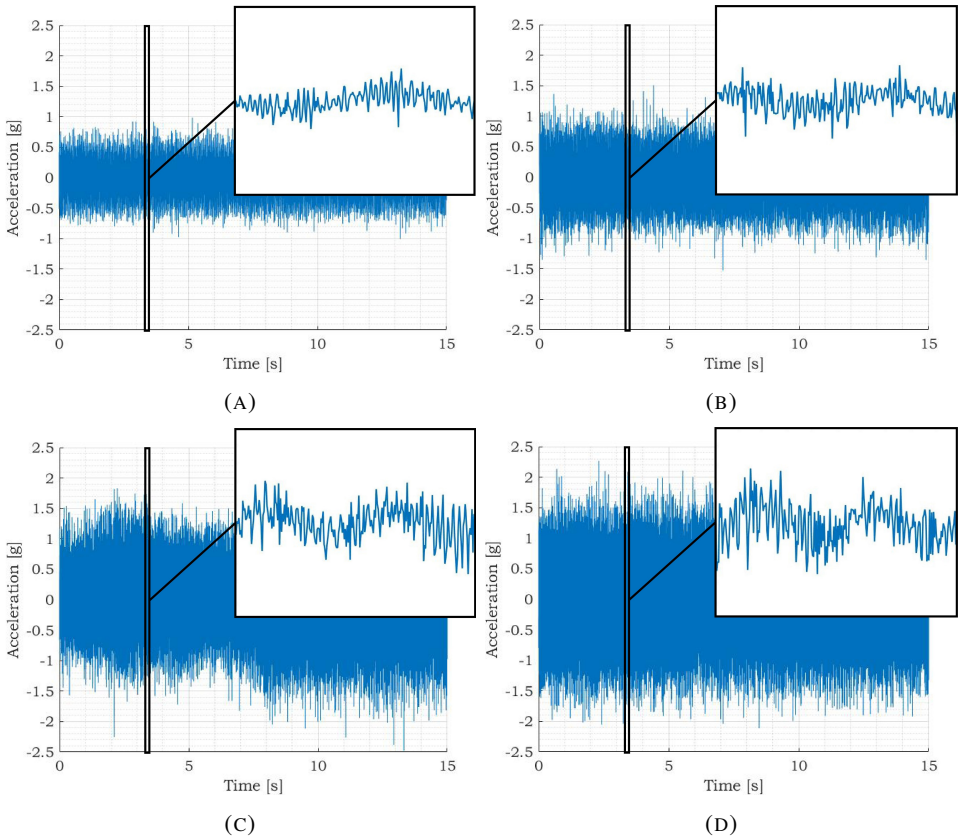

FIGURE D.4: **Raw acceleration data measured at the engine suspension of the Suzuki Swift, while the engine was running at 750 RPM (A), 900 RPM (B), 1230 RPM (C) and 1320 RPM (D).**

D.4 Measured acceleration data; analysis

One of the most well known methods to obtain more information about the content of a vibration is the fast Fourier transform (FFT). The fast Fourier transform is an algorithm to efficiently calculate the discrete Fourier transform of a discrete time signal. With the FFT, a time domain signal is converted into a representation in the frequency domain. The basic output of the FFT is a vector of complex numbers, where each value represents the phase and amplitude of the frequency content. Usually, only the amplitude per frequency is of interest, which is the absolute value of the complex numbers.
When the FFT is taken over a longer time interval signal, the obtained frequency resolution increases. However, the frequency variations over time become invisible. Therefore, it could also be chosen to take multiple short FFT's of shorter (overlapping) time intervals, resulting in something known as a spectrogram or waterfall diagram. On the one hand this reduces the frequency resolution obtained per FFT, but on the other hand the frequency content changes over time can be noted. Therefore, in the fast Fourier transform vibration analysis, always a trade off between frequency and time resolution has to be made. In general can be said that the obtained frequency resolution in Hertz is one over the time period of the FFT in seconds.

The spectrogram plot in figure D.5 shows the frequency content over time of the raw acceleration data shown in figure D.3a. Based on the vibration analysis as presented in chapter 2, it can be concluded that the vibration contains predominately dominant frequencies. Therefore, the presentation of a 2D FFT plot could give a better overview.
Figure D.6 shows the FFT plot obtained from the acceleration data form figure D.3a. The FFT plot was made by taking the average value of all the FFT plots used for the spectrogram, this resulted in an averaged FFT with a frequency resolution of 1 Hz. In the FFT plot can clearly be seen that the vibration has a dominant frequency peak at 44 Hz with an amplitude of 0.37 g.

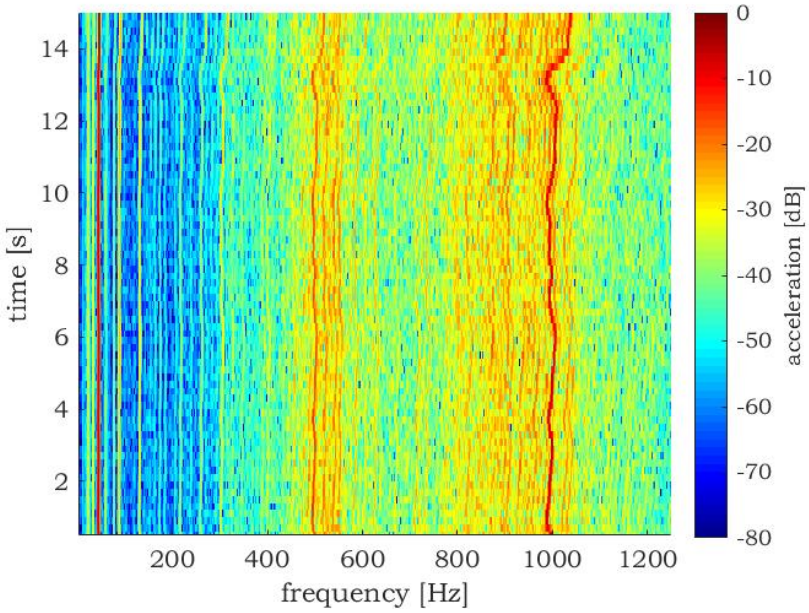

FIGURE D.5: **Spectrogram of the acceleration data measured on the Suzuki Swift running at 1320 RPM. The spectrogram has been constructed out of 1 second time interval FFTs with 80% overlap between the successive time intervals.**

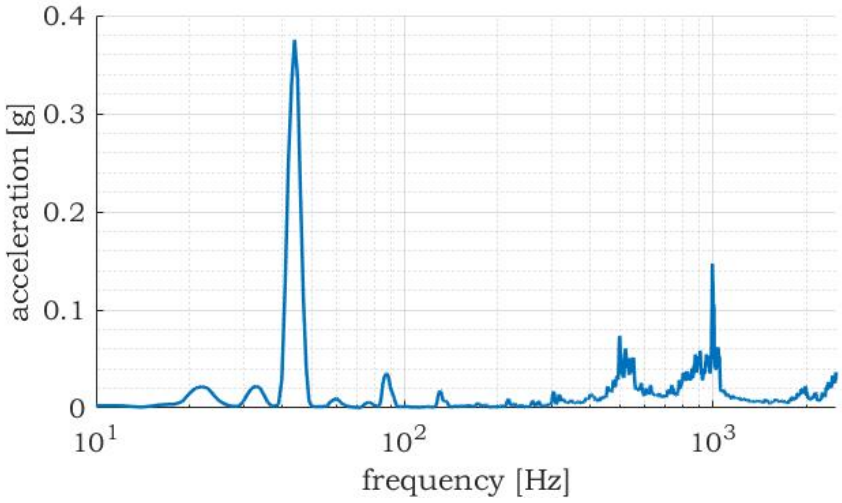

FIGURE D.6: **FFT plot of the acceleration data measured on the Suzuki Swift running at 1320 RPM. The FFT plot has been constructed by taking the average of all the 1 sec FFTs used in the spectrogram shown in figure D.5.**

Figure D.7 shows in one overview the different FFTs belonging to acceleration data plotted in figure D.4 where per measurement the engine RPM was varied. It can clearly be seen that the most dominant frequency peak shifts with the engine RPM. The height and width of the dominant frequency peaks varies also a bit. This can be the result of an increasing vibration amplitude and being more (in)consistent with the engine RPM during the measurement. The higher frequency content around 500 Hz and 1000 Hz does not shift significantly, which is most likely an eigenfrequency of the chassis on which the harvester was mounted.

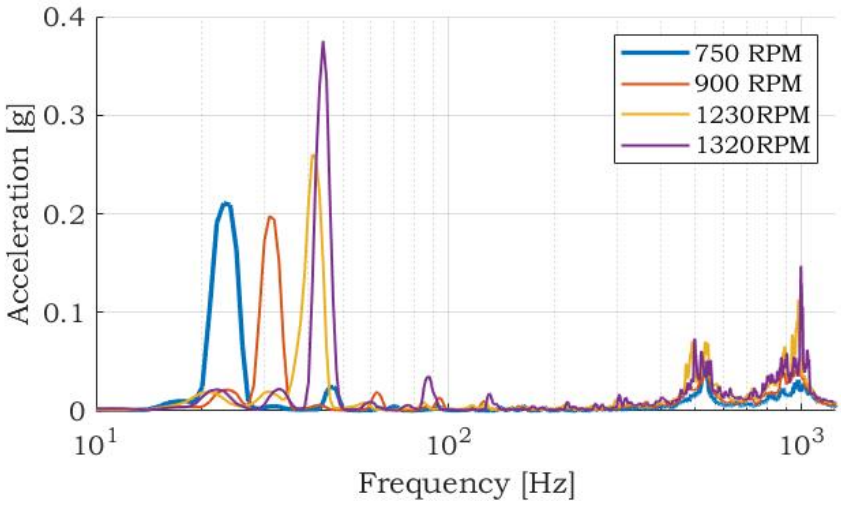

FIGURE D.7

E

Harvester design

E

When all the controllers were operational, the real thesis experiments could begin. In order to perform a comparative study between the various experiments, an energy harvester needs to be constructed. It was desired to be an easy design and easy to implement on the shaker and on the car engine. This appendix gives a more detailed outline of the design, simulation and construction steps made for the vibration energy harvester.

E.1 Cantilever beam resonance harvester

A resonance harvester was build using a cantilever beam design. An electromagnetic transducer is obtained with a fixed coil and magnets attached to the cantilever on both sides of the coil. The design of the cantilever beam resonance harvester is based on the design presented by Glynne-Jones et al. [21], where it was further improved by Torah et al. [47] and some final optimizations were done in the work of Beeby et al. [6]. In this work was not the focus on the optimization of the harvester design, but is was desired to construct a simple energy harvester with a proven design.

In the first subsection, the most basic design parameters are identified to calculate quickly the resonance frequency based on linear beam theory. In subsection two, a 3D model of the energy harvester was made in fusion 360 and the fabrication process was set out. Successively, a prototype of the energy harvester was fabricated. In subsection three, the parameters to fill in the equations of motion have been determined in the system identification experiments. Finally, in subsection four, a dynamical simulation using a numerical ODE solver in Matlab and an experimental validation are performed.

E.1.1 Basic design parameters

The eigenfrequency of a linear mass- spring- damper system depends on the mass and stiffness; $f_n = \frac{1}{2\pi}\sqrt{\frac{k}{m}}$. The stiffness of a beam can be calculated by: $k = \frac{3EI}{L^3}$, where k is the suspension stiffness, E is the Young's modulus of the material, I is the area moment of inertia ($\frac{1}{12}wh^3$ for a rectangular cross section), and L is the total length of the beam. The mass is approximated as a point mass at the tip of the beam. Taking roughly one-third of the cantilever mass and the masses at the tip of the beam, results in the total mass: $m = \frac{33}{140}m_b + m_t$, where m is the total tip mass, m_b is the total beam mass and m_t is the added mass on the tip of the beam [49].

With all the design parameters identified, the configuration procedure can be started. The eigenfrequency was desired to be above the suspension mode eigenfrequency of the shaker, which is between 20 to 30 Hz. In the same time, a too high eigenfrequency could bring difficulties with other lab equipment (For instance laser sensors), because the amplitude would drop significantly al low acceleration levels and much higher sample frequencies are required (At least 10 times the excitation frequency) to obtain a clear view of the motion. Therefore, it was chosen to design the eigenfrequency of the harvester around 40 Hz. The design parameters of the cantilever beam resonance harvester can be found in table E.1. The resonance frequency of the energy harvester should be at 42 Hz, when four magnets are used as tip mass at 20 mm from the cantilever base.

E.1.2 3D model

The 3D model was generated using Autodesk Fusion 360 software. Figure E.1 shows the 3D model and a picture of the constructed linear resonance harvester. An exploded view containing all the component is depicted in Figure E.2.

For the fabrication process of the cantilever beam resonance harvester, some additional parts have been created. These parts are shown in Figure E.4. First, a coil-base was constructed to wind the coil around. This base has been 3D printed in PLA. After winding the coil made of $71\mu m$ lacquered copper wire, a heat gun was used to remove the PLA base and melt the copper wires together. The second additional part is a base to hold the cubic magnets in the desired configuration and position. This enabled to glue te magnets easily using Bison Fast Fix[2] to the spring steel cantilever.

TABLE E.1: **Cantilever beam resonance harvester; design parameters and component specifications**

Spring steel cantilever	
Parameter	**Value [ ]**
Length	20 mm
Width	11 mm (2 x 5.5 mm)
Thickness	0.10 mm
Density	7900 kg/m^3
Young's modulus	190 GPa
NdFeB permanent magnets	
Parameter	**Value [ ]**
Length	3 mm
Width	3 mm
Height	3 mm
Mass	0.205 g
Flux density	1.2 T
Copper coil	
Parameter	**Value [ ]**
Number of windings	460
Wire diameter	71 µm
Height	5 mm
Length	8 mm
Width	4 mm
Resistance	31.7 Ω
Inductance	670 mH at 1kHz

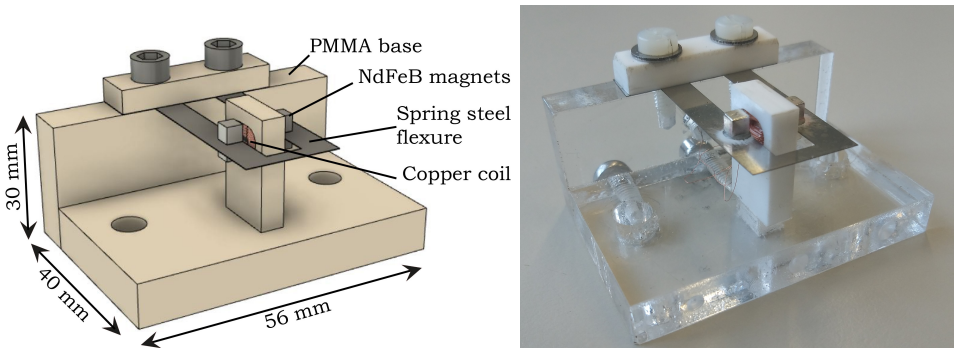

(A) (B)

FIGURE E.1: **3D model of the cantilever beam resonance harvester (A) and the fabricated prototype (B)**

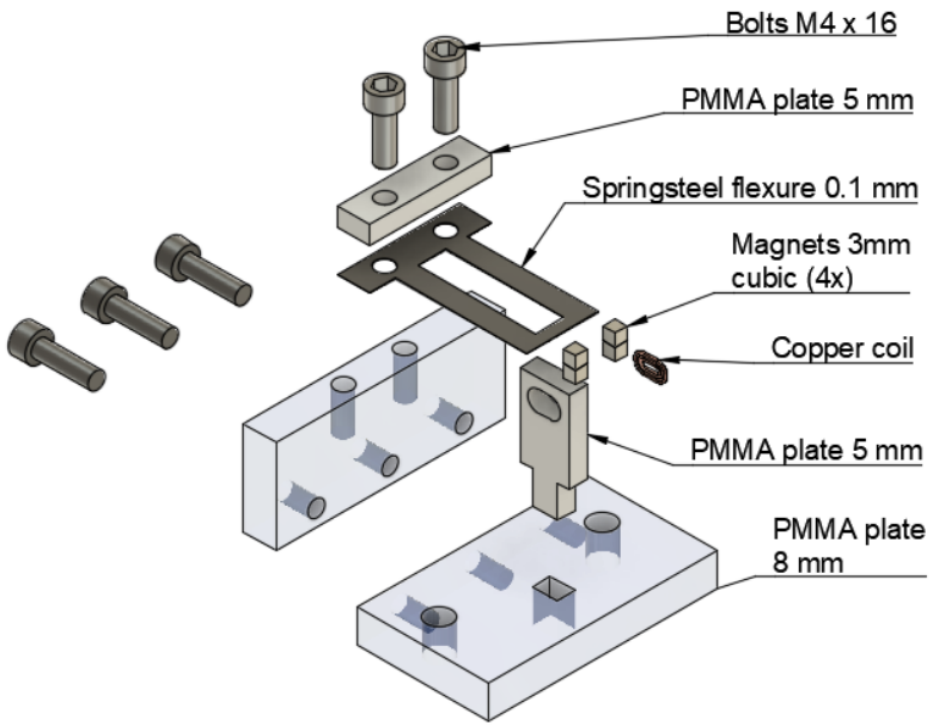

FIGURE E.2: **Exploded view of the cantilever beam resonance harvester showing the various components used to build the prototype. The bolts are used to hold the cantilever and various PMMA base plates together and are tapped into the PMMA.**

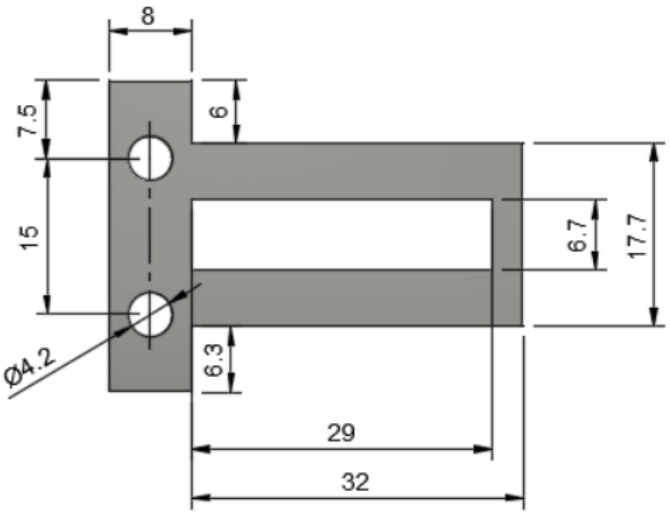

FIGURE E.3: **Cantilever beam resonance harvester; dimensioning of the 0.1 mm thick spring steel cantilever. The cantilever was cut out of a metal sheet using a OPTEC laser cutter.**

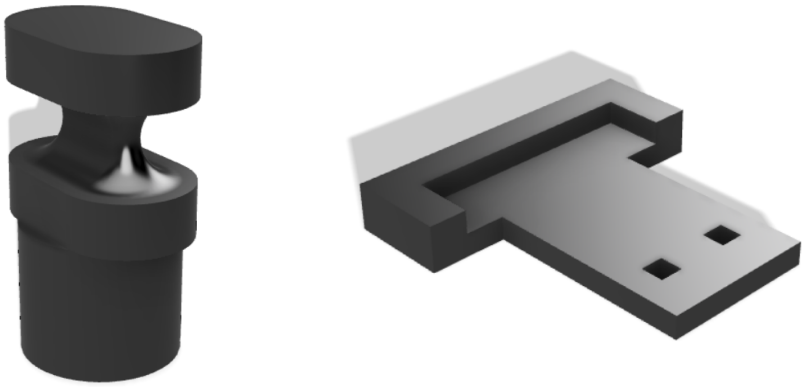

(A) (B)

FIGURE E.4: **Additional 3D printed components used to fabricate the harvester. A base to wind the coil around (A). A basis to place the 3mm cubic magnets in the correct configuration, so the magnets could easily be glued at the correct location on the cantilever beam (B)**

E.1.3 System identification experiments

Mass

The total mass of the four tip magnets was measured to be $0.82g$, as expected from the specifications given. Adding half of the cantilever mass results in a total mass of $0.98g$, which is used for the dynamical analysis.

Stiffness

The dimensions of the fabricated harvester are not exactly the same as in the constructed 3D model, due to material tolerances minor errors in the production process. Also the cantilever is cut out a larger sheet of cold rolled spring steel. By cutting out a smaller piece with a laser cutter, some preloaded stresses can remain in the material, which affects the total stiffness.

Therefore, the cantilever stiffness has been validated in a force-deflection experiment, Figure E.5. The force deflection was measured on top of the permanent magnets, which was assumed as location of the tip mass in the basic design parameters. A stiffness of $61N/m$ was measured in the force deflection experiment. Initially, a stiffness of $65N/m$ was calculated using linear beam theory, which means an error of 6% between the calculated model and the fabricated prototype.

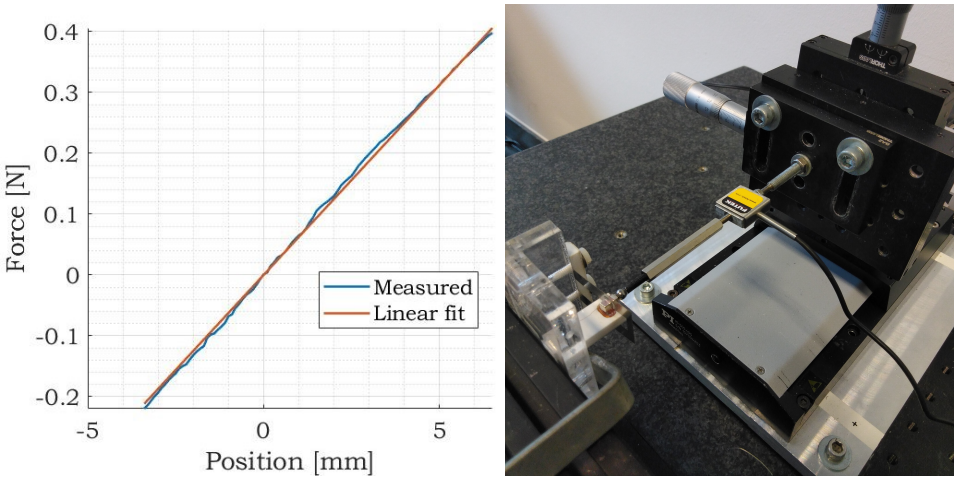

(A) (B)

FIGURE E.5: **Plot of the force deflection experiment with a linear fit included (A) and a picture of the setup used to measure force deflection consisting of a PI M505 linear stage and a FUTEK 250g load cell (B).**

Damping coefficient

The damping of the harvester depends on various factors; the material, air and electromagnetic damping. Where, the latter depends on the load resistance connected to the coil. A damped vibration is used to determine the damping ratio of the system. In a first measurement an open circuit condition was created, in which case the electromagnetic damping is absent [43]. So the measured damping will be purely the mechanical damping of the system. In the second measurement, the coil is connected to a 30Ω load resistance, which is also used in further experiments. This enables the electromagnetic damping, which will increase the total damping coefficient. Figure E.6 shows the damped oscillations of the experiments. The damping ratio can be determined using the logarithmic decrement method:

$$\zeta = \frac{1}{\sqrt{1+(\frac{2\pi}{\delta})^2}} \tag{E.1}$$

where:

ζ = damping coefficient
δ = logarithmic decrement

The logarithmic decrement δ can be calculated from an under damped oscillation using the following equation:

$$\delta = \frac{1}{n} \ln \frac{x(t)}{x(t+nT)} \tag{E.2}$$

where:

$x(t)$ = Amplitude at time t
$x(t+nT)$ = Amplitude n oscillations after t
n = Number of oscillations between the oscillations

In the first experiment, the mechanical damping coefficient of the vibration energy harvester is found to be $\zeta = 0.0025$. Which is purely a loss of energy due to the system mechanics. In the second experiment, with the 30Ω load resistance connected to the coil, a total damping coefficient of $\zeta = 0.0032$ was found, the additional damping with respect to the open circuit experiment can be related to the electromagnetic coupling. The kinetic energy is converted into electricity, useful energy!

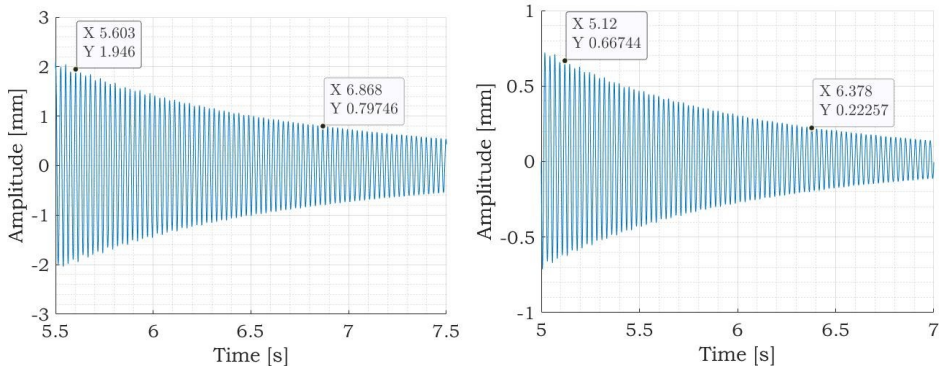

(A) (B)

FIGURE E.6: **Damped oscillations of the vibration energy harvester. While the coil was open circuited, purely mechanical damping is measured (A) and with a 30Ω load resistance attached to the coil, electromagnetic damping is added to the system (B).**

E

E.1.4 Dynamical analysis

With all the model parameters of the fabricated harvester identified, a simulation of the fabricated model can be made by filling in the single mass-spring-damper model parameters of the energy harvester as depicted below.

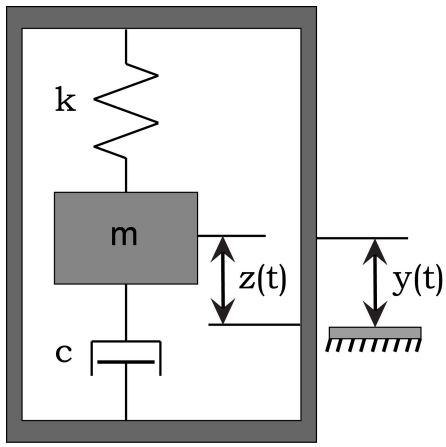

$$m\ddot{z} + c\dot{z} + kz = -m\ddot{y}$$

FIGURE E.7: **Schematic depiction of the cantilever beam resonance harvester as single mass-spring-damper system with the derived equation of motion.**

The dynamical response of the energy harvester has been calculated using the numerical ODE45 solver in Matlab. In order to validate the simulation, a comparison between the simulated and experimental frequency response on a frequency sweep

at a constant acceleration amplitude of $0.1g$ has been made, figure E.8. It can be seen that the shape of the experimental and simulated frequency response is quite similar. Assuming that the frequency sweep in both simulation and experiment are performed at the same speed, it can be stated that the model is correct.

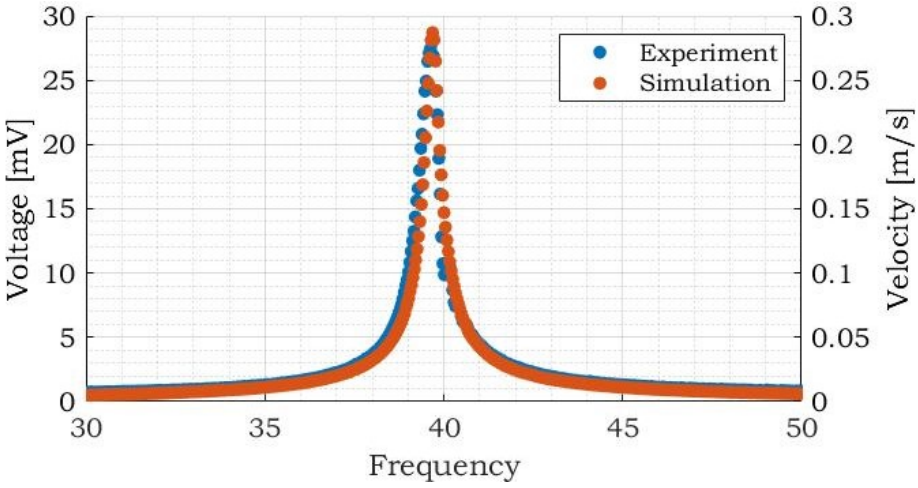

FIGURE E.8: **Simulated and experimental frequency response of the linear resonance harvester**

In figure E.8 can be seen that the simulation and experiment give an almost identical frequency response. There is a factor 0.09 between the velocity and the generated voltage. This is also known as the electromagnetic conversion constant, Φ. Successively, by implementing the electromagnetic conversion constant into to model, according to:

$$V = -\Phi \dot{z} \tag{E.3}$$

where, V is the generated voltage and $\dot{z}$ the velocity of the proof mass with respect to the coil. The voltage generation of the energy harvester can directly be obtained from the model simulation.

Note: *The model does not take nonlinear transducer behavior into account. This can be, for instance, the case when the proof mass amplitude becomes too large and the magnets move out of the coil area.*

E.2 Magnetic spring resonance harvester

A problem arose during the experimental validation of this energy harvester. Due to a small offset in the feed forward controller design, was the largest error near the suspension mode, which is around twenty to thirty hertz. The "resonance region" of the designed nonlinear harvester was in the same region. In order to overcome this problem easily was decided to switch to a linear system with a higher resonance frequency for further research. Therefore, the harvester has not been used in further experiments.

In the design process of this motion energy harvester was chosen for an electromagnetic transducer mechanism, consisting of a stack moving magnets and a static coil. At the top and bottom of the moving magnet stack repulsive fixed magnets are placed, this created a magnetic spring mechanism. To calculate the stiffness coefficients, a model was made using COMSOL Multiphysics. Successively, the resulting force-deflection graph was fitted and used in a dynamical simulation using Matlab. When all the design parameters were determined, a 3D model of the harvester was made using Autodesk Fustion 360. Finally, the harvester was fabricated using 3D printed parts.

E.2.1 COMSOL Multiphysics

In the COMSOL model wizard was chosen for an axisymmetric 2D model in stead of a 3D model to reduce calculation time. At first the geometry was build as half the cross-sectional area of the magnets configuration, figure E.9. On the top and bottom of the configuration are the spring magnets located with the moving magnet stack in the middle. A large area of air is simulated around the magnet configuration to simulate the environment. The force acting on the moving magnets was calculated by altering the position with respect to the spring magnets by a parametric sweep. This resulted in a table containing the force-deflection data, which was loaded into Matlab.

E.2.2 Function fit

The spring constants have been estimated using the matlab curve fitting toolbox. Loading the force-deflection data from COMSOL and using the 'fit' function, the equation to describe the force-deflection relation of the magnet configuration was derived, figure E.10.

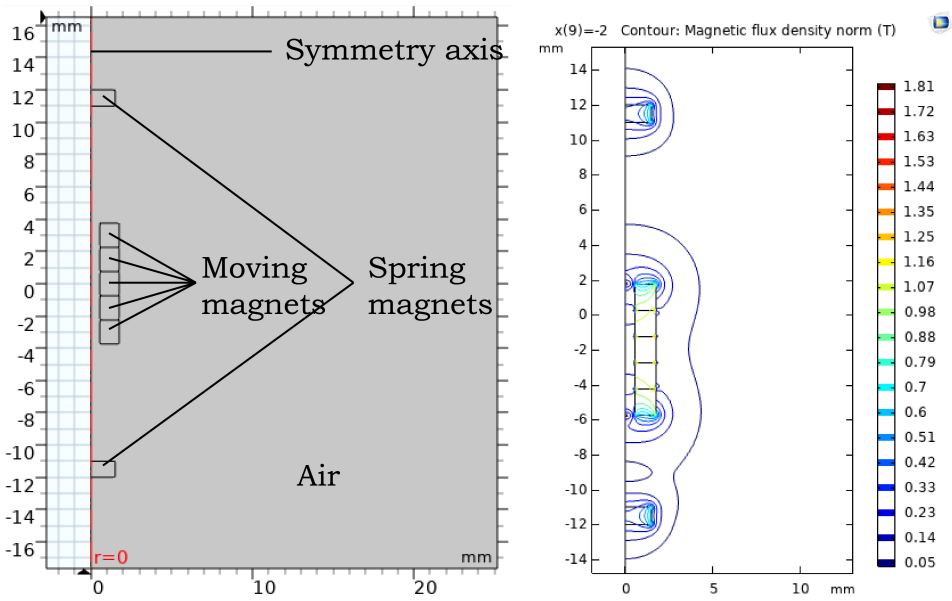

FIGURE E.9: **COMSOL geometry and flux density contour lines.**

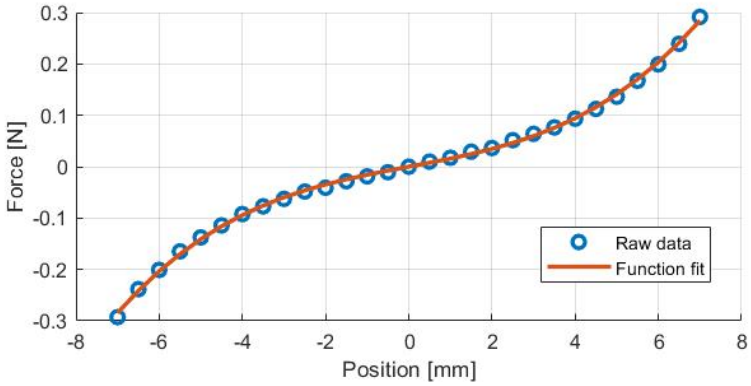

FIGURE E.10: **Force-deflection data from COMSOL compared with the fitted function curve,** $F = 5.18 \cdot 10^5 z^3 + 15.25z$

E.2.3 Dynamical analysis

The harvester is modeled as a single mass-spring-damper system E.7, where the force due to the stiffness kz is replaced by a first and third order term $k_1 z + k_3 z^3$, as found in the force deflection function fit. The damping factor ζ, which consists of a combination of air, magnetic inductance and friction, was estimated at 3.2%. This value was obtained by calculating the Q-factor of the experimental frequency sweep:

$$Q = \frac{f_r}{\Delta f} \tag{E.4}$$

where, f_r is the resonance frequency peak and Δf is the half power bandwidth. With the obtained Q-factor, the damping factor ζ can be calculated: $\zeta = \frac{1}{2Q}$. Successively, an ordinary differential equation (ODE) solver is used to simulate the system response on the sinusoidal frequency sweep. Because of the positive nonlinear stiffness term, an hardening effect would be expected. This would result in different responses when a up or down sweep is performed [31]. However, when the oscillator is exited at a low level acceleration, it will show almost the same response as a linear oscillator, because the nonlinear forcing term is negligible at very low amplitudes.
Figure E.11 shows the simulated and experimental frequency response. In the simulation, a slight tension to the left can be seen in the peak of the response. Which would be the result of the hardening effect of the nonlinear spring. The experimental response shows a more symmetric peak in the response, which would be expected in a linear mass - spring - damper system. Due to the low excitation level, the harvester's proof mass excitation remains so low, that the stiffness can be approximated as linear. For higher acceleration levels the excitation increases, resulting in an increase of the nonlinear stiffness effect.

E.2.4 3D model

The final steps before fabrication are the modeling of a 3D model, material selection and set out the construction process. Building the 3D model was done using Autodesk Fusion 360 software. All the separate parts of the energy harvester are modeled and assembled, to obtain an overview of the total design, see figure E.12. More details on the parts and materials used to construct the harvester can be found in table E.2 and figure E.13. The magnets located in the end caps were glued with two component epoxy. The same was done for the copper coil connection with the Acrylic tube and the end cabs to the tube.

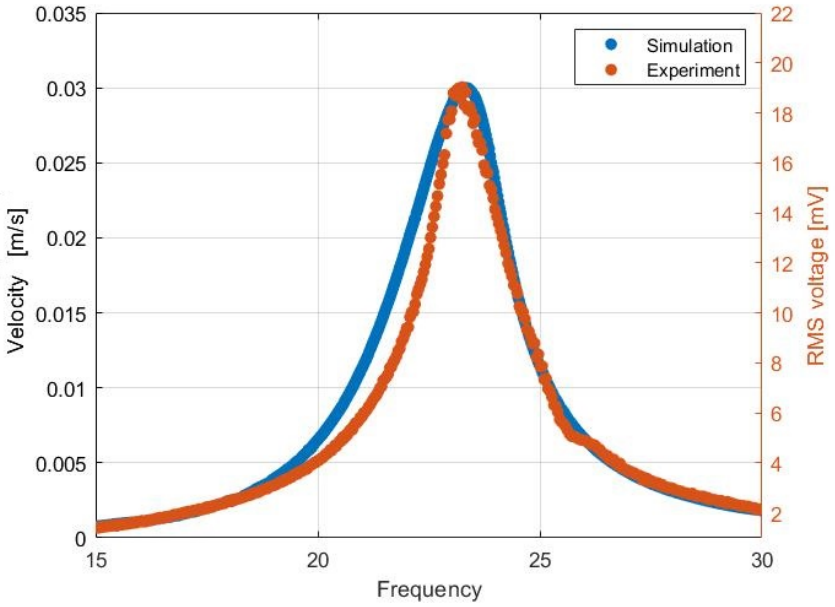

FIGURE E.11: **Simulated and experimental frequency response of the nonlinear resonance harvester**

FIGURE E.12: **3D render of the designed motion energy harvester made in Autodesk Fusion 360**

TABLE E.2: **Permanent magnet characteristics of the magnets delivered by HKCM engineering**

Material	Dimensions		Properties	
	Diameter [mm]	Thickness [mm]	Flux density [T]	Mass [g]
NdFeB-48H	5.40 (3.40)	2.30	1.37	0.21
NdFeB-N35	7.00	1.00	1.17	0.29

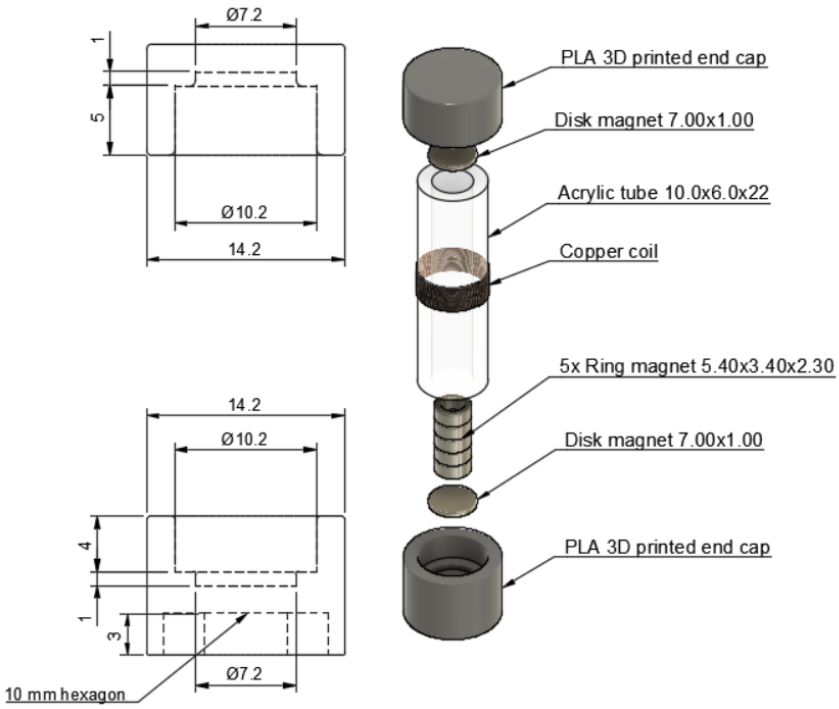

FIGURE E.13: **Crossection drawing of end caps and energy harvester exploded view**

Bibliography

[1] (2020a). NI-9234 - National Instruments. https://www.ni.com/nl-nl/support/model.ni-9234.html.

[2] (2020b). NI-9260 - National Instruments. https://www.ni.com/nl-nl/support/model.ni-9260.html.

[3] (2020). Vibration Control Software - Vibration Software | Brüel & Kjær. https://www.bksv.com/en/products/shakers-and-exciters/vibration-controllers/vibration-control-software.

[4] (2020). What Is a CompactRIO Controller? - National Instruments. https://www.ni.com/nl-nl/shop/compactrio/what-are-compactrio-controllers.html.

[5] Andò, B., Baglio, S., Marletta, V., Pistorio, A., and Bulsara, A. R. (2019). A Low-Threshold Bistable Device for Energy Scavenging From Wideband Mechanical Vibrations. IEEE Transactions on Instrumentation and Measurement, 68(1):280–290.

[6] Beeby, S. P., Torah, R. N., Tudor, M. J., Glynne-Jones, P., O'Donnell, T., Saha, C. R., and Roy, S. (2007). A micro electromagnetic generator for vibration energy harvesting. Journal of Micromechanics and Microengineering, 17(7):1257–1265.

[7] Beeby, S. P., Tudor, M. J., and White, N. M. (2006). Energy harvesting vibration sources for microsystems applications. Measurement Science and Technology, 17(12):R175–R195.

[8] Beeby, S. P., Wang, L., Zhu, D., Weddell, A. S., Merrett, G. V., Stark, B., Szarka, G., and Al-Hashimi, B. M. (2013). A comparison of power output from linear and nonlinear kinetic energy harvesters using real vibration data. Smart Materials and Structures, 22(7):075022.

[9] Billah, K. Y. R. and Shinozuka, M. (1990). Numerical method for colored-noise generation and its application to a bistable system. Physical Review A, 42(12):7492–7495.

[10] Blad, T., Nijssen, J., Broeren, F., Boogaard, B., Lampaert, S., van den Toorn, S., and van den Dobbelsteen, J. (2020). A Rapidly Deployable Test Suite for Respiratory Protective Devices in the COVID-19 Pandemic. Applied Biosafety, 25(3):161–168.

[11] Bowers, B. J. and Arnold, D. P. (2009). Spherical, rolling magnet generators for passive energy harvesting from human motion. Journal of Micromechanics and Microengineering, 19(9):094008.

[12] Cambridge, C. (2011). Revolutionary Leadless Pacemaker From Cambridge Consultants. https://www.dexigner.com/news/24177.

[13] Cottone, F., Gammaitoni, L., Vocca, H., Ferrari, M., and Ferrari, V. (2012). Piezoelectric buckled beams for random vibration energy harvesting. Smart Materials and Structures, 21(3):035021.

[14] Daqaq, M. F. (2011). Transduction of a bistable inductive generator driven by white and exponentially correlated Gaussian noise. Journal of Sound and Vibration, 330(11):2554–2564.

[15] Della Flora, L. and Gründling, H. (2008). Time domain sinusoidal acceleration controller for an electrodynamic shaker. IET Control Theory & Applications, 2(12):1044–1053.

[16] Elfrink, R., Matova, S., de Nooijer, C., Jambunathan, M., Goedbloed, M., van de Molengraft, J., Pop, V., Vullers, R., Renaud, M., and van Schaijk, R. (2011). Shock induced energy harvesting with a MEMS harvester for automotive applications. In 2011 International Electron Devices Meeting, pages 29.5.1–29.5.4.

[17] Fan, K., Cai, M., Liu, H., and Zhang, Y. (2019a). Capturing energy from ultra-low frequency vibrations and human motion through a monostable electromagnetic energy harvester. Energy, 169:356–368.

[18] Fan, K., Zhang, Y., Liu, H., Cai, M., and Tan, Q. (2019b). A nonlinear two-degree-of-freedom electromagnetic energy harvester for ultra-low frequency vibrations and human body motions. Renewable Energy, 138:292–302.

[19] Gao, Y., Leng, Y., Javey, A., Tan, D., Liu, J., Fan, S., and Lai, Z. (2016). Theoretical and applied research on bistable dual-piezoelectric-cantilever vibration energy harvesting toward realistic ambience. Smart Materials and Structures, 25(11):115032.

[20] Geisler, M., Boisseau, S., Perez, M., Gasnier, P., Willemin, J., Ait-Ali, I., and Perraud, S. (2017). Human-motion energy harvester for autonomous body area sensors. Smart Materials and Structures, 26(3):035028.

[21] Glynne-Jones, P., Tudor, M., Beeby, S., and White, N. (2004). An Electromagnetic, Vibration-Powered Generator for Intelligent Sensor Systems. Sensors and Actuators A: Physical, 110:344–349.

[22] Hawes, D. (2017). Nonlinear Stochastic Vibration Analysis for Energy Harvesting and Other Applications. Thesis, Department of Engineering, University of Cambridge.

[23] Katalenic, A. (2013). Control of Reluctance Actuators for High-Precision Positioning. Proefschrift, Eindhoven University of Technology, Eindhoven.

[24] Kaźmierski, T. J. and Beeby, S., editors (2011). Energy Harvesting Systems: Principles, Modeling and Applications. Springer, New York.

[25] Kok, S.-L., Ab Rahman, M. F., Yap, D. F. W., and Ho, Y. H. (2011). Bandwidth widening strategies for piezoelectric based energy harvesting from ambient vibration sources. In 2011 IEEE International Conference on Computer Applications and Industrial Electronics (ICCAIE), pages 492–496.

[26] Lalanne, C. (2014a). Mechanical Vibration and Shock Analysis, Random. In Mechanical Vibration and Shock Analysis, Random, Mechanical Vibration and Shock Analysis, pages 84–89. ISTE Ltd, London, third edition.

[27] Lalanne, C. (2014b). Mechanical Vibration and Shock Analysis, Random. Mechanical Vibration and Shock Analysis. ISTE Ltd, London, third edition.

[28] Lalanne, C. (2014c). Mechanical Vibration and Shock Analysis, Random. In Mechanical Vibration and Shock Analysis, Random, Mechanical Vibration and Shock Analysis, pages 160–165. ISTE Ltd, London, third edition.

[29] Lan, C. and Qin, W. (2017). Enhancing ability of harvesting energy from random vibration by decreasing the potential barrier of bistable harvester. Mechanical Systems and Signal Processing, 85:71–81.

[30] Lang, G. F. and Snyder, D. (2001). Understanding the Physics of Electrodynamic Shaker Performance. SOUND AND VIBRATION, (10):9.

[31] Lee, C., Stamp, D., Kapania, N. R., and Mur-Miranda, J. O. (2010). Harvesting vibration energy using nonlinear oscillations of an electromagnetic inductor. In Energy Harvesting and Storage: Materials, Devices, and Applications, volume 7683, page 76830Y. International Society for Optics and Photonics.

[32] Leng, Y. G., Gao, Y. J., Tan, D., Fan, S. B., and Lai, Z. H. (2015). An elastic-support model for enhanced bistable piezoelectric energy harvesting from random vibrations. Journal of Applied Physics, 117(6):064901.

[33] Martini, L. (2015). Real-time control of an electrodynamic shaker. PhD thesis, Università di Bologna, Bologna.

[34] Merret, G. and Yang, K. (2010). Energy Harvesting Network. http://eh-network.org/data/.

[35] Neri, I., Travasso, F., Mincigrucci, R., Vocca, H., Orfei, F., and Gammaitoni, L. (2012). A real vibration database for kinetic energy harvesting application. Journal of Intelligent Material Systems and Structures, 23(18):2095–2101.

[36] Priya, S. and Inman, D. J. (2009). Energy Harvesting Technologies. Springer, New York.

[37] Rantz, R. and Roundy, S. (2016). Characterization of real-world vibration sources with a view toward optimal energy harvesting architectures. In Industrial and Commercial Applications of Smart Structures Technologies 2016, volume 9801, page 98010P. International Society for Optics and Photonics.

[38] Rantz, R. and Roundy, S. (2017). Characterization of Real-world Vibration Sources and Application to Nonlinear Vibration Energy Harvesters. Energy Harvesting and Systems, 4(2):67–76.

[39] Reilly, E. K., Miller, L. M., Fain, R., and Wright, P. (2009). A STUDY OF AMBIENT VIBRATIONS FOR PIEZOELECTRIC ENERGY CONVERSION. PowerMEMS, page 5.

[40] Rom, W., Karner, M., and Kloker, Manuela, K. (2017). DEWI: Automotive. http://www.dewiproject.eu/domains/automotive/.

[41] Romero, E., Neuman, M. R., and Warrington, R. O. (2011). Rotational energy harvester for body motion. In 2011 IEEE 24th International Conference on Micro Electro Mechanical Systems, pages 1325–1328.

[42] Salauddin, M., Toyabur, R. M., Maharjan, P., and Park, J. Y. (2018). High performance human-induced vibration driven hybrid energy harvester for powering portable electronics. Nano Energy, 45:236–246.

[43] Singh, A., Mohapatra, Y. N., and Kumar, S. (2002). Electromagnetic induction and damping - quantitative experiments using PC interface. American Journal of Physics, 70(4):424–427.

[44] Smith, S. W. (1999a). The scientist and engineer's guide to digital signal processing. In The Scientist and Engineer's Guide to Digital Signal Processing, pages 225–238. California Technical Pub., San Diego (Calif.).

[45] Smith, S. W. (1999b). The scientist and engineer's guide to digital signal processing. In The Scientist and Engineer's Guide to Digital Signal Processing, pages 423–249. California Technical Pub., San Diego (Calif.).

[46] Steinwolf, A. (2006). Random Vibration Testing Beyond PSD Limitations. SOUND AND VIBRATION, 40:12–21.

[47] Torah, R. N., Glynne-Jones, P., Tudor, M. J., and Beeby, S. P. (2007). ENERGY AWARE WIRELESS MICROSYSTEM POWERED BY VIBRATION ENERGY HARVESTING. PowerMEMS, page 4.

[48] van Dijk, J. (2019). Stibat zamelt ruim 7 procent meer batterijen in voor recycling. https://www.stibat.nl/nieuws/persberichten/stibat-zamelt-ruim-7-procent-meer-batterijen-in-voor-recycling/.

[49] vlab.amrita.edu (2011). Free Vibration of a Cantilever Beam with a Lumped Mass at Free End. http://vlab.amrita.edu/?sub=3&brch=175&sim=1078&cnt=1.

[50] Wang, W., Cao, J., Zhang, N., Lin, J., and Liao, W.-H. (2017). Magnetic-spring based energy harvesting from human motions: Design, modeling and experiments. Energy Conversion and Management, 132:189–197.

[51] Yildirim, T., Ghayesh, M. H., Li, W., and Alici, G. (2017). A review on performance enhancement techniques for ambient vibration energy harvesters. Renewable and Sustainable Energy Reviews, 71:435–449.